Chem Soc Rev

Bio-Inspired Strategies for Next-Generation Solar Mobile Power Sources

Journal:	*Chemical Society Reviews*
Manuscript ID	CS-SYN-11-2020-001493.R2
Article Type:	Review Article
Date Submitted by the Author:	06-Jul-2021
Complete List of Authors:	Yoon, Jungjin; Penn State University Park, Center for Energy Harvesting Materials and System Hou, Yuchen; Pennsylvania State University, Materials Science and Engineering Knoepfel, Abbey ; Penn State University Park Yang, Dong; Pennsylvania State University, Materials Science and Engineering Ye, Tao; Pennsylvania State University, Materials Science and Engineering Zheng, Luyao; Penn State University Park, Center for Energy Harvesting Materials and System Yennawar, Neela; Pennsylvania State University Sanghadasa, Mohan; U.S. Army, Aviation and Missile Research, Development, and Engineering Center, Weapons Development and Integration Directorate Priya, Shashank; Pennsylvania State University Wang, Kai; Penn State University Park, Center for Energy Harvesting Materials and System; Virginia Tech

Bio-Inspired Strategies for Next-Generation Perovskite Solar Mobile Power Sources

Received 00th January 20xx,
Accepted 00th January 20xx

DOI: 10.1039/x0xx00000x

Jungjin Yoon,[a#] Yuchen Hou,[a#] Abbey Marie Knoepfel,[a] Dong Yang,[a] Tao Ye,[a] Luyao Zheng,[a] Neela Yennawar,[b] Mohan Sanghadasa,[c] Shashank Priya,[a]* Kai Wang[a]*

Smart electronic devices are becoming ubiquitous due to many appealing attributes including portability, long operational time, rechargeability and compatibility with user-desired form factor. Integration of mobile power sources (MPS) based upon photovoltaic technologies with smart electronics will continue to drive improved sustainability and independance. With high efficiency, low-cost, flexibility and lightweight features, halide perovskite photovoltaics are a promising candidate for MPS. Realization of these photovoltaic MPS (PV-MPS) with unconventionally extraordinary attributes requires new 'out-of-box' designs. Natural materials have provided promising designning solutions to engineer properties under a broad boundary conditions, ranging from molecules, proteins, cells, tissues, apparatus and systems in animals, plants, and humans optimized through billions of years evolution. Applying bio-inspired strategies in PV-MPS could be biomolecular modificaiton on crystallization at atomic/meso-scale, bio-structural duplicaiton at device/system level and bio-mimicking at functional level to render efficient charge deliverage, energy transport/utilization, as well as stronger resistiveness against environmental stimuli (e.g., self-healing and self-cleaning). In this review, we discuss the bio-inspired/-mimetic structures, experimental models, and working principles, with goal of revealing physics and bio-microstructures relevant for PV-MPS. Emphasis is on identifying the strategies and material designs towards performance surging of emerging halide perovskite PV and strategizing their bridge to future MPS.

Contents

[a] *Department of Materials Science & Engineering, Pennsylvania State University, University Park 16802, PA, United States*
[b] *Huck Institute of the Life Sciences, Pennsylvania State University, University Park 16802, PA, United States*
[c] *U.S. Army Combat Capabilities Development Command Aviation & Missile Center, Redstone Arsenal, Alabama 35898, United States*
#Equal contribution
**Correspondence: S.P.: sup103@psu.edu; K.W.: kaiwang@psu.edu*
Electronic Supplementary Information (ESI) available: [details of any supplementary information available should be included here]. See DOI: 10.1039/x0xx00000x

Nomenclature

2,2',7,7'-Tetrakis[N,N-di(4-methoxyphenylamino]-9,9'-spirobifluorene	Spiro-MeOTAD
adenine	A
air mass	AM

aluminum zinc oxide	AZO
artificial intelligence	AI
atomic layer deposition	ALD
bacteriorhodopsin	bR
bio-sensitized solar cell	BSSC
bulkheterojunction	BHJ
carbon fibre reinforced plastic	CFRP
carbon nanotube	CNT
$CH_3NH_3PbI_3$	$MAPbI_3$
charge transfer layers	CTL
charge transport	CT
chemical vapor deposition	CVD
conduction band minimum	CBM
cytosine	C
density functional theory	DFT
deoxyribonucleic acid	DNA
diphenyl-2-pyridylamine	DPPA
dye-sensitized solar cell	DSSC
electron transporting layer	ETL
field of view	FOV
fill factor	FF
fluorinated triphenylamine	FTPA
fluorine-doped tin oxide	FTO
fluoro-octyltrichlorosilane	FOTS
force-displacement	F-D
Förster resonance energy transfer	FRET
fractal dimension	Ds
ganglion cell layer	GCL
glancing angle deposition	GLAD
glass transition temperature	Tg
grain boundaries	GBs
guanine	G
hexadecyl trimethyl ammonium chloride	CTMA
hierarchical-metal-grids	HMG
highest occupied molecular orbital	HOMO
hole transporting layer	HTL
indium tin oxide	ITO
inner nuclear layer	INL
internet of energy	IoE
internet of things	IoT
inverse-opal	IO
inverse-opal perovskite	IOP
inverted micro-pyramidal structured	IMPS
large-diameter-long	LDL
large-volume amines	LVA
levelized cost of energy	LCOE
light-emitting diode	LED
liquid metal	LM
lowest unoccupied molecular orbital	LUMO
Magnolia liliifora leaf vein	MLLV
methylammonium iodide	MAI
mobile power source	MPS
multi-walled CNT	MWCNT
nanoparticle	NP
nanorod	NR
nanowire	NW
oblique-incidence energy-density loss	OEL
open-circuit voltage	V_{OC}
organic photovoltaic	OPV
outer nuclear layer	ONL
perovskite solar cell	PSC
phenyl-C61-butyric acid methyl ester	PCBM
photoluminescence	PL
photonic crystal	PC
photovoltaic	PV
poly(3,4-ethylenedioxythiophene):poly(styrene-sulfonate)	PEDOT:PSS
poly(3-hexylthiophene)	P3HT
poly(9,9-dioctylfluorene-co-fluorenone-comethylbenzoic ester)	PFM
poly(styrene-co-butadiene)	SBS
polydimethylsiloxane	PDMS
polyethylene glycol	PEG
polyethylene naphthalate	PEN
polyethylene terephthalate	PET
polyimide	PI
polyurethane	PU
porous aluminium oxide membrane	PAM
power conversion efficiency	PCE
purple membrane	PM
quantum dot solar cell	QDSC
quasi-fractal	QF
scanning electron microscopy	SEM
short-circuit current density	J_{SC}
shunt resistance	R_{sh}
single-walled carbon nanotube	SWNT
small-diameter-short	SDS
specific energy absorption	SEA
thymine	T
transient absorption	TA
transition metal oxide	TMO
transparent conductive electrode	TCE
transparent conductive oxide	TCO
unmanned aerial vehicle	UAV
valance band maximum	VBM
$WO_3/Ag/WO_3$	WAW

1. Introduction

For over 4.6 billion years, sunlight has been the largest natural energy source for our planet and has played critical role in life existence.[1–3] Early on, solar radiations provided the energy required for biomolecular transformations that drove various biophysical processes, such as metabolism, to create survival of lifeform autotrophically, chemotropically, or heterotrophically.[4] Later, photosynthetic processes emerged in microbes utilizing sunlight, water and carbon dioxide to synthesize oxygen and glucose, changing the atmospheric composition of ancient Earth and providing the foundation for the birth of aerobic multicellular life. Over time, these organisms have developed a variety of efficient ways to use solar energy. For example, as shown in **Figure 1**, photosynthesis in green plants and cyanobacteria demonstrate high efficiencies reaching up to 5–10%.[5] Birds are known to use photo-sensitive molecules in their retina to guide their navigation with the help of sunlight and geomagnetic field (through tuning the ratio between photoexcited singlet and triplet states under magnetic field).[6] Insects and hornets are known to exhibit a photoconductive phenomenon at the 'yellow strips' of their cuticle,[7] which is believed to correlate with their daytime flight as solar radiation speeds up restoration of the ionic channel activity and the synaptic transmission in shoving motion.[8] For poikilotherms or cold blooded animals such as frog, absorption of heat from solar radiation is an important way to regulate their body temperature after hibernation, which is related to the solar-thermal effect of bio-dye molecules'.[9]

Today, rising electrification in developing countries and rapid development of electronic devices in developed countries has created a huge electricity demand. In order to meet this growing demand, solar energy is being considered as one of the important renewable energy solutions. The COVID-19 pandemic and the post-COVID-19 era, when mobility restrictions limit activities of traditional power sectors, have demonstrated that renewable energy such as solar photovoltaic techniques exhibit higher resilience than conventional energy sources.[10] Projecting

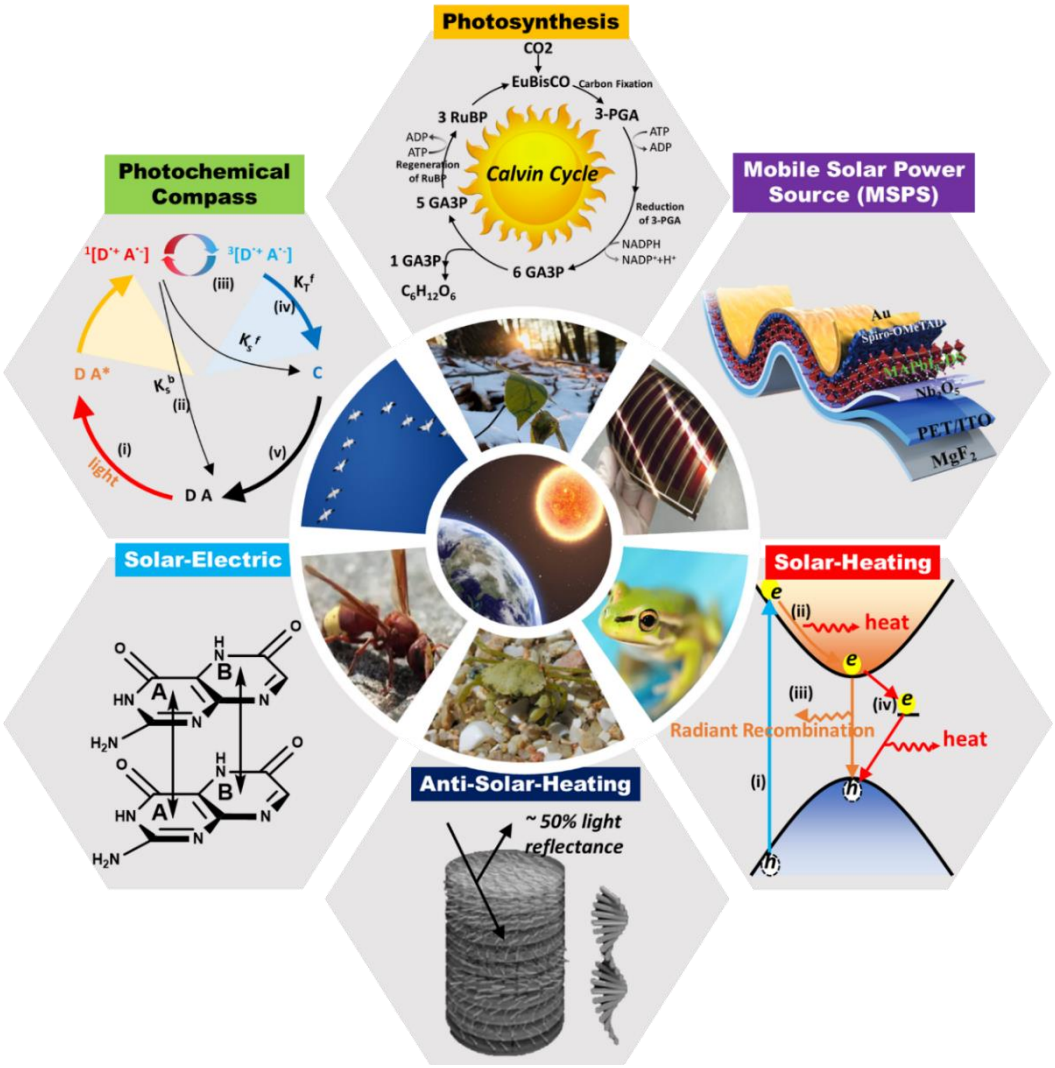

Figure 1 Examples of utilization of solar energy by natural creatures on Earth and the man-made solar cell developed for harvesting solar energy. Adapted with permission from multiple online resources.[6,11–16] Other picture credit: K.W., Y.H., and J.Y.

to the future, solar energy could play an important role in enabling longer operating times for mobile electronic devices such as smart phones, smart watches, various health monitoring sensors, mini-Androids, drones, etc. For these ubiquitous devices, photovoltaic mobile power sources (PV-MPS), with an 'off-the-grid' design, can independently and sustainably provide energy for recharging batteries and are attractive solutions for future devices.

PV-MPS are attractive for use in mobile electronic devices due to their properties including portability, light-weight, flexibility, foldability, high power conversion efficiency (PCE) and long lifetime. Recently, halide perovskites have demonstrated attractive physical properties such as micrometer-scale long exciton diffusion length, large optical absorption coefficient to 10^5 cm^{-1}, direct bandgaps with great tunability down to the ideal 1.5 eV and great mechanical attributes such as high folding, bending, and stretching tolerance thanks to the 'soft' nature of the crystallographic lattice.[11–15] These properties make them good photoactive layer candidates for photovoltaic applications. Compared to traditional first generation (1G) PVs of crystalline gallium arsenide (GaAs) and silicon (Si) (rigid and inflexible), and second generation (2G) PVs of multicrystalline or thin film inorganics, perovskite PV exhibits high efficiency, high flexibility and low-cost simultaneously, representing a promising technique for third generation (3G) PVs, particularly fitting well with the niche market of MPS. So far, perovskite PV displayed an ultrahigh PCE of over twenty-five percent, exceeding that of state-of-the-art commercial multicrystalline silicon PVs,[16,17] as well as other 3G PVs, including dye-sensitized solar cells (DSSCs), organic photovoltaics (OPVs), and quantum dot solar cells (QDSCs).[16,17] As shown in **Figure 2a**, low manufacturing cost, and the mechanical merits of material make perovskite PV a good candidate for MPS applications. Another key figure-of-merit for MPS applications is the power-to-weight ratio (specific power or mass power density) defined by the overall output power over a specific device weight. In comparison to other flexible PV techniques based on thin film CdTe, amorphous silicon, organics, and QD light absorbers,[18,18–23] perovskite PV exhibits the highest value of 29.4 W/g (**Figure 2b**), which could give the MPS a bonus attribute of ultra-light-weight. Similar to power-to-weight ratio, power generation per unit area could be another key figure-of-merit, which can be represented from the PCE value. In principle, PCE is defined as the ratio of electric power output to light power

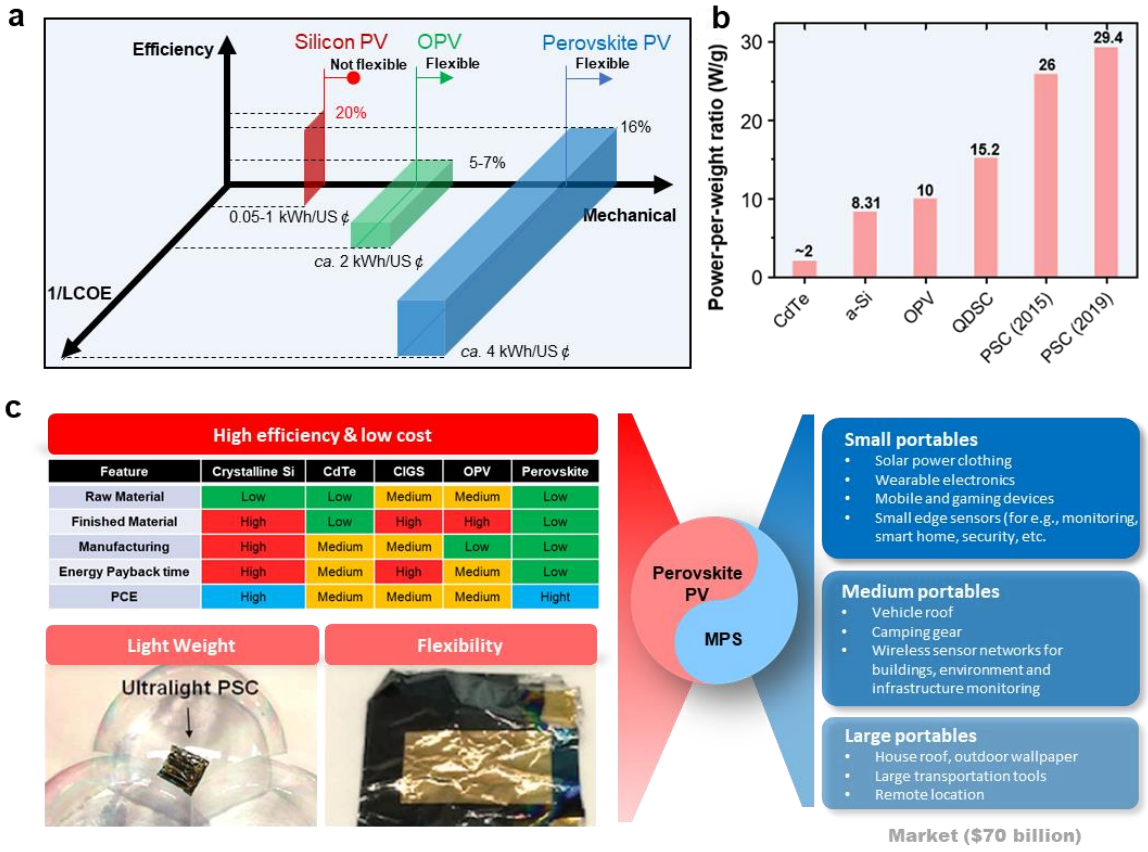

Figure 2 (a) 'Product volume' of different PV techniques. A 3D Cartesian coordinate system is used here to quantify the market potential of different PV techniques: Efficiency, Flexibility and 1/LCOE (cost effectiveness defined by how much electricity can be used per unit cost) are the three indexes. A larger volume indicates a higher competitiveness and thus higher market potential. **(b)** Power-per-weight ratios of various types of solar cells, adapted with permission from Ref.[24,29], Copyright 2015 Springer Nature and 2019 The Royal Chemistry of Society. **(c)** The technique basis of perovskite PV including high efficiency and low cost, as well as other attributes of light weight and sufficient flexibility, coupled by the potential market opportunity with a total market volume of $70 billion. Pictures are adapted with permission from Ref. [29,43], Copyright 2019 The Royal Society of Chemistry.

input (i.e., one-sun illumination of 100 mW cm^{-2}) which has taken into consideration of area. For example, Silicon PV with a module efficiency of 20% indicates a maximum electric power output of 20 mW over a 1 cm^2 area under one-sun illumination. In comparison, OPV module displays much smaller power of 5-7 mW cm^{-2} but perovskite module could offer 16 mW cm^{-2} or even higher output, comparable to that of Si-PV.

Taking consideration of these and aiming at different levels of hierarchies, markets, and network, as illustrated in **Figure 2c**, the perovskite PV-MPS could have applications in small wearable electronics,[24–27] such as smart electronics, epidermal electronics, e-textiles for entertainment, gaming and fashion (e.g., *CuteCircuit*[28] by Museum of Science and Industry in Chicago, US and *Project Jacquard*[29] by Google), medium size appliances such as vehicles, drones[30] (e.g., Titan Aerospace's Solara 50 project[31]), and robotics, and large architectural power sources (building and construction integrated power plant). Evolving from rigid devices to flexible electronic fabrics, many different types of products have been added into the market. With continuously growing demand from various applicational goals, market size is expected to reach up to 70 billion dollars by 2025 (Harrop, 2014).[26] Various fields within this market include, outdoor entertainment, healthcare, academic research and education, agriculture, cellular and mobile devices, consumer electronics and appliances, military, finance, athletics, and retail. Traditional 1G and 2G PV techniques may not meet all these implementations, due to their intrinsic brittle nature and lower power-to-weight ratios. Although there have been attempts to incorporate demo samples of silicon or GaAs PV cells[32] into automobiles and unmanned aerial vehicles (UAVs), there are still many barriers to overcome, such as cost, weight, and mechanical durability/endurance before these are feasible options. In the meantime, perovskite PV technology could provide conformal and better performance solutions, as long as issues such as manufacturing, performance, stability, and toxicity are addressed. Bio-inspired materials could be a viable option to address the gap in the current research. Biological materials and processes have been optimized through millions of years of evolution in the 8 million species on Earth. Delicate biomolecules and systems could lead to low-energy-cost synthesis, efficient mass transfer and energy usage, as well as intelligent functionalities such as self-healing and self-cleaning. Implementing templates from various biosystems have accelerated our advancements within disciplines such as engineering,[33] architecture,[34] medicine,[35] neuromorphic computations,[36] etc.

In this review, we will comprehensively discuss the bio-inspired strategies to address existing issues in perovskite PVs by reviewing (1) various biological molecules such as DNA, bacteriorhodopsin, and porphyrins to optimize the perovskite lattice and crystallization at atomic/meso-scale, (2) biological structures to guide an optimized device structure with enhanced light harvesting, and with robust resistivity against environmental stimuli at device level, and (3) biological systems to inspire designs of perovskite PV-MPS with attributes such as increased-efficiency charge transfer, improved energy usage, and self-healing and self-cleaning functionalities at system level. The marriage between biological systems and perovskite photovoltaics for next-generation solar-based mobile power could potentially provide a roadmap to revolutionary techniques in the future. We anticipate this review could bring new insights and collaborations between these two fields.

2. Bio-inspired design for perovskite MPS

The earliest bio-inspired attempt in PV could be traced back to the 70's, and was based on the photosynthesis in green plants (mimicking basic electro-chemical processes) which lead to the early development of the dye-sensitized solar cell (DSSC). It was based on a photoelectrochemical system consisting of natural dye (mimicking pigment chlorophyll) as light absorber, photo-sensitized anode (with TiO_2 offering the suitable conduction band to accept the excited electrons from dye) and an electrolyte (to provide a redox bath to regenerate the dye). In early DSSCs, the liquidous electrolyte and low absorption coefficient of dye significantly limited the efficiency and practical usage. Later, the fast development of solid electrolyte such as 2,2',7,7'-Tetrakis[N,N-di(4-methoxyphenyl)amino]-9,9'-spirobifluorene (Spiro-OMeTAD),[37] as well as the replacement of the natural dye by the halide perovskite materials eventually lead to the prototype of perovskite solar cells (PSCs).[38] Using prior knowledge from OPVs, DSSCs and even G1 and G2 PVs, many efforts have been made in the research and development of PSCs. This included interfacial engineering, compositional engineering, process development, and structural stability[11] to advance the field to a milestone performance with PCE of 25.7% and T80 lifetime of $>10^3$ hours under accelerated testing (working temperature of 70 to 75 °C for solar cells under AM 1.5 one-sun illumination, without cooling systems).[39] However, issues of defects at lattice scale (nm), grain boundaries (GBs) at mesoscale (μm) and their joint effects on Shockley-Read-Hall (SRH) recombination losses, interface-level charge extraction/transport/collection insufficiencies, device-level instability, manufacturing-oriented problems, and system-level non-intelligence need to be addressed with well-evolved and delicate solutions to move towards commercialization of PV-MPS. **Figure 3** provides the overview of the bio-inspired

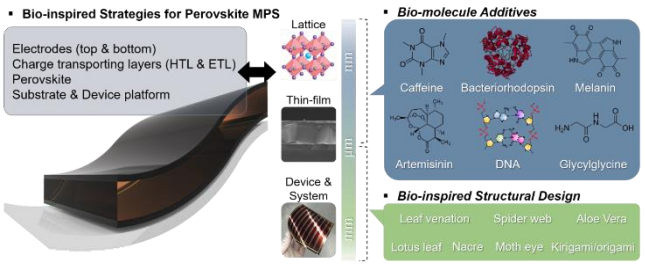

Figure 3 Graphical overview of bio-inspired strategies for perovskite-based MPS (material's perspective). The bio-inspired approaches can be divided into two parts: the engineering of perovskite and charge transporting layers using biomolecules as additives and the structural designs that emulate natural structures. Adapted with permission from Ref. [47], Copyright 2014 Springer Nature.

approaches for optimizing the performance of perovskite PV-MPS on using strategies focused on materials. Various biomolecules with specific functional groups that interact with either lattice defects, GBs or interface-level insufficiencies could be incorporated to enhance the properties for a given application. Bio-structural mimetic design could enable devices with functionalities under different environmental conditions, such as Lotus-like hydrophobicity for rain/dust self-cleaning. From PSC structural perspective, there are three main types of functional layers: electrodes (transparent front electrode and back contact), perovskite light absorber, and functional charge transfer layers (CTLs including hole transporting layer (HTL) and electron transporting layer (ETL)). In the following text, we will specify various bio-derived additives/systems and prior attempts at incorporation, as well as hypothetical applications, in electrodes, charge transfer layers, and perovskite photo-absorber layers in the PV cells.

3. Electrodes

At the user level, a mobile energy source (MPS) requires the device to be as easy to carry as possible. Considering the planar geometry of the PV products, a foldable/flexible feature (such as a poster-like PV module product) can significantly reduce the storage space. This flexibility requirement is highly compatible with the 'soft' nature[40–42] of halide perovskite materials. The perovskite exhibits a low Young's modulus of ~5-20 GPa[42–44] compared to that of over 70 GPa for CIGS and Si-based inorganic semiconductors,[45,46] and higher defect tolerance due to the polaron nature that electron-phonon coupling induced localized lattice deformation in perovskite which could allow the charge carriers to travel long distances regardless of the presence of defects. The CTL including HTL and ETL could also have good compliance in mechanical deformation, which could be realized using thin organic layers, polymeric materials (e.g., poly(3,4-ethylenedioxythiophene) polystyrene sulfonate (PEDOT:PSS) and poly[bis(4-phenyl)(2,4,6-trimethylphenyl)amine (PTAA)), and thin films of nanocrystals. In order to make the whole device highly foldable/flexible, both the back contact (top electrode) and front transparent conductive electrode (bottom electrode) need to be optimized as well. Particularly in application of perovskite solar cells, compatibility to this type of PV technique also have certain requirements such as nonreactivity to perovskite, good semiconductor-metal interface in perovskite solar cells, and protective role against moisture as well as multiple conventional concerns such as energy level matchup and good charge collection/conductivity attributes.

3.1 Top electrode

Assuming the light incidents from the bottom, the top electrode (back-contact electrode) is the uppermost layer in a PSC, generally composed of conductive metals such as silver (Ag), gold (Au), aluminum (Al), cupper (Cu) or carbon (C). The top electrode layer commonly serves to collect charges from the adjacent CTL, and also to reflect the unabsorbed incident light backwards to the perovskite absorber to recycle the light. Ag and Au are commonly used electrode materials and in PSC they exhibit good device efficiency. However, several chemical/mechanical stability issues have been raised recently. Particularly in the case of Ag, the movable I^- ions from the perovskite layer can chemically react with Ag to produce a more stable phase of AgI. This will induce an I-vacancy in the crystallographic lattice which leads to the self-doping of perovskite to a n-type semiconductor and thereby a poor contact at the semiconductor/metal interface. In addition, formation of I^- vacancy could also trigger a quick lattice collapse and eventually the degradation of device performance.[47] This effect can also be present when a HTL is inserted between the perovskite and the top Ag electrode, where the HTL such as Spiro-MeOTAD exhibits unavoidable pin-holes and voids providing highways for the migration of Ag atom from top electrode and I-ions from bottom perovskite and further trigger the subsequent chemical reaction. In order to mitigate this problem, additional interfacial engineering strategies such as passivating perovskite grain boundaries,[48] and inserting interlayers[49–51] could help. Nevertheless, Ag might not be the ideal choice for perovskite PV. Similar to Ag, in Au electrode-based devices, Au atoms can also penetrate underlying CTLs and perovskite layers exposed to temperature conditions above 75 °C. According to Domanski et al.,[52] the migration of Au atoms can be reduced by the insertion of a thin Cr film below Au electrode. This is a typical strategy in making transparent electrodes consisting of ultrathin Cr and Au, where the Cr ultrathin layer could sufficiently inhibit the accumulation of Au into aggerates and consequently uniformize the Au into a continuous film. From a cost and manufacturing perspective, both Au and Ag are not ideal candidates for commercial devices, although they have the highest reported PCE and the most ongoing research is based on Au and Ag. Alternatively, Al could be a more cost-effective solution (1 kg/2 USD vs. 1 kg/60,000 USD of Au). So far, Al has been introduced as the top electrode for the *p-i-n* (inverted) architecture due to its higher Fermi level that can match well with the conduction band (CB) of *n*-type buffer layers for selective electron collection. Regardless, the Al electrode still has the issue of Al infiltration into underlying organic layers, and an additional oxidation issue that superficial Al atoms could be oxidized to Al_2O_3 when exposed to ambient air.[53] In order to overcome these instability issues, particularly the metal atom infiltration problem, Cu, or another inert metal, could be a good electrode candidate. For example, Zhao et al. demonstrated the Cu top electrode in a *p-i-n* (inverted) PSCs displayed good stability.[54] By tracking the hypothetical formation of CuI at the interface between Cu and $CH_3NH_3PbI_3$ ($MAPbI_3$) at an elevated temperature of 80 °C for 100 hours, the authors confirmed that no diffusion of Cu into perovskite occurred. This indicates that Cu could be a feasible candidate for a top electrode for stable, cost-effective, and high-performance PSCs. Apart from these bulk metal electrodes, various innovative electrodes including carbon black,[55,56] silver nanowire (NW) (AgNW),[57,58] carbon nanotubes (CNTs),[59–61] poly(3,4-ethylenedioxythiophene):poly(styrene-sulfonate) (PEDOT:PSS),[62–64] and dielectric/metal/dielectric structures[65,66]

have been attempted as top electrodes with good stability and cost-effectiveness. Beyond the basic requirements such as manufacturing cost, operational stability and high PCE, for specific applications in MPS, the electrode should also meet suitable mechanical properties.[67] These properties include not only the mechanical flexibility of the electrode under bending conditions, but also the adhesion characteristics with its adjacent layer (i.e. underlaying CTLs) to ensure mechanical integrity of the device, which otherwise will lead to mechanical delamination of top electrode from the bottom device during harsh or repeated bending conditions, leading to product failure. From a manufacturing perspective, simpler manufacturing processes of the top electrode would be more favorable.[61–63] Conventional metal thin-film electrodes are generally based on vacuum thermal evaporation process which requires high energy consumption and tedious process steps. Alternative top electrodes need to be compatible with simpler and less energy-consuming processes such as mechanical transfer or solution processes.

Recently, biomimetic electrodes have been proposed in the energy sector. For example, a "biomimetic ant-nest electrode structure" has been proposed in the lithium–sulfur battery (Li–S battery).[68] The "ant-nest-like" electrode can be fabricated using three easy processing methods, including ball-milling (for slurry mixing), doctor-blading (for laminate casting), and a sacrificial method (for porous creation), with CNT being the conductive additive to ease electron transportation and poly(9,9-dioctylfluorene-co-fluorenone-comethylbenzoic ester) (PFM) being the conductive binder (**Figure 4b**). Such a design is inspired by the naturally superefficient ant-nest network, which is well-known for its high spatial usage capable of abundant storage, and the multi-interconnected channels allowing for efficient and fast food transportation.[69] Following this scenario, shortening the travel time for charge carriers in PV devices by means of delicately designed nanostructures could secure a more efficient charge transport and thus minimize scattering losses during transport. Design of such a nanostructure for efficient transport is not easy, but could be modeled from existing bio-prototypes. The 'foraging trail networks' established by ants could be a good example. As shown in **Figure 4a**, wood ants can build the foraging trail networks that provide a shorter travel time for the foraging ants to deliver the information of the food source. Foraging ants use attractive trail pheromones to guide their nestmates to food or water, use a repellent pheromone to mark unrewarding paths, and concentrate the signal at trail bifurcations (or decision points), thereby forming an information delivery network. Such a network is built with low construction costs and low maintenance efforts but displays high message transport efficiency.[70] Similar to this foraging trail network, many other efficient biological transport systems have been discovered and investigated in different species, such as ants and bees. For example, in ant colonies, an individual ant can only do simple tasks but millions of ants can collectively build an intelligent network with higher level intelligence complex behaviors like foraging for food, raising aphid "livestock," building nests, waging war with other colonies and burying their dead. This interaction of individual components with simple behaviors to produce a whole network with complex behaviors is a new research field called 'emergent propriety' in the neuroscience branch of biology. The 'emergent propriety' has been found in many bio prototypes such as cells (as components of vascular networks), mycelia (as components of fungal networks) or individual insects (as components of social insect foraging networks).[69] Specifically, fungal mycelial networks can realize efficient transportation and robustness against damage,[71] slime molds can create networks that balance transport efficiency and robustness,[72] and these natural 'smart' networks at different biological levels point to the impressive ability of self-organized intelligent systems that satisfy specific goals. Mimicking this 'emergent propriety' has been proposed to develop the next-generation of non-von Neumann computation[73,74] and artificial intelligence's (AI's) life 2.0.[75] For smart transport and collection of charge carriers in electrode, another well-known example is the natural leaf, exhibiting high mass transport efficiency, which has been widely used in biomimetic electrodes. In a natural leaf, the "hierarchy" vein structures embedded in spongy leaf cells can efficiently deliver water and minerals to every single leaf cell (will be specifically discussed in the section of **3.2 Bottom Electrode**). In parallel, the leaf can also manage the light usage efficiently. **Figure 4c** illustrates the leaf body composed of palisade cells, spongy cells, and veins. It should be noted that palisade and spongy cells can scatter the sunlight by the refractive index mismatch between the cells and intercellular air spaces, leading to a high light usage. The palisade cells also

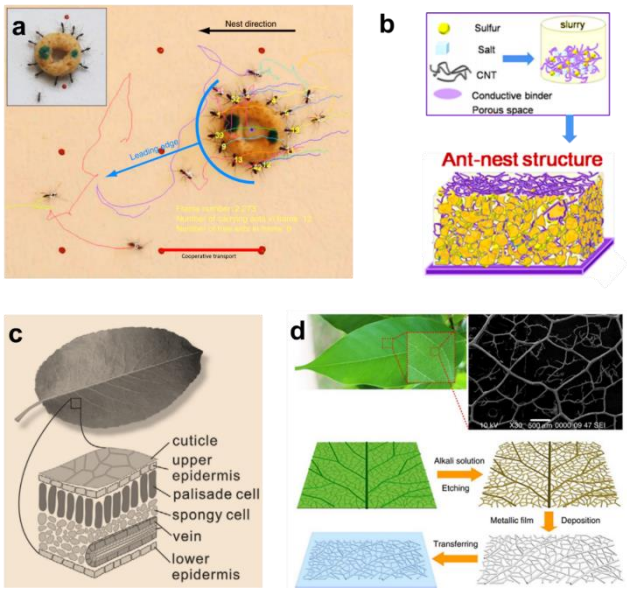

Figure 4 Biological network and their electrical mimicker. (a) Ants' cooperative transport network. Snapshot from a tracked movie of trajectories of different ants, adapted with permission from Ref.[76], Copyright 2015 Springer Nature. **(b)** Porous ant-nest structured Li–S electrode (CNT-nest-S), adapted with permission from Ref.[68], Copyright 2016 American Chemical Society. **(c)** Photograph of a leaf and schematic of its internal anatomy, adapted with permission from Ref.[77], Copyright 2020 WILEY-VCH Verlag GmbH & Co. KGaA, Weinheim. **(d)** Morphology and extraction of leaf vein network, with corresponding optical, SEM images of the leaf and fabrication method, adapted with permission from Ref.[78], Copyright 2014 Springer Nature.

Table 1 Summary of Physical and Chemical Properties of Common Optical Polymers. This table comes from Ref. 76

Polymer	Thickness (mm)	Total light transmittance (%)	Retardation (nm)	Refractive index	Glass transition temperature (°C)	Thermal expansion coefficient (ppm/°C)	Water absorption ratio (%)	H_2O barrier (g $m^{-2}day^{-1}$)
PI	0.1	30 ~ 60	Large	N.A.	<300	8 ~ 20	2.0 ~ 3.0	N.A.
COC	0.1	94.5	7	1.51	164	70	< 0.2	N.A.
PES	0.1	89	< 10	1.6	223	54	1.4	80
PC	0.1	92	20	1.59	145	75	< 0.2	N.A.
PET	0.1	90.4	Large	1.66	80	33	0.5	9
PEN	0.1	87	Large	1.75	150	20	0.4	2

guide the incident light towards the deeper layer for effective light capture as well as an enhanced interfacial reflection. The spongy cells with large numbers of cell–air interfaces give rise to an internal light scattering effect that elongates the light path. Such a natural "optical meta-structure" can further tune the fractions between forward- and backward-scattered light through designing the population and geometry of the cells. **Figure 4d** demonstrates utilizing these natural leaf vein structure as a transparent network-electrode. Specifically, a leaf is etched to eliminate the organic material and cells and keep the vein scaffold network, which is then coated by metals to form a mesh network electrode. Overall, natural structural design of the top electrode (back contact) enabling optimized optical management for enhancing light usage in PSCs will benefit the device efficiency. Following this, "optical meta-structure" could be a promising route for high performance PSCs.

3.2 Bottom electrode

In contrast to the reflection role of top electrode (back contact), the bottom electrode (front contact) of PSCs is responsible for transmitting incident solar light to the inner perovskite light absorber as well as collecting free charge carriers from perovskite. Therefore, it should not only possess suitable electrical properties, including sufficiently high electrical conductivity and suitable energy level to match with that of the photoactive layer, but also high-level light-transparency allowing sufficient light to pass through. In conjunction with the PV-MPS, an additional attribute of the bottom electrode should be a qualified flexibility, allowing a large degree of mechanical deformation of the PV-MPS devices. Such a flexibility requirement can be achieved by using ultrathin polymer layers of high light transmittance. **Table 1** summarizes the polymeric candidate with physical and chemical properties for optical use.[76] Clearly, conventional polymers such as polyethylene terephthalate (PET, T_g ~78°C) or polyethylene naphthalate (PEN, T_g ~123°C) have excellent optical transparency >87%, but are limited by the working temperatures. While the aromatic polyimide (PI) displays excellent thermal stability up to 300°C but suffers from poor optical transmittance. Balancing the light transmittance and thermal stability remains one of the most challenging projects for their typical optoelectronic applications. In the case of PSC manufacturing, both charge transfer layers and photoactive perovskite layers can be processed at low temperatures. For example, $MAPbI_3$ film can be processed at low-temperatures (<100 °C).[77–79] Kim et al.[80] carried out early

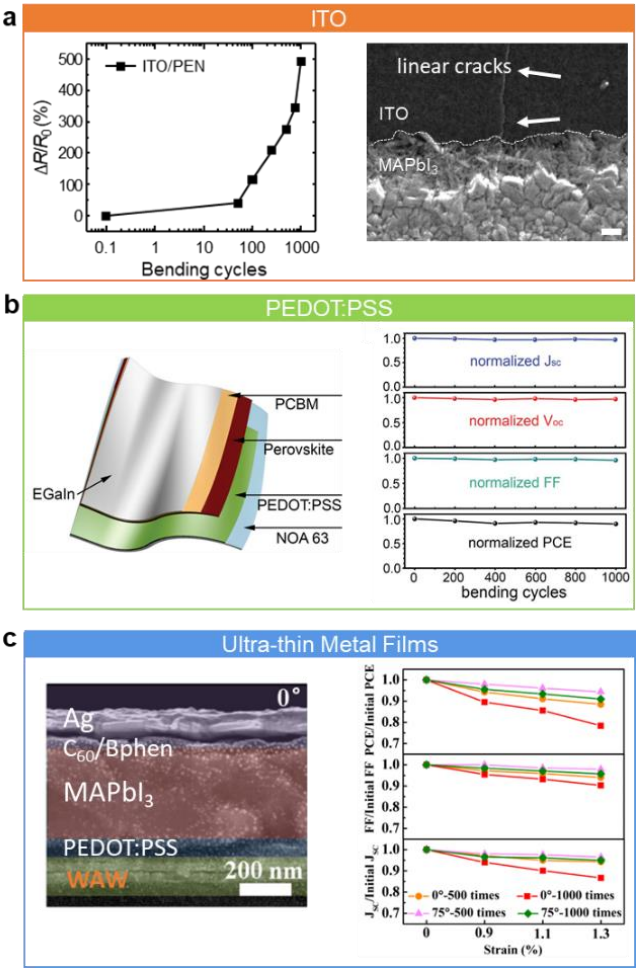

Figure 5 Transparent electrode substrates in flexible PSCs. (a) Plot of sheet resistance of ITO/PEN substrate with various bending cycles (left), and cross-sectional SEM image showing the presence of linear cracks after 1,000 bending cycles (right), adapted with permission from Ref. [86], Copyright 2017 The Royal Society of Chemistry. **(b)** Schematic of the ultra-flexible solar cell based on PEDOT:PSS/NOA63 transparent substrate (left), and normalized solar cell parameters (J_{SC}, V_{OC}, FF, and PCE) of the device after repeated bending at r = 1 mm for 1,000 bending cycles (right), adapted with permission from Ref. [42], Copyright 2015 WILEY-VCH Verlag GmbH & Co. KGaA, Weinheim. **(c)** Cross-sectional SEM image showing the device architecture of flexible solar cell based on WO_3/Ag/WO_3 transparent substrate (left), and changes of device parameters of J_{SC}, FF, and PCE under various strains (right), adapted with permission from Ref. [97], Copyright 2018 American Chemical Society.

works replacing high-temperature sintering processed TiO_2 ETL with a low-temperature atomic layer deposition (ALD)-processed TiO_x layer for ETL, displaying a 12.2% PCE and good bending test results on a PEN/ITO substrate. Directly assembling PSCs from the aforementioned polymeric bottom electrode substrates (via "bottom-up" method) can lead to the MPS-oriented products. Using traditional commercial flexible plastic transparent electrode substrates such as indium tin oxide (ITO)-coated PET and PEN,[81,82] many researchers have made early attempts since 2014. Albeit the initial success in achieving higher performance, the intrinsic drawbacks of these ITO coated PET or PEN include limited material inventory, high price, low optical transmittance, and severe mechanical fragility, which have significantly limited their applicational diversifications. For example, ITO usually shows a significant sheet resistance increase (by over 500% in **Figure 5a**) due to the presence of linear cracks after 1,000 bending cycles (with a bending radius of 4 mm).[83] Therefore, in the MPS-oriented portable PSCs, since the major mechanical limitation comes from the fragility of transparent conducting oxides (TCOs), engineering the mechanical properties of the TCOs and developing alternative flexible transparent electrode becomes the most straightforward strategy.

In order to replace the fragile TCOs, candidates including highly conductive polymers, ultra-thin metal films, metal-NWs- or CNT-based grids or networks have been explored. PEDOT:PSS is composed of conductive PEDOT and water-dispersible PSS, which has been widely used in the larger scope of electronics such as light-emitting diode (LED) and solar cells.[84] The PSS has dual functionality of electrical doping and desolating the PEDOT in water.[85,86] Tuning the doping level through additional dopants such as H_2SO_4 can further improve the overall electrical conductivity of the PEDOT:PSS film, increasing from 1 S cm^{-1} (Clevios PH1000) to > 4000 S cm^{-1}.[87] Recently, Park et al.[42] utilized the PEDOT:PSS to replace the TCO as the bottom electrode substrate for PSCs. By employing a structure of NOA63/highly-conductive PEDOT:PSS/Perovskite/Phenyl-C_{61}-butyric acid methyl ester (PCBM)/EGaIn (**Figure 5b**), the resultant PSC exhibited over 10% PCE with excellent flexibility (i.e., a recovered PSC from bending under a bending radius of 1 mm displayed a 96.4% efficiency maintenance). Alternatively, ultra-thin metal films have also been employed as the transparent electrode substrates for a long period. Such an ultra-thin metal film can be either a single continuous film or sandwiched between two dielectric layers.[88] As noble metals such as Ag and Au have low electrical resistance (1.6-2.4 mΩ cm^{-1}), they are the most frequently used ultra-thin metal electrodes. It should be noted that such a transparent ultra-thin metal electrode can also be used as top electrodes in either single junction PSCs or tandem PSCs. For example, Lee et al. employed Cu (1 nm)/Au (7 nm) as the top transparent electrode for a single-junction PSCs built upon a Ti foil substrate, achieving a 14.9% PCE.[89] The major challenge in an ultra-thin metal electrode is the trade-off between the electrical conductivity and the optical transmittance. Flexible PSCs using ultra-thin metal electrodes, such as a sandwiched structure of "aluminium zinc oxide (AZO)/Ag/AZO", the mono ultrathin layer of bare Ag and a ITO coated Ag film, usually exhibit lower PCEs in the range of 6–10%,[90–93] which might be due to the poor perovskite crystals in these early studies. Recently, Liu et al.[94] constructed the microstructured WO_3/Ag/WO_3 (WAW) multilayer transparent electrodes, through a glancing angle deposition (GLAD) method. **Figure 5c** shows the device configuration and mechanical stability. The resultant flexible device displays a PCE of 13.79% and a 90.97% retainment of initial PCE after 1,000 bending cycles under a maximal strain of 1.3%.

Metal-NWs- or CNT-based grids or networks have also been utilized as the transparent electrode. These grids or networks exhibit excellent electrical conductivity, broad spectral transmittance, and super mechanical flexibility, being widely applied as the transparent conductive electrodes (TCEs) in various optoelectronics. More importantly, their grids or networks are composed of fibrous conductive polymers[79,95,96], metal NW[23,97,98] and CNT,[67,99–101] making them good candidates to form a "leaf vein" network architecture.[102] The natural designed "leaf vein network" system consists of a two-dimensional network composed of branches having different diameters at different scales. Such leaf vein networks[103,104] play an important role in the photosynthesis by supplying nutrients and water to the leaf cells and transport away the photosynthesized carbohydrates to other parts of the plants. Meanwhile, these networks also serve as a flexible backbone for ensuring mechanical stability of the leaf.[105,106] **Figure 6a** displays an example of a *Magnolia liliifora* leaf vein network. The natural vein network has been designed into a highly efficient style to simultaneously ensure bidirectional transport and provide sufficient mechanical stability. Such a transport function of the "leaf vein networks"[105] shares many characteristics with the electrical electrodes applied in photochemical cells, solar cells, LEDs, Li-ion batteries and supercapacitors,[107] where electrical current can be collected or distributed more efficiently. The high-efficiency transport in "leaf vein networks" can be ascribed to the hierarchical structures, consisting of the *petiole*, *midrib*, and *secondary and lower-order veins* (**Figure 6a**). A gradual thickening from secondary veins towards the midrib and the petiole reflects the variation in the amount of resources being transported along network. The supply of water and nutrients (yellow arrows in **Figure 6a(i)**) attenuates from the petiole towards the midrib and subsequently to the leaf blade; the photosynthetic product carbohydrates are collected in the opposite direction but with increasing amounts (red arrow in **Figure 6a(i)**). These lower-order veins connect the secondary veins to midrib, rendering an interconnected network, which ideally provide a bidirectional transport between leaf cells and other part of the plant, playing an important role in collecting and distributing organic material to the plant. For electronics, the bottom electrode substrate (front electrode) can also be designed in a similar way, where metal fingers collect the local currents and transport them towards the metal bus bars and subsequently to the strings. As shown in **Figure 6a(ii)**, such a design has been well applied in Si-PV

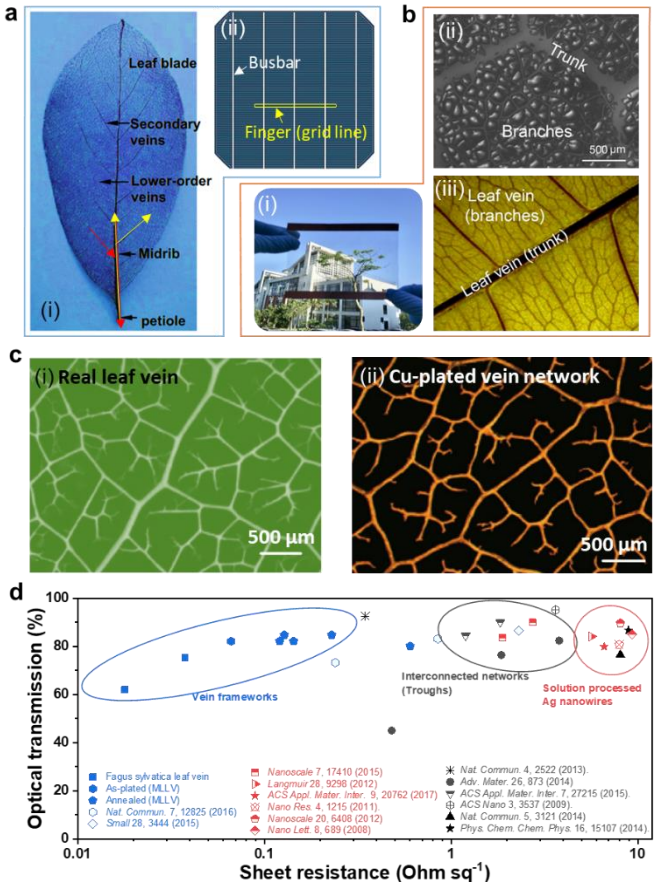

Figure 6 Leaf vein design of TCE. (a) (i) Architecture of a leaf vein network, adapted with permission from Ref.[112], Copyright 2020 Springer. (ii) Image of a typical three-busbar solar cell, adapted with permission from online sources[133]. **(b)** (i) The photograph of a flexible WO_3/Ag hierarchical metal grids (HMG) film. (ii) SEM image of the flexible WO_3/Ag HMG film (iii) The photograph showing the hierarchical structure of a leaf, adapted from Ref.[111], Copyright 2020 Elsevier. **(c)** An optical microscope image of (i) *Magnolia liliiflora* leaf vein, (ii) Cu-plated leaf vein, adapted with permission from Ref.[112], Copyright 2019 Springer, and **(d)** a literature survey for the leaf vein-like transparent electrodes summarizing different materials with respect to optical transmission and sheet resistance.

panels where the photo-generated current is first collected by the fingers (grid line) and then be converged to the bus bars. Li et al.[108] reported the large-area flexible transparent electrodes based on such "leaf vein-like" silver hierarchical-metal-grids (HMG) consisting of mesoscale first-order vein ("trunk") and microscale secondary vein ("branches") (**Figure 6b(i)**). As can be seen in **Figure 6b(ii)**, the branched grids uniformly distribute the conductive pathways and the laser-etched trunk grids can converge the current from the branch. Meanwhile the grid structure also provides a reasonably high optical transmittance (~81%) with low sheet resistance (1.36 Ω sq^{-1}), through optimal geometrical design of the grids' widths, spaces, and the sizes of the colloidal crackle patterns in the branch. Although such an HMG is aimed for the application of electrochromic smart windows, directly using this flexible and transparent HMG as bottom (front) electrode in PSC is promising. Jia et al.[109] also reported the vein-like TCE based on copper electroless deposition[110] on a leaf vein scaffold. They first chemically etched the tissues and cells on a real leaf and then dried and flattened the vein network as a scaffold template for copper electroless deposition.[110] **Figures 6c(i)&(ii)** compare the micrographics of a real *Magnolia liliifora* leaf vein (MLLV) with a Cu-plated MLLV network prepared via electroless deposition for thirty minutes.[109] As a result, such vein-like transparent conducting electrodes display ultralow sheet resistance of <0.1 Ω sq^{-1} (much lower than that of ~ 7 Ω sq^{-1} in PET/ITO), broadband optical transparency >80%, and high current density transport capability >6,000 A cm^{-2}. It should be noted that there have been various methods developed to construct the metal wire network/grid mimicking this leaf vein like TCE. According to the metal material classification, Cu nanowire networks,[111] solution-processed Ag nanowire networks,[111–122] lithographically fabricated metal meshes,[123] novel approaches obtained cracked polymers,[124] cracked TiO_2 [125] and cracked silica nanoparticle thin layers,[126] lithography assisted In_2O_3 grain boundary,[127] and metal nanotrough-like networks[128] have been proposed for TCEs. **Figure 6d** lists the published results of TCEs with R_{sh} <10 Ω sq^{-1} combined with a transmittance (T) of approximately 80%, in which the 'black symbols' denotes those TCEs obtained with interconnected metal networks, the 'red' the solution-processed Ag NW films, and the 'blue' the leaf veins involved frameworks. The state-of-the-art ITO has a benchmark R_{sh} of 7 Ω sq^{-1} and T of 85%. In most prior TCE works, R_{sh} was in the range of 1–10 Ω sq^{-1} with a T of ~80%. It should be noted that leaf veins derived frameworks can exhibit lower R_{sh} than commercial ITO. For example, Han et al.[115] obtained metallized veins through Ag sputtering and achieved a R_{sh} less than 10 Ω sq^{-1}, which is twice as small as that of ITO, meanwhile exhibiting a high transmittance of 85% compared to 80% for PET/ITO. In their work, the metallization was performed by Ag sputtering in vacuum, and Ag was only coated at one side of the vein. The sputtered Ag has an amorphous nature. These factors jointly lead to a relatively high R_{sh}, even though this resistance is still smaller than that of ITO. Yu et al.[129] employed a polymer-assisted metal deposition to metallize the leaf veins, which enhanced the copper wrapping effect on the veins and thus produced a lower R_{sh} towards 0.25 Ω sq^{-1}. However, the poor copper adhesion on carbon-based veins usually leads to copper delamination and low material stability. Recently, Jia et al.[109] utilized the electroless copper plating through the Pd seed layer which can be strongly anchored on the vein surface. With this enhanced Pd binding effect, the copper coating has a stronger material stability able to be stored for over one year.

So far, these metallized vein network TCE are not widely used in PSCs and have only been attempted in several seminal works in OPVs. Properly engineering the geometric and topological layout of the vein network remains the major challenge due to the trade-off between optical transparency and electrical conductance. Recently, Wang et al.[130] designed Cu nanowires with different diameters to construct the hierarchical network for OPVs (**Figure 7a**). They used both large-diameter-long (LDL) Cu NW (with an average diameter of 120 nm and an average length of 150 μm) and small-diameter-short (SDS) Cu NW (with an average diameter of 25 nm and an average length

of 30 µm) as well as an LDL & SDS mixture with different weight ratios to optimize the geometric layout of the vein network. As a result, a hybrid nanowire network composed of 25 wt.% LDL and 75 wt.% SDS nanowires exhibit the best performance due to the highest transparency and conductance at this ratio (**Figure 7b**). For OPVs, the devices employing different types of Cu NW were fabricated. In accordance with the transparency and conductance trend, the device with the 25 wt.% LDL and 75 wt.% showed both highest FF and J_{SC}, which can be attributed to efficient light harvesting and charge collection features of this bottom electrode. (**Figure 7c**). In terms of the geometric optimization of the vein network, Han et al.[131] engineered the *quasi-fractal* (or hierarchical) structure using a natural leaf template. *Fractal* in mathematics is a subset of *Euclidean Space* with a complex dimension exceeding its topological dimension, and has many embodiments in nature such as trees, vertebrate lungs, and circulatory or neuron systems (will be detailed in **Section 4.2 Fractal Neurons**). For leaf vein-like electrode usage in solar cell, the key justification is based on an assumption that the electrical current flow in this structure is analogous to those of fluid, as both current flow and inviscid fluid flow can be mathematically described by the *Laplace's Equation*, fundamentally supporting the electrode application of it.[132] Compared to a uniform network, such a *quasi-fractal* (or hierarchical bar-finger) structure derived from the design of natural leaf vein will have a better performance for charge carrier transport and collection. As described above in **Figure 6**, the network mainly consists of secondary veins with emanated smaller veins, forming an angular network (reticulate veins). The smallest veins have a diameter of ~50–110 µm, being split into shorter branches at each node. Such a network pattern is usually termed as '*umbrella trees*', belonging to non-uniform fractals

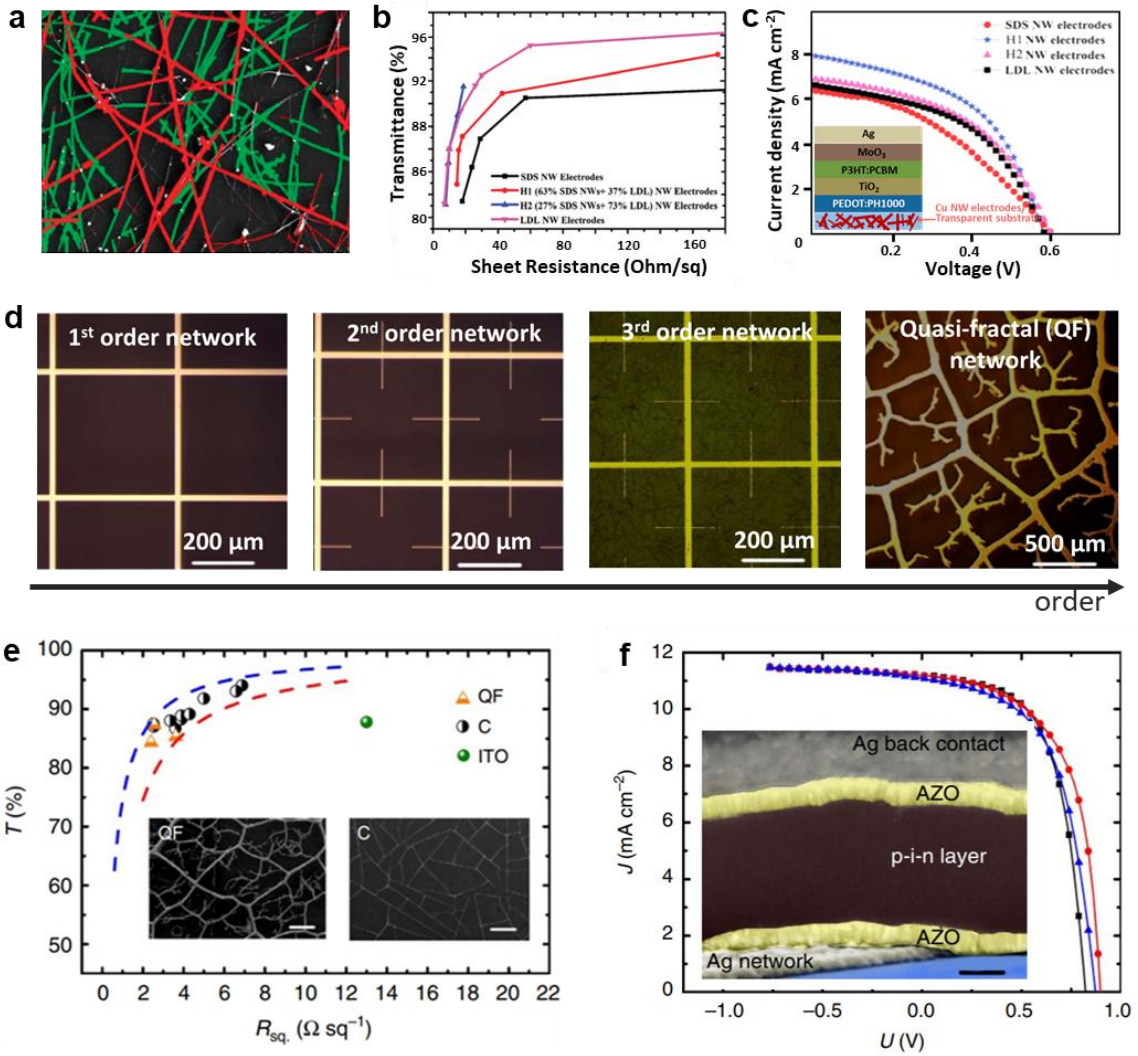

Figure 7 Geometric and topological engineering of conducting transparent electrode (CTE). (a) SEM image of a hybrid nanowire network consisting of 25% long nanowires (marked by red colour) and 75 % short nanowires (marked by green colour). **(b)** Comparison of the transmittance and sheet resistance of electrodes composed of nanowires with different geometrical parameters. **(c)** J–V curves of solar cells based on hybrid Cu nanowire electrodes. Inset: Schematic illustration of solar cell architecture, adapted with permission from Ref.[134], Copyright 2018 The Royal Society of Chemistry. **(d)** Multiple-order and quasi fractal QF network design of CTE. **(e)** Comparison of sheet resistance and resistance of C, QF and ITO film. **(f)** J–V characteristics of the PV cells under based on QF, C, and ITO electrode under AM1.5 illumination. Inset: cross-sectional SEM image of device architecture, adapted with permission from Ref.[118], Copyright 2016 Springer Nature.

with fractal properties pertain to the '*canopy'* which refers to a structure that is formed by the branch tips rather than the whole pattern.[133] Fractal analysis has been used as a powerful tool to characterize the complexity of plant structures. In fractals, branch ordering taxonomy-based method is usually used for fractal dimension determination.[134,135] However, the irregular nature of the venation network in natural leaf vein usually leads to large uncertainty in fractals characterization. Alternatively, angle determination between sub-veins at bifurcation level is an easier way to measure. *Umbrella canopies* typically display a particular branching angle at a given magnification ratio, which is usually named as the smallest angle compatible with self-avoidance (in two-dimension).[133] In fractal geometry of mathematics, a fractal dimension is usually characterized as a measure of the space-filling capacity of a pattern that tells how a fractal scales differently from the space where it is embedded. By determining the branching angle in a leaf vein, a fractal dimension (D_s) of 1.4 ± 0.2 can be determined, falling within the range of 1.4–1.8, which confirms that such a network is an approximate non-uniform fractal.[136] In addition, Han et al.[115] also developed a theoretical fractal model of a leaf vein-like electrode network subjected to three optimization conditions: (i) maximal surface coverage; (ii) uniform current density; and (iii) minimal overall resistance at fixed shading (**Figure 7d**). To maximize the surface coverage, D_s needs to be approximately two. A minimal overall resistance is theoretically incompatible with the requirement of either maximal surface coverage or uniform current density. While with topological extension, the network in the third direction can satisfy both the requirements of maximal surface coverage and uniform current density. As a result, this leaf vein-like quasi-fractal structure (hierarchical) displays a smaller contact resistance of 2.6 **Ω**, compared to that of 14.8 **Ω** from the uniform (non-hierarchical) network and 28.4 **Ω** from ITO as shown in **Figure 7e**. And the quasi-fractal-based PV cell could exhibit slightly higher efficiency of 5.46% than the 5.37% from the non-hierarchical network electrodes (**Figure 7f**).

3.2.1 Metal foil electrode

Above we have discussed the PSCs with a conventional fabrication procedure starting from a transparent flexible bottom electrode, followed by deposition of multiple layers and finished with a top electrode (**Figure 8a**), where the transparent bottom substrate can be either polymeric (plastic) glasses (mentioned above), willow glass (PCE of 13.14% to 18.1% has been demonstrated),[137,138] mica (layered framework of aluminosilicate, a mica/ITO based device displays a PCE of 9.67%),[139] and even paper (PCE of 9.67% has been demonstrated).[140] PSC manufacturing from a metal foil electrode presents an unconventional but promising strategy. **Figure 8b** shows the device assembly procedure, where multiple layers are deposited directly on the foil substrate followed by the addition of the top transparent electrode. As the metal foil substrates are often opaque, the counter (top) electrodes need to be transparent. **Table 2** summarizes the performances of representative flexible PSCs built on the metal foil substrates.[89–92,141–144] Titanium foil (Ti-foil) is the most frequently used foil substrate, as it would be convenient to obtain a TiO_2 layer on top of Ti-foil which is known as an efficient ETL in PSCs. A record PCE of 14.9% has been obtained by Han et al.[89] using a device structure of Au/Cu/HTL/$MAPbI_3$/TiO_2/Ti-foil. This relatively high PCE comes from the high crystalline quality and low oxygen vacancy of the TiO_2 layer. The oxygen vacancies in the oxidized Ti-foil surface determines the effectiveness of the TiO_2 ETL. Minimizing the oxygen vacancy of the TiO_2 ETL benefits the electron collection efficiency and thus improves PCE. Furthermore, such Ti-foil-based PSCs exhibit higher fatigue resistance than those using conventional ITO/PET substrate, by

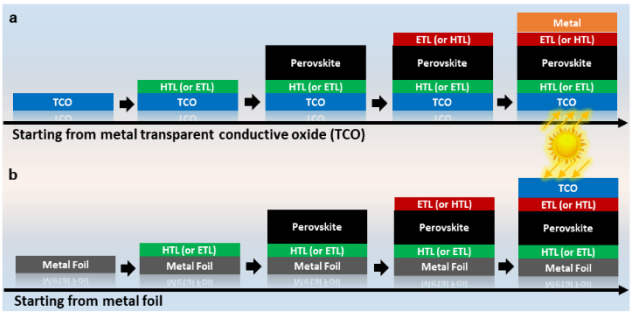

Figure 8 Schematic illustration for two different fabrication procedures of perovskite solar cell. (a) Manufacturing of perovskite solar cells using transparent conducting substrate (*e.g.* ITO/Glass) as bottom electrode. **(b)** Manufacturing of perovskite solar cells using metal foil as bottom electrode.

Table 2 Summary of the performances of flexible perovskite solar cells based on metal foil substrates.

Device Structure	Active Area (cm^2)	J_{SC} (mA cm^{-2})	V_{OC} (V)	FF	PCE (%)	Ref.
Ti foil/compact-TiO_2 /mesoporous-TiO_2/$MAPbI_3$/Spiro-OMeTAD/Ag	0.135	9.5	0.899	0.73	6.15	91
Ti foil/TiO_2/$MAPbI_3$/Spiro-OMeTAD/Ag NWs	0.135	16.48	0.918	0.49	7.45	137
Ti foil/SiO_2/TiO_2/$MAPbI_3$/Spiro-OMeTAD/Ag/ITO	0.135	18.5	0.998	0.61	11.01	90
Ti foil/TiO_2/Al_2O_3/$MAPbI_{3-x}Cl_x$/Spiro-OMeTAD/PEDOT:PSS/(transparent conductive adhesive)/(PET film with embeded Ni mesh)	N.A.	17	0.983	0.61	10.3	92
Ti foil/TiO_2/$MAPbI_3$/Spiro-OMeTAD/Cu/Au	0.14	17.9	1.09	0.74	14.9	89
Ti foil/TiO_2 nanotube/$MAPbI_3$/carbon nanotube (CNT) networks composite with Spiro-OMeTAD	0.16	14.36	0.99	0.68	8.31	138
Cu foil/CuI/$MAPbI_3$/ZnO/Ag	0.1	22.5	0.958	0.594	12.8	139

showing a 100% initial PCE maintenance after bending of 1,000 times at a bending radius of 4 mm. In addition to Ti-foil, copper foil (Cu-foil) has also been used in flexible PSCs. Ahmadi et al.[144] prepared cuprous iodide on a Cu-foil by exposing the precleaned Cu-foil in iodide vapor, which serves as the hole transport layer (HTL) for the device. After being coated with perovskite, the device is then coated by a ZnO ETL followed by a spray coating of Ag NWs as the top electrode, which exhibited a PCE of 12.80%. These foils-based solar cells show good feasibility of perovskite PV-MPS but present challenges in top transparent electrode manufacturing and in limited mechanical stretchability of the bottom metal foils.

3.2.2 Fiber electrode for fabrics

Fiber-structured energy devices, including the fiber-based triboelectric nanogenerators, batteries, supercapacitors, sensors, chromic devices, and solar cells, etc., have recently received enormous attention due to their high potential being integrated into wearable textiles.[145–160] By weaving these fiber devices into clothes with proper fibrous structural design, clothing integrated MPS can be easily obtained. As described in **Figure 9a(i)**, this will provide access to multiple built-in sensors, small electronics and applications integrated within the MPS clothing. **Figures 9a(ii)** and **9a(iii)** show the concept that a PSC fiber device can be incorporated into the smart fabrics to power multiple functional electronics. Research and developments of these MPS fabric power plants may be further stimulated by the fast-growing need for near-body/on-body electronics.[161,162] From a technical point of view, compared to the common thin film-based PSCs, many technical challenges, such as complication of fiber axial perovskite synthesis, curvature interface manipulation, and nonuniform light exposure on PSCs with adoption of a 1D-fiber (cylinder-type) geometry, need to be considered. In any case, the device fabrication starts with the fiber electrode. In 2014, Qiu et al.[163] utilized a stainless-steel fiber as the backbone cathode for a fiber PSC device. **Figure 9b** shows the device structure. The steel fiber was sequentially dip-coated by an *n*-type TiO_2 compact layer and mesoporous layer, followed by the perovskite being infiltrated into the mesopores. The HTL was encrusted through dip coating and the device was finalized by the dry-drawn from a spinnable CNT array of transparent multi-walled CNTs (MWCNTs) with an average diameter of 10 nm. The fiber-shaped PSCs delivered a PCE of 3.3%, with open-circuit voltage (V_{OC}) of 0.664 V, short-circuit current density (J_{SC}) of 10.2 mA cm^{-2}, and fill factor (FF) of 0.487, demonstrating the earliest attempts for PSC fabric. In contrast, Li et al.[164] employed multi-twisted CNT as the backbone core (**Figure 9c**). They chose the highly flexible CNT fiber that is directly spun-twisted from a spinnable CNT array as the anode and sequentially coated thin layers of compact n-TiO_2, meso-TiO_2, $CH_3NH_3PbI_{3-x}Cl_x$, poly(3-hexylthiophene)/single-walled carbon nanotube (P3HT/SWNT), and silver (Ag) nanowire network from the inside out, and used Ag nanowire network as the outside effective contact bridging the neighbouring CNT fiber electrodes. The device exhibits a champion PCE of 3.03%, with a V_{OC} = 0.615 V, J_{SC} = 8.75 mA cm^{-2}, FF = 56.4% and could withstand

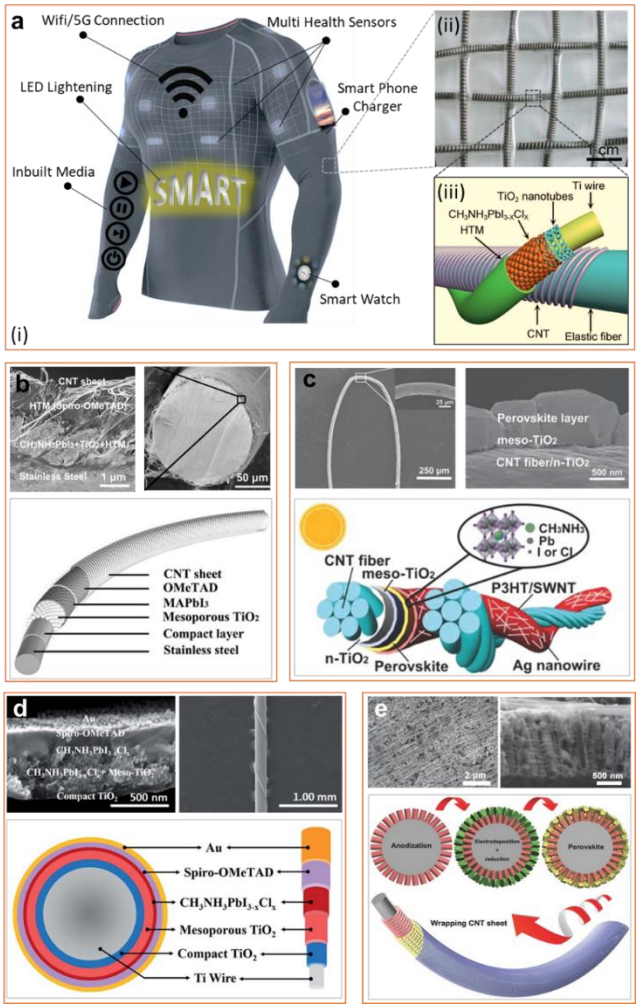

Figure 9 The design of PSC fibric device. (a) (i) Illustration for a smart clothing integrated with electronic devices, picture credits to an online resource.[170] (ii) Photograph of a fibric perovskite solar cell. (iii) Schematic illustration for the structure of the fibric perovskite solar cell, adapted with permission from Ref.[171], Copyright 2015 The Royal Society of Chemistry. **(b)-(e)**: The schematic illustration and SEM image showing the structure of **(b)** a wearable double-twisted fibrous perovskite solar cell based on stainless steel, adapted with permission from Ref.[166], Copyright 2015 WILEY-VCH Verlag GmbH & Co. KGaA, Weinheim. **(c)** A design of fibrous perovskite solar cell based on CNT fiber, adapted with permission from Ref.[167], Copyright 2014 WILEY-VCH Verlag GmbH & Co. KGaA, Weinheim. **(d)** A design of fibrous perovskite solar cell based on Ti wire, adapted with permission from Ref.[168], Copyright 2016 The Royal Society of Chemistry. **(e)** Another design of fiber-shape perovskite solar cell based on modified Ti wire and CNT sheet, adapted with permission from Ref.[169], Copyright 2016 WILEY-VCH Verlag GmbH & Co. KGaA, Weinheim.

1,000 bending cycles with no significant efficiency loss. Besides the CNT and steel fiber, Ti wire is another candidate for backbone electrode. Hu et al.[165] utilized the Ti wire as the core backbone for the fiber PSC. As shown in **Figure 9d**, an integrated device structure of Ti/c-TiO_2/meso-TiO_2/perovskite/spiro-OMeTAD/Au has been assembled in a fiber format, where a thin layer of Au nanoparticle (NP) was employed as the top semi-transparent electrode. The device exhibits a 5.3% PCE under AM 1.5 illumination and an apparent

Table 3 Summary of PV parameters of state-of-the-art fiber-shaped PSCs.

Device Structure	J_{SC}(mA cm^{-2})	V_{OC}(V)	FF	PCE (%)	Ref.
Stainless steel/Compact layer/Mesoporous TiO_2/$MAPbI_3$/Spiro-OMeTAD/CNT sheet	10.2	0.667	0.487	3.3	[163]
CNT fiber/Mesoporous TiO_2/$MAPbI_3$/P3HT-SWNT/CNT	8.75	0.615	0.564	3.03	[164]
Ti wire/TiO_2 nanotube/$MAPbI_{3-x}Cl_x$/Spiro-OMeTAD/CNT	3.5	0.63	-	5.22	[167]
Ti wire/Comapct TiO_2/Mesporous TiO_2/$MAPbI_{3-x}Cl_x$/Spiro-OMeTAD/Au	12.32	0.714	0.609	5.35	[165]
Ti nanowire/Compact TiO_2/TiO_2 nanotube/$MAPbI_3$/Transparent CNT	14.2	0.85	0.56	7.1	[166]
Ti wire/Compact TiO_2/Mesoporous TiO_2/$MAPbI_3$/Spiro-OMeTAD/Au	14.18	0.96	0.66	7.53	[168]

8.4% efficiency in a diffuse model. Qiu et al.[166] further modified the Ti wire (core backbone of the fiber cell device) and used the transparent aligned CNT sheet as the counter electrodes (**Figure 9e**). With an anodization process, an array of TiO_2 nanotubes were radially grown on the Ti-wire, showing a mesoporous configuration. Then a porous, sponge-like PbO layer was coated on the TiO_2 array using cathodic deposition, followed by addition of hydroiodic acid to form the PbI_2 precursor of perovskite. After conversion into perovskite through dipping into methylammonium iodide (MAI) solution and being coated with HTL and top electrode (wrapped by a transparent CNT tape with 80% transmittance in 400–800 nm spectrum range and 500 S cm^{-1} electrical conductivity), the device shows a PCE of 6.8%, with a V_{OC} of 0.852 V and J_{SC} of 16.1 mA cm^{-2}. Further covering a 5 nm Ag outside the CNT led to a PCE increase to 7.1%. **Table 3** summarizes the device performance parameters of the fabric PSCs. Overall, the novel fabric structure and high performance of PSCs could help pave the way for future self-powering e-textiles. Composing above fiber-based solar cells into wearable textiles require properly weaving them in accordance with an appropriate fibrous structural design. Examples of fibrous structures are observed in many processes in nature, with one well-known example being the spider web.[167] Different fibrous structures will have different weights, energy densities, and mechanical properties in the final MPS products. In nature, in order to confer certain mechanical properties, the fibers are usually arranged in a specific pattern. For example, in the palm trunk of *coconut palm*, there are three types of fibers with different patterns located at different regions in the trunk (the cortex, the peripheral zone and the central zone): the outer surface cortex is composed of numerous longitudinal fibrous strands; the periphery contains a narrow layer of parenchyma cells and high density vascular bundles forming a hardened support for the tree; the central cylinder consists of ground

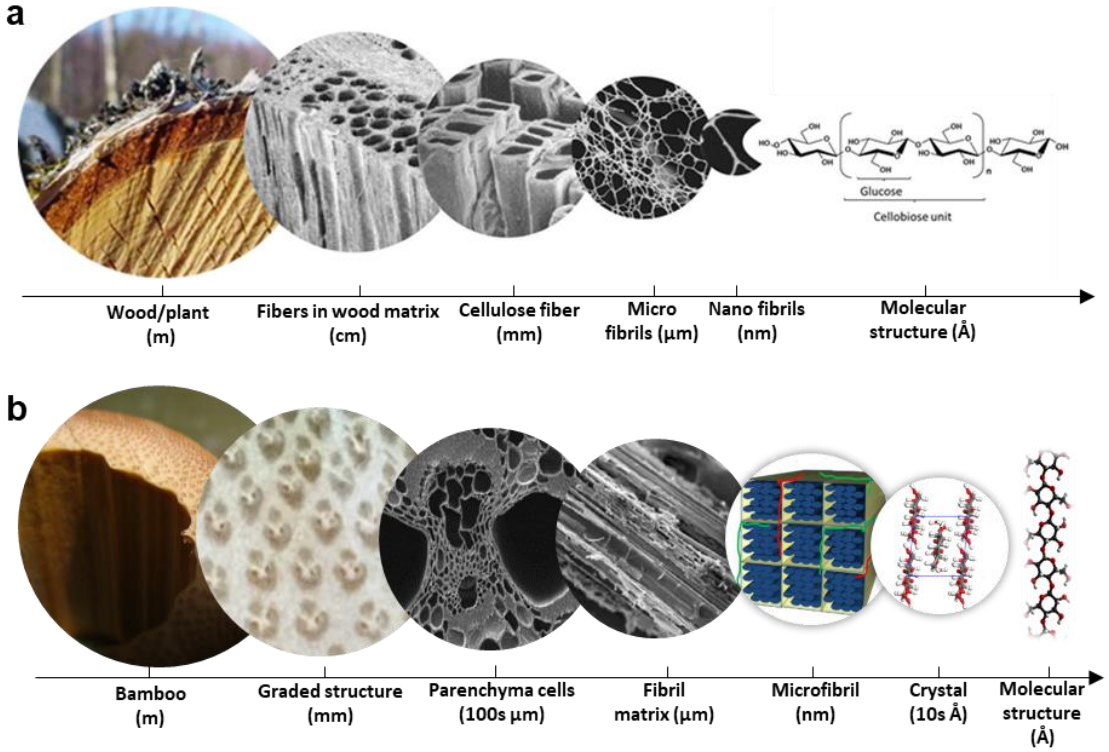

Figure 10 Microscopic structures in natural plants. (a) Schematic illustration for the structure of wood fibril bundles at different scales, adapted with permission from online resource.[183] **(b)** Schematic illustration of the hierarchical structure of bamboo, adapted with permission from online resource[184], and Ref.[185–189], Copyright 2011, 2015, and 2018 Springer Nature, 2016 Cabi, and 2019 Frontiers.

parenchymatous tissues scattered with vascular bundles with higher moisture density and responsible for longitudinal matter transport.[168,169] Weaving the fiber into different patterns with involvement of other types of fiber components could diversify the functionalities. Similar to palm trunk, in wood there are parallel tubular cells which are reinforced with cellulose fibrils in a spiral wound, embedded in a matrix of hemicellulose and lignin. The winding angle of fibrils leads to different mechanical properties (such as stiffness and strength[170–173]) for the wood. **Figure 10a** shows the wood fibril bundles at different scales. Bamboo is another example, and is one of the strongest natural fiber composites. **Figure 10b** shows the hierarchical structure of bamboo, where the vascular bundles in the parenchyma matrix are surrounded by supporting fibers. Cellulose microfibrils reinforce the intertwined hemicellulose-lignin matrix.

Overall, in terms of some specific requirements on the mechanical properties for the MPS products, these wood and bamboo structures inspired innovations are promising. For example, Sun et al.[174] proposed a bamboo-like graphitic carbon nanofiber for energy storage application. The design was inspired by the bamboo structure where there is a periodic distribution of interior holes along with the length and graded pore structure at the cross-section, which would not only enhance the stability with different mechanical deformations but also provide higher surface area for the access of electrolyte and lower ion-transport resistance. The final device exhibits excellent performance, even being operated under conditions of bending at 90° and twisting at 180°. Recently, Zhu et al.[175] reported a bamboo derived biodegradable & biocompatible transparent conductive electrode for PSCs, which exhibits extreme flexibility and light-weight properties. The bamboo-based bioelectrode PSCs display a PCE of 11.68%, the highest among all biomass-based PSCs. Meanwhile, the flexible device has a highly bendable mechanical stability, maintaining over 70% of its original PCE after 1,000 bending cycles at a 4 mm curvature radius. Cai et al.[176] developed an efficient HTL consisting of P3HT and bamboo-structured CNT for PSCs. The addition of bamboo-structured CNT (1–2 wt.%) led to over one-order-of-magnitude higher conductivity, and two-order faster interfacial charge transport. These attempts are good examples of how the structured bio-inspired materials could lead to higher mechanical performance for solar cell. Nevertheless, weaving the fiber-like solar cells into a fabric patterns by means of bio-inspired pathways (e.g., spider web) or some art forms (e.g., kirigami and origami) might lead to a fabric PV-MPS with unexpected mechanical performance.

3.3.3 Paper-electrode substrate

To extend applied potential in MPS, PSCs with extreme mechanical stretchability is of great interest. This will require the PSC to have a recoverable device performance after various mechanical deformations including stretching, twisting, bending, and delamination. Many prior efforts have mainly focused on bending durability only, leaving stretchability vastly unexplored. Although the aforementioned fiber-structured device and textile-type devices[18,23,40] have shown great robustness against various mechanical deformations[165,166,177–179], there is still technical challenge to balance the mechanical performance with PCE. The layer-by-layer coating on a metal-fiber backbone needs to be uniform and should have minimized defect density, otherwise the PCE will drop significantly. The connection of individual fiber-devices into a whole fabric needs to be carefully designed

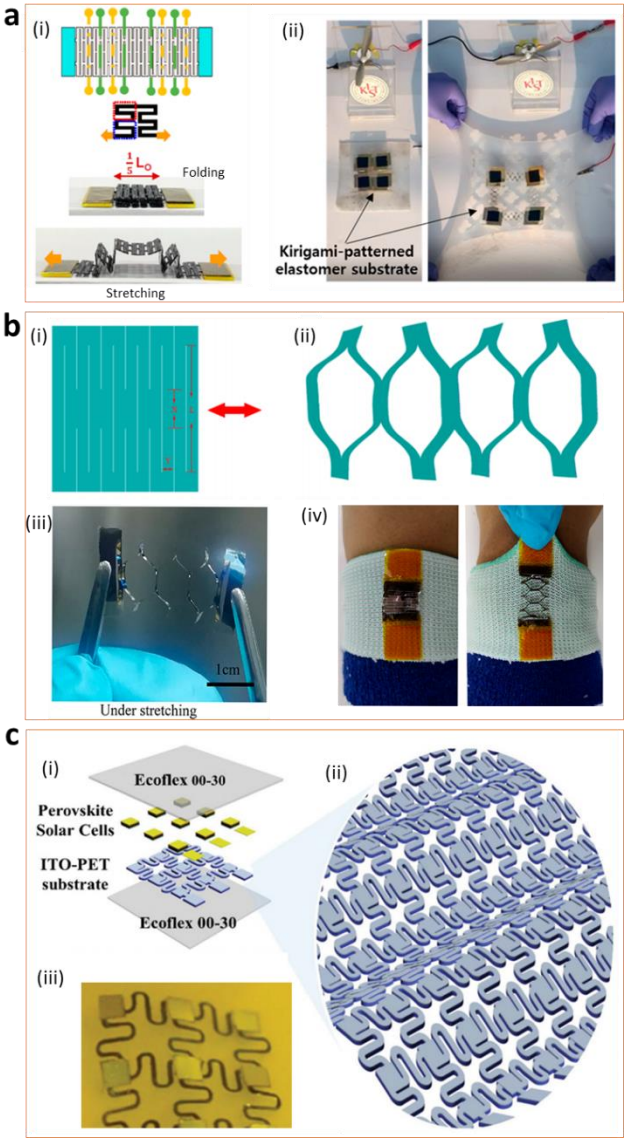

Figure 11 Adaptation of '*kirigami*' and '*origami*' strategies in designing flexible perovskite solar cells. (a) (i) Schematics of the *kirigami*/*origami* approach to achieve stretchable flexible PSC with high coverage. (ii) Photographs of the stretchable PSC module connected to a fan under the sunlight, adapted with permission from Ref.[195], Copyright 2019 American Chemical Society. **(b)** (i)-(ii): Schematic illustration for the structure using *kirigami*-based cutting strategy at (i) initial state and (ii) stretching state. (iii) Photograph showing the *kirigami*-based PSC device under stretching state. (iv) Photograph of *kirigami*-based PSCs mounted on a human wrist accommodating the stretching deformation, adapted with permission from Ref.[196], Copyright 2020 American Chemical Society. **(c)** (i) Schematic illustration showing the architecture of the *kirigami*-structured PSC with serpentine interconnect design. (ii) Zoom-in view showing the detail of serpentine interconnect substrate design. (iii) Photograph of the *kirigami*-structured PSC device with serpentine interconnects, adapted with permission from Ref.[197], Copyright 2020 The Royal Society of Chemistry.

to reduce the longitudinal series resistance for charge transport. For the textile-type device where manufacturing of multiple layers is deposited on a textile, the rough and curved surface of the textile could induce many unwanted interface issues for the whole device. Alternatively, another design could be the "island-bridge" structure (consisting of "device islands" and "wire bridges" connecting these islands, derived from the silicon-based stretchable electronics[180] and frequently utilized for stretchable systems[181]), which have already been applied in PSCs. The "island-bridge" design first fabricates the device on a paper-electrode substrate, followed by a papercraft with proper post-cutting (*kirigami*) or -folding (*origami*).[182] This enables the PSCs to preserve their initial PCE under large mechanical deformations such as stretching, bending, and twisting. Jo et al.[183] reported the PSCs based on the *kirigami*- and *origami*-strategies demonstrated 400% stretchability and high areal coverage. The main drawback of the "island-bridge" design is the trade-off between the coverage-area and stretchability. The higher ratio of the "bridge" area will produce a better stretchability, but will lower the total output power due to the smaller area of the "device island" (geometrical fill factor). **Figure 11a(i)** shows a solution to this trade-off dilemma. By adopting the *origami* folding, the bridge can be folded up and stacked under the device region ("island"). This strategy allows an efficient spatial usage (or geometric fill factor) close to 100% (**Figure 11a(ii)**). Meanwhile, the stretchability could be maximized by employing different *kirigami* designs. Li et al.[184] also adopted the *kirigami*-based cutting strategy for a stretchable PSC. **Figures 11b(i)&(ii)** show this cutting design, with the out-of-plane deformation possibly able to sufficiently disperse the stress load, thus increasing the stretchability. The *kirigami*-based PSCs with an optimal geometric design exhibited high stretchability with a strain of 200%, high twistability with an angle up to 450°, and high bendability with a radius down to 0.5 mm. Furthermore, the *kirigami* PSCs displayed a good mechanical endurance with an invariant PCE after 1,000 repetitive stretching, twisting, and bending cycles. **Figure 11b(iii) & (iv)** shows the photograph of *kirigami*-based PSCs mounted on a human wrist with accommodation to the stretching deformation. Qi et al.[185] also reported *kirigami* structured PSCs with serpentine interconnects. **Figure 11c** shows the schematic diagram and photograph of the stretchable PSCs. The yellow area in **Figure 11c(i)** is the gold electrode from which the sub-cells are arranged in arrays. A packaging layer of Eco-flex is further used at both sides of the cell to protect the device. As a result, the obtained devices exhibited a high and stable PCE of 17.68% with a robust mechanical cycling performance of 87% of the initial PCE after 300 cycles of continuous stretching under a large stretching ratio of 80%. The optimized PSC also shows a stable efficiency in harsh environment (80% relative humidity) for 10 days. Overall, research on the stretchable device platforms for PSCs is still at the developing stage. In addition to the "island-bridge" structure,[185] pre-strained wrinkle structure,[18] as well as papercraft-inspired approaches[183–186] have also been investigated to realize the PSC based portable MPS. This will rely on various state-of-the-art fabrication technologies including photolithography, laser processing, and 3D printing, for engineering, optimizing and innovating new device architectures.

4. Charge Transport Layer

PSCs are layer-by-layer stacking-structured devices with the core perovskite layer absorbing the light and generating excited electrons and holes, which need to transfer across multiple interfaces before being collected by the electrodes. Charge transfer layers (CTL) are responsible for minimizing the charge losses during the interfacial transfer process. In case of PSCs, multiple HTL and ETL materials have been applied following several selection rules of: (i) excellent thermal/photochemical stability; (ii) suitable highest occupied molecular orbital (HOMO)/ lowest unoccupied molecular orbital (LUMO) energy level aligning with those of perovskite; (iii) optimal charge carrier mobility for efficient transport; (iv) good processing ability; (v) good operational phase stability; (vi) low cost and easy attainability; (vii) proper optical transparency. So far, multiple artificial CTL materials including spiro-OMeTAD,[187–191] Spiro-like-based derivatives,[192–202] carbocyclic small molecules,[202–206] nitrogen-, sulfur-, oxygen-, or silicon-containing organics,[207–216] metallomacrocycle-based materials,[217–219] π-Conjugated oligomerics, and other inorganic semiconductors[220] have been utilized as the HTL for PSCs. Meanwhile, metal oxides (e.g., TiO_2, ZnO, SnO_2, WO_3),[221–223] organic *n*-type materials (PCBM, ICBA[224–232]), core–shell nanoparticles,[233] plasmonic nanoparticles,[234–236] etc., have been employed as the ETL for PSCs. Optimal CTL materials satisfying all the aforementioned requirements might lead to a new route towards minimized energy losses during interfacial transport in PSCs. Hence, material expansion from these commonly used artificial materials to some novel functional materials that have not been well recognized yet could be a promising research direction, especially if they are cheaper, more abundant and easier obtainable.

Natural/bio-materials offer such an opportunity. Incorporation of natural bio-semiconductors into electronic, information processing and storage devices, and bio-/artificial-semiconductor interfacing, are growing research areas. New fields at the intersection of synthetic biology and semiconductor technology-Semiconductor Synthetic Biology (SemiSynBio) has been rapidly developing to take advantage of significant efficiency and information processing capabilities from biological systems compared to the best equivalent silicon-based systems. Specifically, deoxyribonucleic acid (DNA) and small cell integrated functional devices, biological/artificial electronics, and biological/artificial coupling systems with high-level automation, have been attempted.[237] Using natural/bio-semiconducting materials not only broadens the material inventory for seeking a suitable CTL material for ultrahigh-efficiency PSCs, but also offer great opportunities to redefine the architecture and manufacturing of PSCs in a more efficient or intelligent way towards MPS-orientated products.

4.1 DNA

4.1.1 DNA charge transport (CT) mechanism

Among those biomaterials of interests, charge transport and relevant charge transfer processes in double helical DNA have attracted huge interests over decades due to their close relevance to the oxidative damage in DNA, which is believed to related to aging and senility of all living creatures.[238,239] In recent decades, research of DNA has discovered long-range charge transport phenomena in DNA and has shown the adaptability in defined nanostructures[240] by proper design and synthesis, further stimulating the research interest in DNA serving as a building block for nanoelectronics applications. As shown in **Figure 12a**, DNA has four chemical bases: adenine (A), guanine (G), cytosine (C), and thymine (T), where A pairs up with T while C pairs with G to form the 'base pair' units. Each base is also attached to a phosphate molecule and a sugar molecule, forming a cluster called a 'nucleotide'. Nucleotides are arranged in two long-strands with a spiral form, called a 'double helix'. The double helix DNA is analogous to a spiral staircase, with the base pairs being the individual steps, while the sugar and phosphate molecules are the vertical railings. Sequencing the base pairs and tuning the pair numbers (coding) of DNA allows for a high degree of variability. Each organism has a unique DNA sequence, which details their genetic information. Human DNA consists of about 3 billion base pairs, with 96% similarity to the DNA sequence of great ape species. With the base pair complexity, charge transfer (CT) behaviour in the DNA double helix can be different. Using different DNA models, multiple mechanisms have been proposed for interpreting the CT along the DNA chains. **Figure 12b** summarizes these mechanisms including (i) ballistic (wire-like) transport, (ii) super-exchange, (iii) A-hopping, (iv) G-hopping, (v) polaronic hopping. Ballistic (wire-like) CT mechanism[241] assumes a delocalized π-bond (created by the stacked nucleobases of DNA) through which the injected charge can propagate. Such a ballistic mechanism was proposed by Barton et al.[241] to rationalize the observations of a picosecond transfer photoinduced CT between rhodium and ruthenium metallo-complexes intercalated in a DNA stack (**Figure 12b(i)**). Super-exchange CT[242–244] assumes well localized donor and

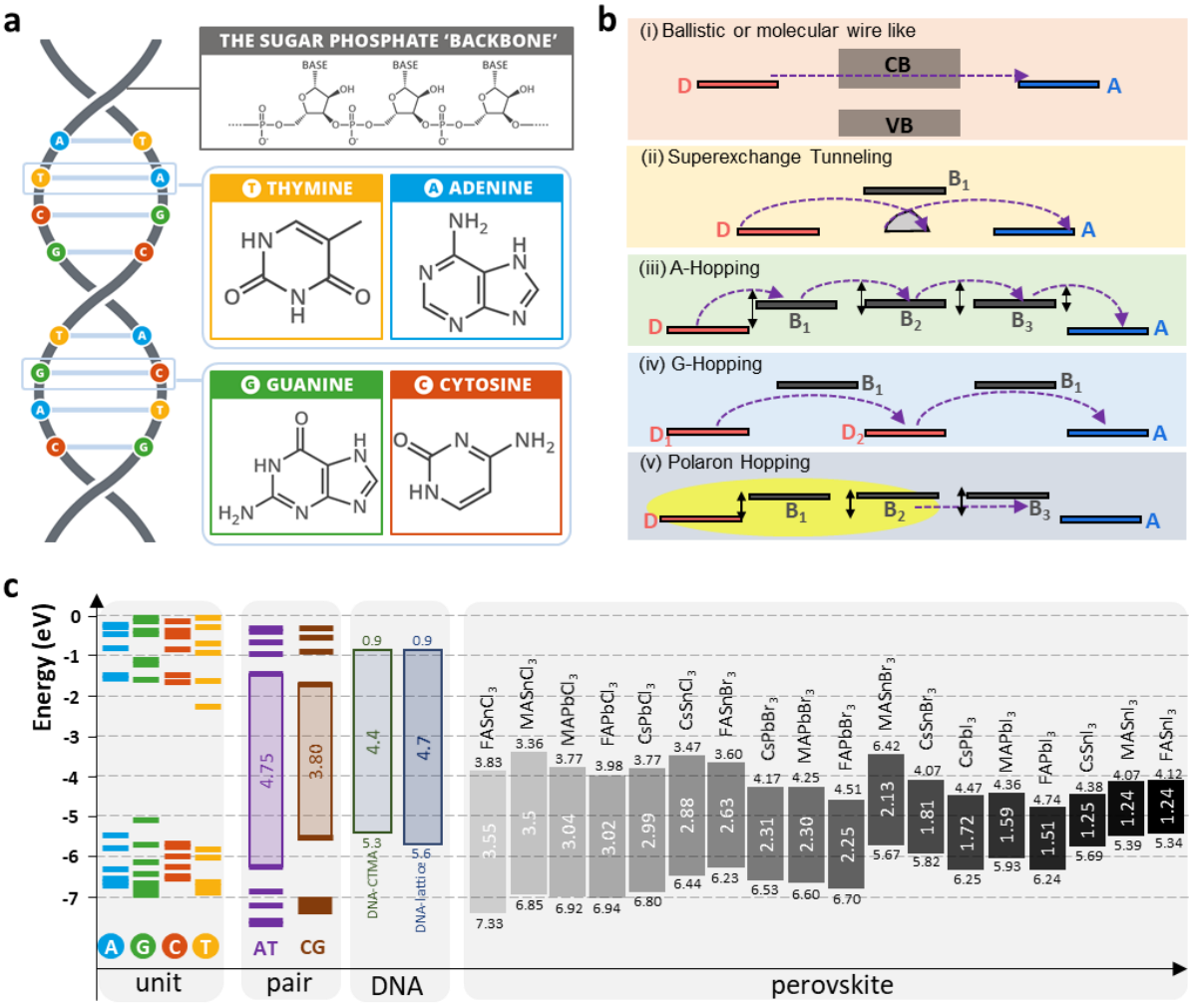

Figure 12 DNA and related transport mechanisms. (a) Schematic illustration of chemical structure of DNA and nucleobases, picture credits to online resource.[267] **(b)** Charge conduction mechanisms in DNA molecules, adapted with permission from Ref.[268], Copyright 2011 Elsevier. **(c)** Energy level diagram of four basic units, two pairs, DNA macromolecules, and various perovskites.

acceptor, which occurs when there are large energy gaps between the donor/acceptor and bridge energies. In this way, quantum tunnelling via the states of the intervening bridge dominates the transport, which has been verified by the theoretical predication of CT in short DNA sequences (**Figure 12b(ii)**). Such an CT mechanism is similar to those in proteins, with an exponential decay constant of ~1 $Å^{-1}$.[244–246] The A-hopping mechanism[247] is a multi-step transport which subdivides the transport into two mechanisms (i) transport between AT pairs and (ii) transport between AT and CG pairs. Charge transport follows incoherent hoping mechanism among the transport between AT nucleobases but changes into a thermally activated injection when transporting from AT to CG pairs (**Figure 12b(iii)**). In G-hopping,[248,249] a hole moves between CG nucleobases, mediated by an intervening AT (**Figure 12b(iv)**). This model has been verified by multiple atomic force microscopy (AFM) and scanning tunnelling microscopy (STM) experiments that the electrical resistance of DNA fragments decreases with an increase in the G-content.[250–252] Polaronic hopping (**Figure 12b(v)**) is related to the electron/hole cloud polarization that is likely delocalized over several base pairs. This polarization arises due to the redistribution of electron density in the DNA themselves[253] and/or due to the interaction with the solvent molecules[254] and/or the thermally activated polaronic motion. The polaron model is used to rationalize experimental data[253] that there is little change in the radical cation migration efficiency through long distance (10–55 base pair) within the DNA. This will lead to a large electron/hole cloud delocalization over several bases, thereby an overall increased conductivity of the DNA.[253]

4.1.2 DNA buffering solar cells

DNA and its derivatives have been applied in organic electronics including organic LED,[255] organic field-effect transistors (OFET) [256] and OPVs,[257,258] by optimizing the interfacial electrical contact between photoactive layers and the electrodes and/or modifying the micromorphology of the complex organics. Recently, Thomas's group[259] found a significant exciton disassociation effect upon interfacing the organic photovoltaic system with the DNA molecules. Several DNA-modified ETLs have been applied in organic solar cells with a device structure of ITO/ETL/P3HT:PC_{70}BM/HTL/Ag (**Figure 13a(i)**). By using an ETL of DNA, ZnO-NPs, or ZnO-NPs/DNA, the photocarrier behaviour exhibited different dynamics at the interface and thereby showing different PCEs. **Figure 13a(ii)** compares the false color NIR transient absorption (TA) maps for the ITO/ETL/P3HT:PC_{70}BM/MoO_3/Ag using empty ETL or a DNA ETL. Incorporation of DNA ETL led to an obvious change in the photobleaching at different characteristic wavelengths labelled by PB1, PB2, and PB3 of P3HT (**Figure 13a(iii)&(iv)**). Spectral cuts at a probe delay of 800 fs of the TA map in **Figure 13a(iv)** show significant variation in PB2 and PB3 features, including a strong blue shift of PB2 from the cell using the ZnO-NPs/DNA ETL. Such an observation suggests that the ZnO-NPs/DNA has a great photo optical effect on the conjugation length and intrachain coupling of photocarriers in the P3HT. Overall, insertion of this ultrathin DNA layer between the photoactive layer and electrode lead to a more efficient carrier extraction as evidenced by a lower population of trapped excited exciton states and faster extraction at intermediate timescale decays (5 and 100 ps). It should be noted in the above work, DNA can also be chemically doped into a *p*-type HTL with preferable energy levels better matching that of the photoactive layers. For example, via a redox reaction with hexadecyl trimethyl ammonium chloride (CTMA), the HOMO can be shifted towards -5.4 eV, perfectly aligning with the valance band maximum (VBM) of $MAPbI_3$ perovskite, while the LUMO of DNA-CTMA can be maintained as high as -1.1 eV. Such a band structure will efficiently block the electron transfer between DNA-CTMA and $MAPbI_3$ perovskite due to a large Schottky barrier for the electron, but will secure an efficient hole transfer due to the formation of an Ohmic contact. Yusoff et al.[260] recently utilized such a DNA-CTMA as the HTL for perovskite solar cells. The well-aligned energy level of the VBM of $MAPbI_3$ with the HOMO of DNA-CTMA minimizes the energy loss for hole transfer and optimizes the magnitude of V_{OC} from 0.90 V to 1.04 V. The LUMO coefficients are located on the Thymine and Cytosine units of DNA. By tuning the ratio and thus the LUMO to a higher level, the DNA-CTMA HTL could efficiently block electrons, reducing the recombination loss and enhancing both the J_{SC} and PCE from 19.20 to 20.85 mA cm^{-2} and from 12.49% to 15.86%, respectively. More recently, our group[261] also incorporated the hole-extraction facilitated DNA into the grain boundaries (GBs) of perovskite film (**Figure 13b(i)**). A 3 nm-thick DNA layer bridging the neighbouring perovskite crystal grain can facilitate the charge transfer across the GBs, increasing the charge carrier mobility by two times from 1.18×10^{-4} cm^2 $V^{-1}s^{-1}$ to 2.43×10^{-4} cm^2 $V^{-1}s^{-1}$. As a result, hole extraction throughout the DNA modified device shows a more efficient process with a faster photoluminescence (PL) quenching (**Figures 13b(ii)-13(iv)**). Consequently, a DNA-modified PSC shows a PCE of 20.63% compared to a 18.43% from a reference cell and the hydrophobic nature of CTMA modified DNA further extends device's lifetime from day-scale towards month-scale.

By exploiting its intrinsic molecular conductive nature, DNA can be an excellent integrant in electrically optimizing the property of functional layers and enhancing the performance of solar cell device. **Figure 13c** summarizes different types of solar cells being incorporated with DNA. It should be noted that PSCs have shown the higher PCE compared to OPVs and represents as the optimal platform of applying DNA engineering. Nevertheless, as DNA itself displays complex and multi-hypothetical charge transfer mechanisms, incorporation of DNA into the perovskite system requires an in-depth understanding from the molecular scale to the macroscale for successful device design and operation. More investigations and theoretical models are required to elucidate DNA/perovskite interfacial charge dynamics.

4.2 Fractal neurons

4.2.1 Fractal neurons information transport mechanism

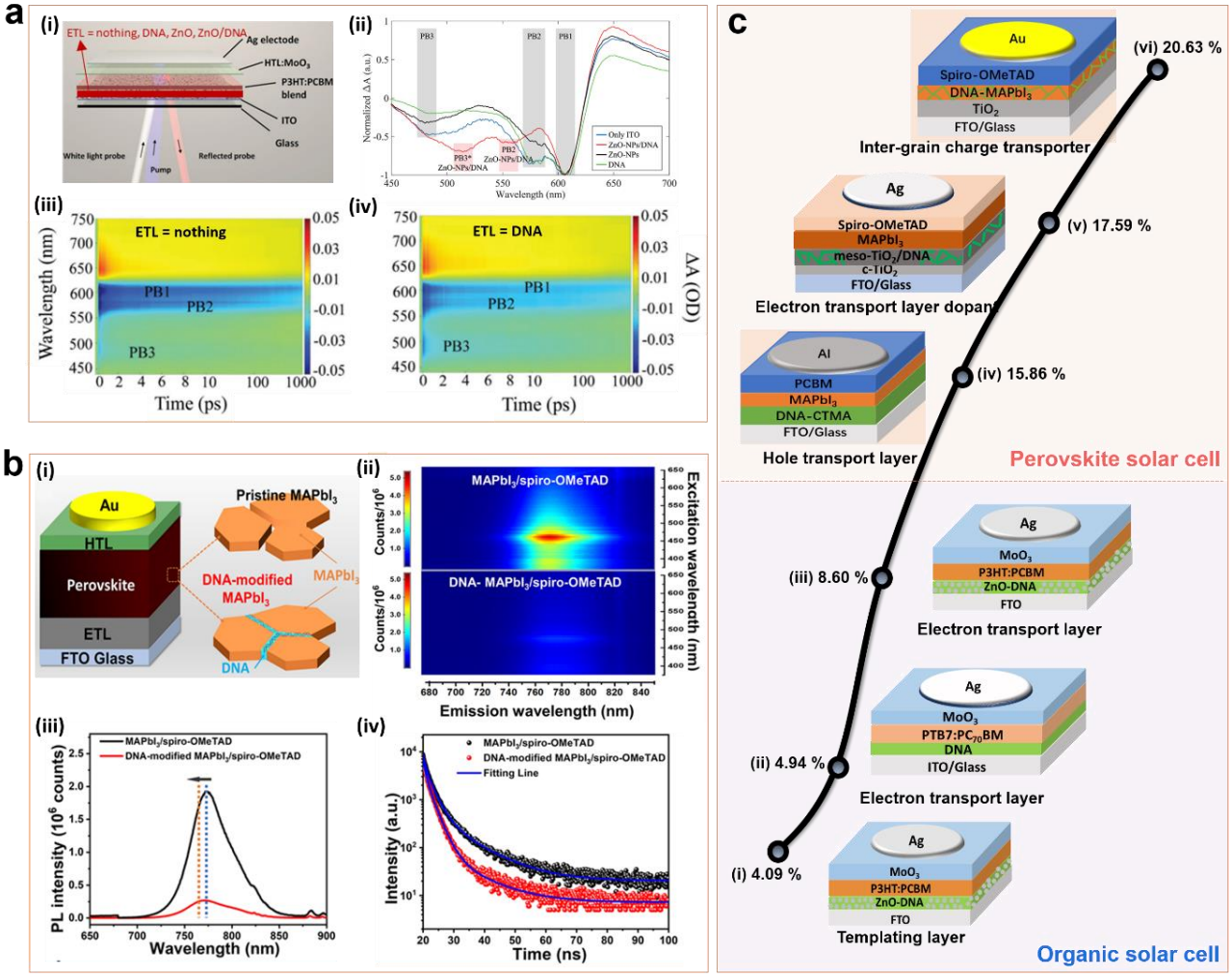

Figure 13 Employment of DNA in organic and perovskite photovoltaics. (a) (i) Schematic illustration of the organic solar cell using DNA as a CTL. (ii) Spectral cuts at a probe delay of 800 fs of the transient absorption of the DNA-incorporated solar cell. (iii) and (iv): Pseudocolor UV–vis transient absorption maps of solar cell device (iii) with and (iv) without DNA, adapted with permission from Ref.[273], Copyright 2018 WILEY-VCH Verlag GmbH & Co. KGaA, Weinheim. **(b)** (i) Schematic illustration of the DNA-integrated perovskite solar cell. (ii)-(iv): (ii) PL emission mapping, (iii) steady state PL spectra, (iv) time-resolved PL spectra of DNA-integrated $MAPbI_3$ and pristine $MAPbI_3$/hole-transport-layer structure, adapted with permission from Ref. [275], Copyright 2019 American Chemical Society. **(c)** Summary of different types of solar cells being incorporated with DNA: (i) Toschi et al. (Ref.[273]) (ii) Dagar et al. (Ref.[271]) (iii) Dagar et al. (Ref.[272]) (iv) Yusoff et al. (Ref.[274]) (v) Peng et al. (Ref.[276]) (vi) Hou et al. (Ref.[275]).

Fractals are prevalent in nature, in part because of their ability to generate a large surface area within a given volume.[262] The fractal leaf vein hierarchy structure, mentioned in the previous section (**3.2 Bottom Electrode**), can efficiently deliver water from petiole towards leaf blade. In a broader scale, such a natural fractal design of tree branches allows trees to absorb more sunlight, *bronchial trees* in animals to efficiently transfer oxygen to the bloodstream, and allows the coastlines to sufficiently disperse wave energy from the ocean.[263] The nervous system (comprising ~10^{11} neurons) in the human brain is another example of fractal geometry as well, with ~10^{14} synapses, or connections among these brain cells. This indicates an average of 10^3 connections for each cell through axons reaching out to make the synaptic connections with the dendrites of other neurons. As shown in **Figure 14a**, the nervous system is designed in a fractal branching pattern, connecting thousands of neuron's axons and dendrites that allows them to communicate with a large number of neighbouring cells. If the nervous system were designed using a *Euclidean geometry*, for example in cube-like shapes neatly packed into the brain, each neuron would only connect with at most six other cells, which wouldn't allow for the necessary synaptic communication. Overall, the fractal neurons exhibit advantages in delivering, processing and storing information in a more spatially efficient way, which aligns with the fractal geometry structural design. That is, by connecting structural patterns with each other over variable size scales, one can obtain large surface area and excellent transportability. Accordingly, fractal structural design can efficiently disperse or collect entropy (information), energy, and mass over large temporal and spatial dimensions. Therefore, artificial fractal structures inspired from natural designs (e.g., clouds, coastlines,[264] trees, neurons, bronchial trees, blood vessels[265]) have been widely researched for applied mathematics/physics

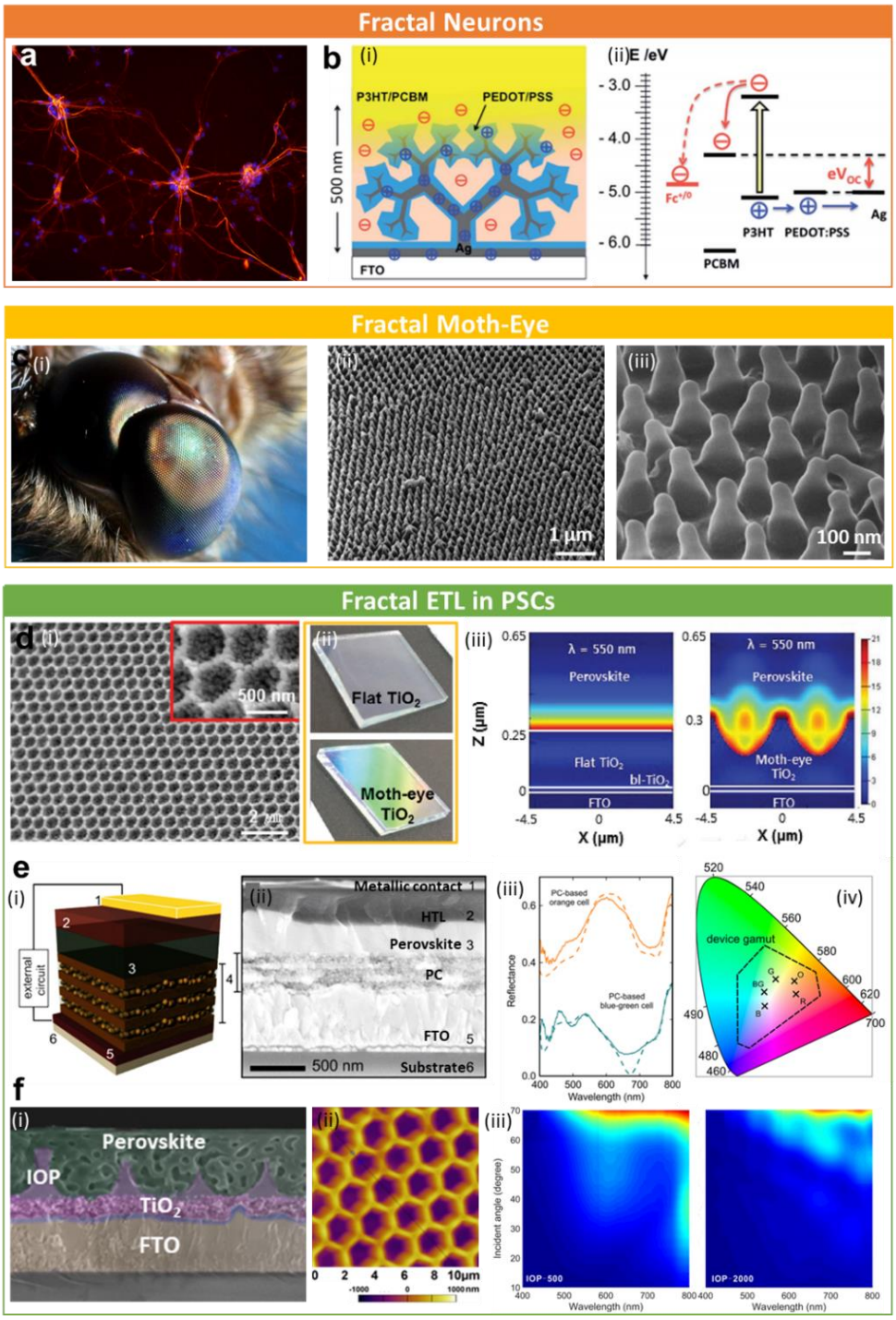

Figure 14 Fractal design. (a) Photograph shows the neuron network, adapted with permission from online resource.[303] **(b)** (i) Schematic illustration of an idealized morphology of fractal bulk heterojunction (BHJ) device. (ii) Energy level diagram in fractal BHJ device, adapted with permission from Ref.[285], Copyright 2014 The Royal Society of Chemistry. **(c)** (i) Photograph of moth eye, adapted with permission from online resource.[304] (ii) & (iii) SEM image showing the moth eye nanostructure, adapted with permission from Ref.[305], Copyright 2012 Springer Science and Business Media B.V. **(d)** (i) SEM image of moth-eye patterned mesoporous-TiO_2 layer (Moth-eye TiO_2). (ii) Photography of normal TiO_2 and moth-eye TiO_2 on glass substrates. (iii) Comparison of the spatial profile of the optical absorption per unit volume in the vertical direction of perovskite/flat TiO_2 and perovskite/Moth-eye TiO_2 at a wavelength 550 nm, adapted with permission from Ref.[294], Copyright 2016 Wiley-VCH Verlag GmbH & Co. KGaA, Weinheim. **(e)** (i) Schematic illustration of a photonic-crystal (PC)-based perovskite solar cell. (ii) Cross-sectional SEM image showing the structure of PC-based perovskite solar cell. (iii) Experimental (solid lines) and theoretical reflectance (dashed lines) of the PC-based orange (orange lines) and blue-green (dark cyan lines) perovskite solar cells. (iv) CIE 1931 chromaticity space showing the color hues of the PC-based (R) red, (O) orange, (G) green, (BG) blue-green, and (B) blue cells, adapted with permission from Ref.[299], Copyright 2015 American Chemical Society. **(f)** (i) Cross-sectional SEM image showing the structure of solar cell device based on 2D 'inverse-opal' perovskite (IOP) photonic films. (ii) AFM topographical image of IOP photonic film. (iii) The variable-angle reflection spectra of IOP films with different micro-geometry, adapted with permission from Ref.[300], Copyright 2016 American Chemical Society.

(e.g., antennas[266]) and could have great significance when

applying it in designing optimized electrodes for solar cells.

4.2.2 Fractal vs. Euclidean design in solar cell

The fractal neuron concept is predicted to enhance the charge transport efficiency for solar cells. For example, a branched network is responsible for more efficient light manipulation through sublayer scattering. Meanwhile, interfacial charge transfer at a heterojunction with a proper fractal design could further assist the dissociation of excitonic state into free charges, which aligns with the "bulkheterojunction (BHJ)" idea in OPVs.[267] The structured electrodes are also able to collect the photogenerated charge carriers in a more efficient way. For example, Kay et al.[268] constructed the Fe_2O_3 electrodes displaying improved transport properties due to a fractal ('*cauliflower*') structure. Meier et al.[269] developed a micro-structured PEDOT:PSS HTL on Al electrode which enhanced the charge flow and improved PCE for the solar cell. Recently, Chamousis et al.[270] also use the fractal electrodes to promote charge separation and extraction from illuminated photoactive layer. **Figure 14b(i)** shows the fractal silver layer with a dendritic topography, coated by a thin PEDOT:PSS HTL used as the photoelectrode. The fractal silver layer on the fluorine-doped tin oxide (FTO) substrate was prepared via electrochemical deposition of silver sulfate (Ag_2SO_4) under diffusion-limited conditions.[271–275] Such a spatial stretching structure benefits the charge flow from the photoactive layer towards the photoelectrode, as illustrated in the energy level diagram in **Figure 14b(ii)**.

4.2.3 Fractal structure for light manipulation

Fractal structures inspired and/or mimicked from examples in nature have been employed in designing high-performance functional structures for various applications.[276–278] In solar cell research, these fractal structure designs have been made to manipulate the light for (i) optical reinforcement for higher photocurrent through multiple effects (e.g., anti-reflection effect) and/or (ii) specific coloration for devices through introduction of 'artificially colored' meta-structures. Light manipulation using the anti-reflective function of the structures has been a highlighted part of their applications. For solar cells, optical loss by light reflection at surfaces is responsible for 14% of total losses. Thus, it is critical to reduce the reflection losses to improve PCE. Optical reflection occurs at an interface between two media having different optical refractive indices and can be explained by the *Fresnel's Equations*.[279–281] When light passes through two media of refractive indices of n_1 and n_2, respectively, the reflection (R) at the interface can be predicted by the equation of $R = [(n_2 - n_1)/(n_2 + n_1)]^2$. A smaller difference in refractive indices between the two media will result in less reflection. For 3D structures having subwavelength periods or lengths, the effective refractive index of the system is determined by the volume fraction.[282] The eyes of certain species of moths, butterflies, and flies have such a fractal microscopic design, with arrays of *protuberances* which have dimensions smaller than the wavelength of the incident light upon them. **Figure 14c(i)** shows a picture of a moth's eye (*Cephonodes hylas*) with a microscopic view showing the arrays of *protuberances* (**Figures 14c(ii)** and **14c(iii)**). Such a feature forms a region with a graded refractive index at an interface (between two media), which can substantially reduce the amount of light that is reflected by the interface. As a result, the reflectance reduction is thought to increase the sensitivity of the visual system of the species. This fractal microstructure also leads to the transparent sections of an insect's wing, giving them a camouflaging effect. On the basis of this fractal moth-eye anti-reflection strategy, improvement in transparency at the front contact of solar cells has been attempted.

One example in PSC is the structural modification of the TiO_2 ETL in a *n-i-p* device architecture.[283] Kang et al.[279] reported utilizing the nanopatterned mp-TiO_2 layers with a conical shaped 'moth-eye' structure (of a 500-nm-dorm feature) for improving the light harvesting efficiency (LHE). This bio-inspired fractal nanostructure can reduce the reflection at the interface between mp-TiO_2 ETL and $MAPbI_3$ photoactive layer as the fractal pattern induced optical manipulation which resulted in an antireflective property. Using soft nanoimprinting lithography and polydimethylsiloxane (PDMS) stamping methods, a moth-eye patterned mp-TiO_2 layer was successfully obtained, showing a well-ordered periodic 2D hexagonal symmetry (**Figure 14d(i)**). The optical enhancement from the moth-eye patterned mp-TiO_2 layer was also observed from the photograph of a real film, as can be seen from the colorful surface (light scattered) of the patterned mp-TiO_2 film in **Figure 14d(ii)**. In addition, finite-difference time-domain (FDTD) method also predicts the optimized optical field distribution in those fractally patterned mp-TiO_2 film (**Figure 14d(iii)**). As a result, in comparison with the flat layer, PSCs incorporating the moth-eye TiO_2 exhibits a 5.3% enhancement of photocurrent and improves the PCE from 15.74% to 17.48%.

The fractal structure in the eye or wings of insects also leads to the strong coloration. Such a structural color, in contrast to dyes or pigments, originates from the interference of ordered coherently scattering of light waves, which provides the coloration for species. For example, the fractal structure, and the resultant color, in wings of butterflies is important for camouflage, mating, and warning. Similarly, from the art perspective for the MPS products, PVs with aesthetical versatility, appealing appearance and colorfully vivid feature are becoming more and more important in modern life. Beyond the basic power supplier function, multiple products such as building integrated PV and PV built-in clothing also must consider the aesthetics of the end product. In regards to this, Zhang et al.[284] developed a multilayered scaffold that can provide optical reflection at certain visible wavelength and provide the PSC device with structural colors. **Figure 14e(i)&(ii)** show the device architecture incorporating porous photonic crystal (PC) based scaffold with dual functionalities of optical reflection and charge transport. By precisely tuning the reflectance peak of the PC and the absorption from the infiltrated perovskite, vivid iridescences with variable colors ranging across the visible spectrum can be obtained. For example, **Figure 14e(iii)** shows the reflectance spectra of an orange (orange lines) and blue-green (dark cyan lines) PSC using the PC scaffold. Further tuning the PC and

perovskite nanostructures, colors ranging from red (0.41, 0.34) to orange (0.41, 0.40), green (0.33, 0.41), blue-green (0.29, 0.35), and blue (0.29, 0.30) in the chromaticity space have been obtained for the PSC devices (**Figure 14e(iv)**). These PSCs with a wide range of iridescence also exhibit efficient performance with PCEs up to 8.8% with a blue hue. The use of natural fractal inspired structural colors, rather than utilizing pigments or dyes, as meta-optical materials provides a promising outlook for development of PSCs and their MPS products.

Meng et al.[285] also reported vivid colored PSCs using the 2D 'inverse-opal' perovskite (IOP) photonic films. Typically, the inverse-opal (IO) structured films (film replicas containing colloidal crystals (artificial opals)) are composed of patterns with ordered void arrays surrounded by solid materials in continuous alternations of high and low refractive index.[286] Such a structure affects the light wave propagation and alters the optical property of the film.[287] The 2D IOP film can be fabricated via a template-assisted spin-coating processing. **Figure 14f(i)&(ii)** shows the microscopic structure. Additionally, the IOP film makes it possible for the angular dependency of color variation, which originated from optical reflection of the nanostructures (**Figure 14f(iii)**). This feature can allow PSCs to be utilized for various applications that require aesthetic functions. Briefly, specifically tuning the IOP micro-geometry and the optical property of the perovskite (through changing the material composition at the crystallographic A, B and X-sites of the ABX_3 halide perovskite), colorful devices with respectable PCEs (6.7% to 11.2%) have been obtained.

4.3 Bacteriorhodopsin (bR)

4.3.1 Natural role of bR

Bacteriorhodopsin (bR) protein extracted from *Halobacterium salinarum* has been broadly utilized in multiple biohybrid

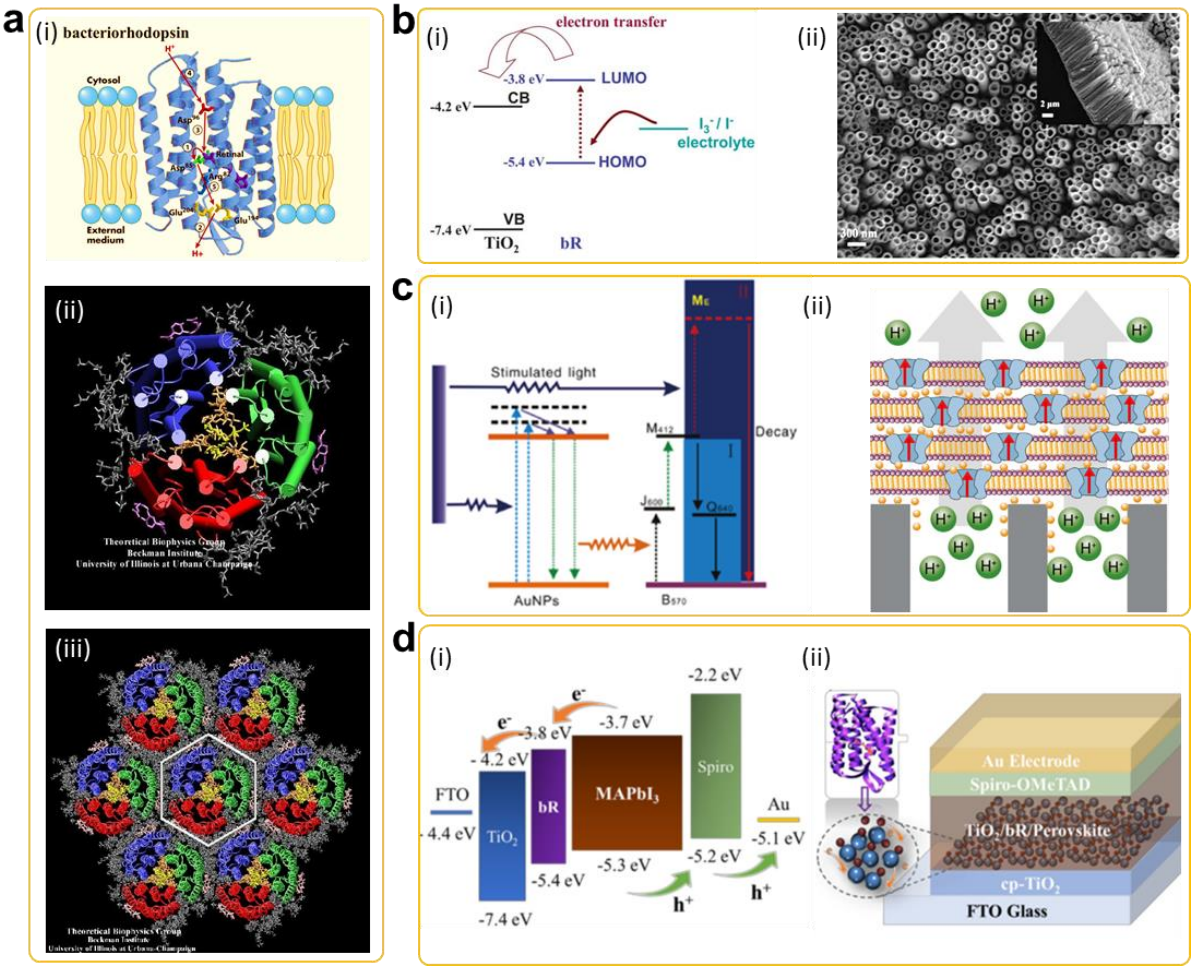

Figure 15 Bacteriorhodopsin (bR) related CTL application in PV. (a) (i) Schematic illustration of the bacteriorhodopsin (bR) in archaea *Halobacterium salinarum*, adapted with permission from online resource.[332] (ii) Unit cell structure and (iii) top view of multiple unit cells of the purple membrane (PM) containing bR trimer and lipid molecules, adapted with permission from online resources.[333,334] **(b)** (i) Energy level diagram of charge carrier injection in the bR/TiO_2 photoanode cell. (ii) SEM image of the TiO_2 nanotube arrays with the inset showing the cross-sectional view, adapted with permission from Ref.[307], Copyright 2011 The Royal Society of Chemistry. **(c)** (i) The equivalent energy level diagram of the photochemical reaction in a bR-integrated photovoltaic stacking system. (ii) Schematic illustration showing the structure of the bR/AuNPs heterogeneous multilayers, adapted with permission from Ref.[314], Copyright 2015 Elsevier. **(d)** (i) Energy level diagram of bR-integrated perovskite solar cell (BPSC). (ii) Schematic illustration of the architecture of BPSC, adapted with permission from Ref.[322], Copyright 2019 American Chemical Society.

electronics known as "bioelectronics" that merges current electronic techniques with biology.[288] The bR (playing a role of a light-driven proton pump in the purple membrane (PM) of the archaea *Halobacterium salinarum*) consists of seven-transmembrane (7TM) helices and a retinal chromophore covalently bound in the central region through a protonated Schiff base to a lysine residue (**Figure 15a(i)**). The PM (**Figures 15a(ii)** and **15a(iii)**) is composed of a 2D hexagonal crystal with a ~6.2 nm unit cell (containing bR trimer and lipid molecules as intertrimer medium). The photocycle in bR can be initiated by the photon absorption at the covalently bound chromophore retinal which leads to a series of conformational changes within the protein, and ultimately to the proton transport across the cell membrane. Such a photon-activated mechanism, along with the ability of bR to regenerate, makes it possible to develop bR-based nano-optoelectronics.[289] For example, aligned bR PM film on ITO has shown an efficient and stable photocurrent response.[290] Early attempts of utilization of bR as a light-activated component in PV cells exhibited 9.73 mV cm^{-2} and 41.7 mV cm^{-2} in dry and aqueous systems, respectively.[291] Although there have been many successful cases of bR-based biohybrid electronics (which have been well reviewed elsewhere[288]), practical utilization of these biomolecular-based components in electronics require a detailed understanding of the coupling of these individual bR molecules to macroscopic surfaces of electrodes, as well as the evolutions in electronic environment under dynamic (nonequilibrium) conditions.[292] Prior research has revealed that bR can be fully functional under a wide range of temperatures and pH, while the conductivity of bR could be separated into two regimes, determined by various charge transport mechanisms.[293–295] At lower temperatures (T< 250 K), the electrical conductance is dominated by the electron tunneling mechanism which switches to the electron hopping mechanism as temperature increases.[293] The electron hopping mechanism will be affected by the removal of the retinal chromophore within the bR. The interaction intensity between the bR protein and the electrode substrate can also affect the transport mechanism.[294]

4.3.2 Applied role of bR

As the bR is responsible for a series of photochemical reactions ultimately leading to the protons pumping across the membrane, PV can utilize each individual reaction to promote either efficient photon absorption or charge transport. Hence, different operation mechanisms in regards to bR being applied in PVs have been reported. **Table 4** summarizes works using bR to promote charge transport in related optoelectronics. For example, Allam et al.[289] report on the assembly and utilization of a bR/TiO_2 nanotube array as the photoelectrode in photoelectrochemical application. The ~7 μm thick nanotube array of TiO_2 films were fabricated by room-temperature anodization of Ti-foil in the formamide electrolytes containing NH_4F, followed by the sensitization with bR. Such a nanotube array of TiO_2 enables sufficient attachment of bR at the surface (**Figure 15b(ii)**). By using the bR/TiO_2 hybrid photoelectrodes for photoelectrochemical water splitting, the hybrid electrodes obtained an increased photocurrent density

Table 4 Summary of operational mechanism of previous bR-based photovoltaics.

Composite Materials	Operational mechanisms	Ref.
bR/TiO_2	Electron transfer effect	[290]
bR/Au	Coupled proton transportation	[297]
bR/kpw	3D proton transfer	[315]
bR/AAO	Protons transportation	[316]
bR/Nafion	Plasmonic enhancement	[317]
bR/QDs	Förster resonance energy transfer	[318]
bR/CNTs	Electron-ion interaction	[319]

of 0.65 mA cm^{-2} (under AM 1.5 illumination), about 50% improvement compared to the pure TiO_2 nanotubes (0.43 mA cm^{-2}) fabricated under the same conditions. The improvement is due to the bR-assisted efficient electron transfer from electrolyte to the photoanode of TiO_2. **Figure 15b(i)** shows the energy level diagram and a mechanism of electron injection to the bR/TiO_2 photoanode in presence of redox I_3^-/I^- electrolyte solution. The bR has a LUMO and a HOMO energy level of -3.8 and -5.4 eV (based on surface photovoltage spectroscopy (SPS[290])), respectively. TiO_2 has a conduction band maximum (CBM) of -4.2 eV, which allows an efficient electron injection from bR to TiO_2 (**Figure 15b(i)**). In the presence of the redox electrolyte (0.02M I_3^-/I^-), an electron can be captured by bR and excited from HOMO to LUMO upon illumination, which is then expected to travel to the TiO_2 photoanode. Guo et al.[296] also proposed a bR/metal heterogeneous structure for efficient charge transfer, which also leads to a novel PV stack system. On the optical side, using delicate, well-patterned structures to maximize the light absorption is one of the most widely used strategies in nature. For example, in the leaf cell, as the core organ for photosynthesis, *Granum*[297] consists of a stack of 10–100 *thylakoids* containing pigments and electron-acceptors. When the light stimulates the antenna pigment in the *thylakoids*, electrons can be excited and transferred via the photoelectric conversion process. The stacking design of *thylakoids* provides a large surface area which allows for highly efficient solar radiation capture. It has been reported that by mimicking this stacking design through constructing TiO_2 nanosheets templated by graphene, photoelectric response can be enhanced ~20 times.[298] The bR and its surrounding purple membrane also have a 2D crystalline feature (**Figure 15a(iii)**), making it possible to stack with metal to form a laminar electrode capable of more efficient radiation capture. This has been achieved by constructing bR/Au NPs heterogeneous multilayers for a photovoltaic stacking system (**Figure 15c(ii)**), where the bR layers are inserted between AuNPs layers. The bR layers work as the photon acceptor and the Au NPs layers can further enhance the photocurrent because of its native surface plasmon field effect. **Figure 15c(i)** illustrates the equivalent energy level diagram of the photochemical reaction in these stacks. When a continuous incident light (350–800 nm) is shed on the device, the

excited state can be pumped by AuNPs leading to emitted light of ~ 520 nm. The 520 nm light is then absorbed by bR, giving rise to a photocycle starting from the B570-state to the J600-state, and then passes to the M412-state in bR. It should be noted that the blue light is also contained in the stimulated light source, which can directly affect the bR's ability to accelerate the decay of the immediately formed M412-state in bR.[299] This provides a shorter time pathway II (light activates the M412 to an excited state Me,[300] which can facilitate a quicker decay to B state) to complete the typical photocycle, leading to a 'bypass photocycle model' in bR. With the stacking of Au NP layers, the photocycle pathway of partial bR molecule will take this ('bypass' short-cut) pathway II, which represents as a more efficient and accelerated photocycle for bR. For PV application, bR has been employed as photosensitizers in bio-sensitized solar cells (BSSCs), where the bR proteins are attached on TiO_2 film. These proteins can be photo-excited and transfer the excited states to the TiO_2 photoanode, as well as refill the electrons from the redox reaction with the electrolyte. Thavasi et al.[301] built the first BSSC using bR as a light harvester, being adsorbed at the TiO_2 electrode, exhibiting a V_{OC} of 0.35 V and J_{SC} of 0.09 mA cm^{-2} under an illumination of 40 mW cm^{-2}. Following this, Mohammadpour et al.[302] and Jeganathan et al.[303] fabricated BSSC based on TiO_2/bR electrode and the devices displayed a PCE of 0.35% and 0.49% under AM 1.5, respectively. More recently, Das et al.[304] reported bR assisted photocycle in PSCs. The bR can be inserted between the TiO_2 ETL and perovskite photoactive layer, which implements the energy transfer step involving photon absorption and Förster resonance energy transfer (FRET) process. **Figure 15d** contains the energy level diagram (**Figure 15d(i)**) and the schematic illustration of the corresponding PSC device (**Figure 15d(ii)**). The light energy conversion can be achieved through the transfer of the photogenerated electrons from the perovskite to bR molecules through a FRET process.[305–307] The photogenerated electrons can be subsequently transferred to TiO_2 ETL, driven by the energy level difference between bR and TiO_2.[308,309] Such a bR bridge between perovskite and TiO_2 is further verified by the observation of reduced interfacial charge recombination. As a result, the bR modified PSC exhibits a higher PCE of 17.02% compared to that of 14.59% from a reference blank device.

Overall, the bR photocycle effect on photocurrent enhancement provides an additional mechanism for tuning the interface between the photoactive layer and the photoelectrode. Considering the control role of proton 'gate' (bR's original role in creatures, as shown in **Figure 15a**) and the photocycle process of bR, there could be two ways to export the optical signals of bR. One is to design and construct a photocell system jointed by two half-cells, which can produce the proton gradient difference between the two half-cells, i.e., a proton 'gate'. The other one is to couple the proton with electronic carriers, inducing the displacement and recombination of the charged carriers during the bR photocycle, resulting in the generation of a differential photovoltage. The ongoing research using bR incorporated hybrid structures for enhancing photocurrent or frequency response, is expected to be applied in fields of biological electronics with potential applications in medical electronics such as bR-based immunosensor[310] and bR-based artificial retinal prostheses.[311] Nevertheless, in solar cells, bR incorporation taking advantages of its 'gate' and photocycle role in complex with perovskite crystals still remains an untapped research area, with the energy/mass transfer mechanism at the bR/perovskite interface being a particularly interesting research topic. In fact, many other dyes besides bR have shown unusual energy transfer mechanisms, which has led to several interesting subtopics such as Triplet-triplet annihilation (TTA) upconversion[312] and singlet fission (SF)[313] that can bring new insights for reducing the thermodynamic losses in PSC and hypothetical foundations for exceeding the Shockley–Queisser (SQ) limit of solar cells.

4.4 Other natural materials

Natural materials including biological molecules with conjugated structure or radical features can be good charge transport materials for electronic applications. Particularly, for the π-conjugated natural pigments such as Chlorins (a specific type of porphyrins which is in a form of Mg^{2+} complexes found as the green photosynthetic pigments in plants (*chlorophylls*)), the energies of frontier molecular orbitals (*i.e.*, HOMO and LUMO) and the distribution of the orbitals (*i.e.*, DOS) in these molecules play crucial roles in intra- and inter-molecular charge transport, and are also relevant to the light absorption/emission, charge injection/extraction/trapping and electron pushing/pulling or donating/accepting effects. These π-conjugated features in those artificially synthesized semiconducting polymers/small organic molecules enable their optoelectronic properties and make them widely applied in fields such as OPVs and OLEDs. Natural pigments also have such conjugated structure, which makes them good candidates for CTL materials in PSCs.

4.4.1 Porphyrins

Porphyrins, derived from Greek word '*porphyros*' meaning 'purple', are compounds of cyclic, tetrapyrrolics with intense colors. In nature, porphyrins are the parent members of pigments in various species and serve key roles in various vital processes such as metabolisms and photosynthesis. For example, the *heme* has a porphyrin ring (**Figure 16a**), the iron center (Fe^{2+}) in the porphyrin ring can coordinate the oxygen (O_2) serving as the oxygen carrier. Hence the blood cell containing *heme* can carry oxygen from the lungs to the various tissues. In fact, 70% of the body's iron is present in red blood as hemoglobin, composed of iron-porphyrin *heme* groups, resulting in the red color of human blood (color of Fe^{2+}, this is different from the blue color in spiders and octopuses' blood which contains Cu^{2+}). *Hemes* are also crucial in enzymes (*e.g.*, liver enzymes metabolizing drugs), catalases (protecting cell from oxidative damage), or electron transfer proteins.[314] Another example of a natural porphyrin complex is found in chloroplasts of algae and plants, *i.e.*, the *chlorophyll*, a green pigment critical in photon absorption, resonance energy transfer and photoexcited charge separation in

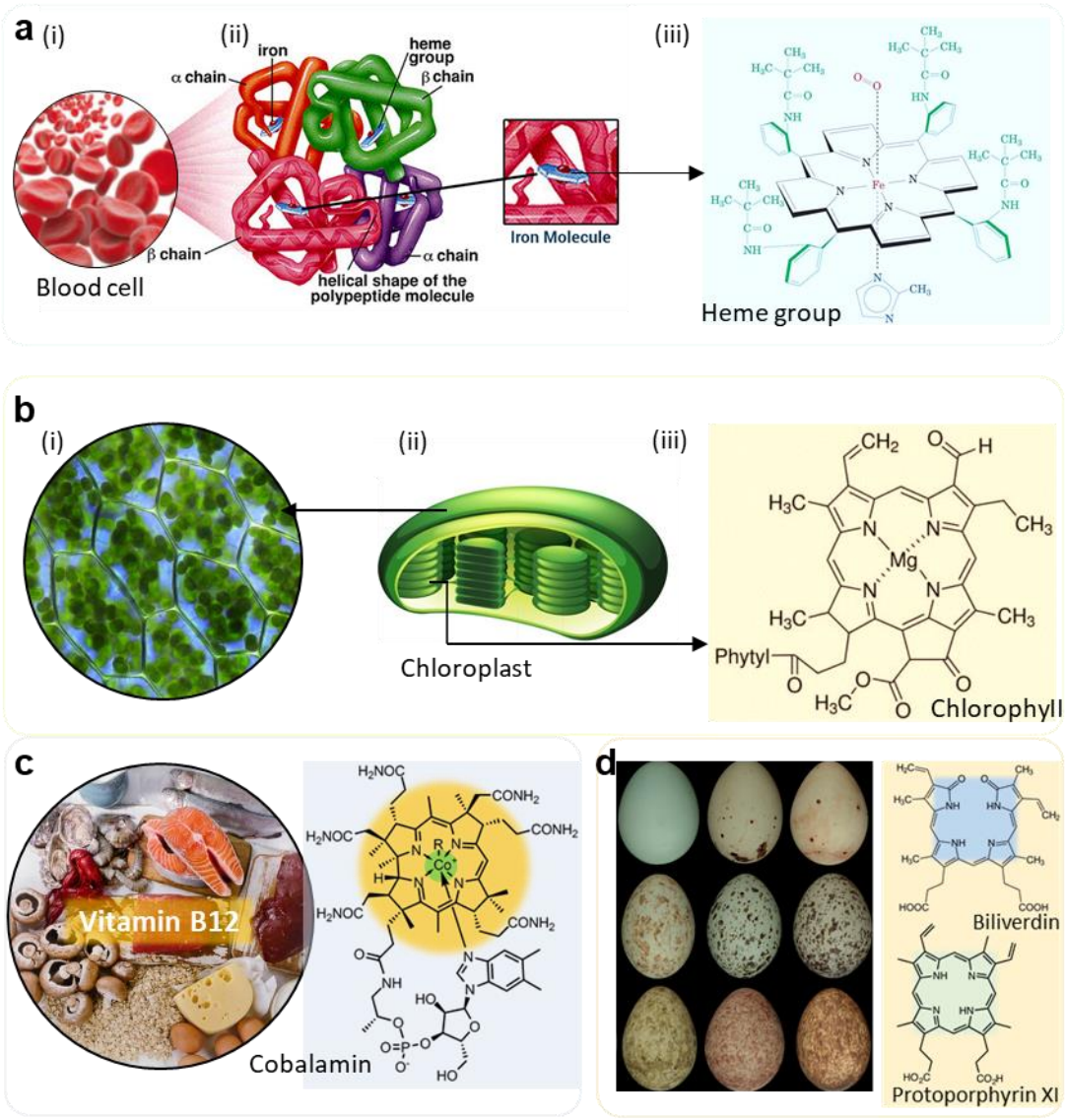

Figure 16 Porphyrins and derivatives. (a) Schematic illustration of a (i) blood cell, (ii) molecular structure of Hemoglobin and (iii) chemical structure of *heme group*. Adapted with permission from online resources.[342,343] **(b)** (i) Microscopic image of *Plagiomnium affine laminazellen* showing the (ii) Chlorophyll in the cell, schematic illustration of chloroplast structure, and (iii) chemical structure of *chlorophyll*. Adapted with permission from online resource.[344] **(c)** Images of foods in rich of Vitamin B12 (left) and chemical structure of *Cobalamin* (right), adapted with permission from online resource.[345] **(d)** Image of eggshells of different avian lineages showing varying color and pigment patterns (left), and chemical structure of *Biliverdin* and *Protoporphyrin XI* (right), adapted with permission from Ref.[346], Copyright 2016 Wiley-VCH Verlag GmbH & Co. KGaA, Weinheim.

photosynthesis. *Chlorophyll* molecules are embedded in the thylakoid membranes of chloroplasts in photosystems (**Figure 16b**), and are well arranged so that light harvesting and transportation (>95% transfer efficiency) could maximize the efficiency in such a small system. The high energy transfer efficiency is realized by the unique property of *chlorophyll* (incorporated with Mg^{2+} in the porphyrin ring) that the absorption and emission spectra overlap exceptionally well, so the energy transfer to nearby molecules can favorably follow the Förster (resonance) mechanism. Following this, the photon energy can be harvested by *chlorophyll* and then transferred among ~100 *chlorophyll* molecules through this resonance mechanism. As a result, the overall energy transfer process, from photon absorption to arrival at the reaction center is less than 10 ps, which is significantly faster than the *chlorophyll* fluorescence lifetime of 5 ns (in this way the fluorescence loss is negligible). Replacing Mg^{2+} with other metals will not only change the absorption and emission spectra, inducing less efficient resonance energy transfer, but also competitively quench the *chlorophyll's* excited state (through a spin-orbit coupling or 'heavy atom effect') and reform the ground state. Therefore, the Mg^{2+} *chlorophyll* is designed by nature to maximize the efficiency of photosynthesis. Additionally, other porphyrin-derived natural pigments are found in *cobalamin* (Vitamin B12 source as shown in **Figure 16c**, which is typically involved in the metabolism of every cell in human body, affecting DNA

Table 5 Summary of electronic properties and photovoltaic performance of porphyrin-based HTL in perovskite solar cells.

Porphyrin	Work Function (eV)	Hole Mobility ($cm^2/V{\cdot}s$)	Perovskite Composition	Device Architecture	PCE (%)	Ref.
Y2[b]	-5.25	2.04×10^{-4}	$MAPbI_3$	FTO/c-TiO_2/m-TiO_2/PVK/Por/Au	16.6	323
Y2A2[b]	-5.1	1.53×10^{-5}			10.55	
WT3[b]	-5.2	4.2×10^{-4}	$Cs_{0.05}[(FA_{0.83}MA_{0.17})PbI_{0.83}B_{r0.17}]_{0.95}$	FTO/c-TiO_2/m-TiO_2/PVK/Por/Au	19.44	325
YR3[b]	-5.1	9.3×10^{-5}			17.84	
Y2[b]	-5.22	3.2×10^{-5}			17.93	
Zn-22[b]	-5.29	2.89×10^{-4}	$(FAPbI_3)_{0.85}(MAPbBr_3)_{0.15}$	FTO/c-TiO_2/m-TiO_2/PVK/Por/Au	17.78	324
Cu-22[b]	-5.37	3.06×10^{-4}			15.36	
PZn-TPA-O[b]	-5.31	3.51×10^{-4}	$MAPbI_3$	ITO/ZnO/PVK/Por./Au	12.4	330
PZn-TPA[b]	-5.2	3.38×10^{-5}			11.96	
PZn-DPPA-O[b]	-5.23	3.85×10^{-5}			13.52	
PZn-DPPA[b]	-5.36	4.1×10^{-4}			14.11	
PZn-TPA[b]	-5.2	3.3×10^{-5}	$MAPbI_3$	ITO/ZnO-s/PVK/Por./Au	16.37	331
PZn-2FTPA[b]	-5.4	3.9×10^{-5}			18.85	
PZn-3FTPA[b]	-5.29	3.5×10^{-5}			17.71	
Zn-Py	-5.35	N.A.	$MAPbI_3$	FTO/c-TiO_2/m-TiO_2/PVK/Por/Au	17.82	336
Co(II)-23/Co(III)-23	-5.3	N.A.	$Cs_x(MA_{0.17}FA_{0.83})_{(1-x)}Pb(I_{0.83}Br_{0.17})_3$	FTO/c-TiO_2/m-TiO_2-SM/PVK/Por/Au	20.02	332
DPPEZnP-TSEH	-5.2	2.60×10^{-5}	$MAPbI_3$	ITO/SnO_2/C_{60}/PVK/BHJ (Por.+PCBM)/MoO_3/Ag	19.02	337

([a]Abbreviations: BHJ = bulk heterojunction; c-TiO_2: compact TiO_2; m-TiO_2: mesoporous TiO_2; m-TiO_2-SM: mesoporous TiO_2 modified with sinapoyal malate; ZnO-s: sulfur-passivated ZnO; PVK: Perovskite; Por.: Porphyrin; [b]LiTFSI and 4-tertbutylpyridine additives were incorporated into the precursor solution for the preparation of hole transport layer.)

synthesis and regulation as well as fatty acid and amino acid metabolism), *biliverdin* and *protoporphyrin* (**Figure 16d**, found in thin regions of eggshells and proposed to strengthen the egg shell[315]). Overall, the porphyrins-based materials with relatively high chemical stability have shown an enormous application range, including chemical usage (oxidation, atom transfer, and electron transfer catalysts), advanced functional devices (CO_2 reduction, light harvesting, information storage, and chemosensors), medical applications (photochemotherapeutics for cancer treatment), and imaging techniques as well (used as fluorescent/photoacoustic imaging dyes in the biomedical fields).

Considering their low oxidation potential and high charge transporting capabilities, porphyrins are considered to be efficient CTLs in PVs. Because of the large structural tuning capacity, porphyrins materials could have high versatility in terms of electrochemical, photophysical and charge-transport properties, making them good CTL candidates to perovskite materials of highly tunable energy levels. In addition, porphyrins have excellent thermal stability and high hole mobility due to the strong π-π stacking and intermolecular charge transfer of the porphyrin film (in fact the porphyrin materials have been applied as an electron donor in BHJ OPVs[316]). These jointly secure their initial success in PSCs. **Table 5** summarizes prior examples of using porphyrins materials as HTLs in PSCs. In 2016, Chou et al.[317] reported the first porphyrin based HTL (Zinc porphyrins: Y2 and Y2A2) for PSCs. As shown in **Figure 17a**, Y2 and Y2A2 consists of a *meso*-5,15-bis(ethynylaniline)porphyrin backbone bearing the butyl (Y2) or dodecyl chains (Y2A2), with two facing alkoxyphenyl groups in the other two opposite *meso* positions. The design benefits the electronic communication between the porphyrin core and the donor amine group. As a result, the Y2 and Y2A2 films exhibit well-matched HOMO of −5.22 eV (close to the CBM of -5.4 eV of $MAPbI_3$) and high hole mobility of 10^{-4} cm^2 V^{-1} s^{-1}, resulting in a PCE of 16.60% (comparable to that of 18.03% from a reference cell using Spiro-OMeTAD). Chen et al.[318] reported the 5,10,15,20-tetrakis{4-[N,N-di(4-methoxylphenyl)amino-phenyl]}-porphyrin with Zn(II) and Cu(II) being centered in the porphyrin ring (abbreviated by 'ZnP' and 'CuP' in **Figure 17b**). Density functional theory (DFT) results show that the four meso-substituted triarylamines surrounding the porphyrin ring are nearly perpendicular to the porphyrin due to steric hindrance, giving a twisted spatial structure. Both the porphyrin core and the triarylamine contribute to the HOMO DOS distribution of ZnP and CuP, while the LUMO is only determined by the porphyrin ring. Compared to ZnP (-5.29 eV), CuP has a lower HOMO of -5.37 eV. The corresponding film exhibits similar hole mobility of about 3×10^{-4} cm^2 V^{-1} s^{-1}, nearly two-fold higher than Spiro-OMeTAD (1.58×10^{-4} cm^2 V^{-1} s^{-1}). ZnP based PSC exhibits a PCE of 17.78% compared to the Spiro-OMeTAD reference (18.59%). For the HTL application in solar cells, the morphological features of the film, such as pin-hole, uniformity, surface roughness, and porous density, as well as their effects on mobility, electrical conductivity and slight energy-level shifting, are crucial to final device performance. Re-engineering the molecular structure of porphyrin to optimize the intermolecular

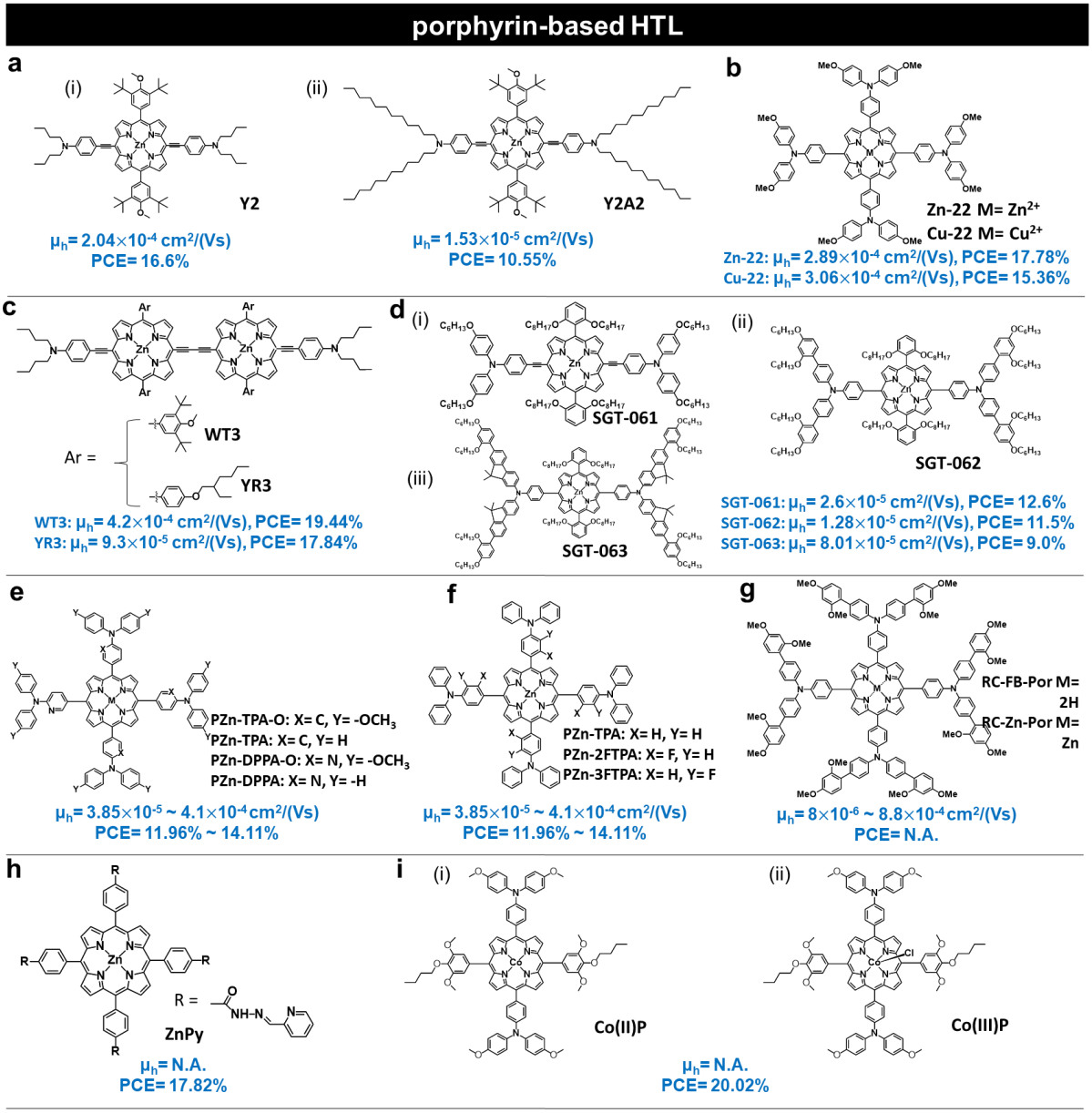

Figure 17 Chemical structure of some reported porphyrin-based hole transport materials. (a) (i) Y2 and (ii) Y2A2, adapted with permission from Ref.[348], Copyright 2016 American Chemical Society. **(b)** ZnP and CuP, adapted with permission from Ref.[349], Copyright 2017 American Chemical Society. **(c)** WT3 and YR3, adapted with permission from Ref.[350], Copyright 2018 American Chemical Society. **(d)** (i) SGT-061, (ii) SGT-062 and (iii) SGT-063, adapted with permission from Ref.[354], Copyright 2019 Elsevier. **(e)** PZn-TPA-O, PZn-TPA, PZn-DPPA-O and PZn-DPPA, adapted with permission from Ref.[355], Copyright 2017 Wiley-VCH Verlag GmbH & Co. KGaA, Weinheim. **(f)** PZn-TPA, PZn-2FTPA and PZn-3FTPA, adapted with permission from Ref.[356], Copyright 2018 American Chemical Society. **(g)** RC-FB-Por and RC-Zn-Por, adapted with permission from Ref.[367], Copyright 2018 Wiley-VCH Verlag GmbH & Co. KGaA, Weinheim. **(h)** ZnPy, adapted with permission from Ref.[366], Copyright 2019 Elsevier. (i) Co(II)P and (ii) Co(III)P, adapted with permission from Ref.[357], Copyright 2018 Wiley-VCH Verlag GmbH & Co. KGaA, Weinheim.

interaction and their stacking in the final film can be a shortcut. Chiang et al.[319] extended the coplanarity of porphyrin by using the dimeric porphyrin conjugates structure.[320–322] The resultant porphyrin dimers WT3 and YR3 were composed of ethynylaniline electron-donating moieties attached at the lateral meso-positions of the porphyrin (**Figure 17c**). The enhanced coplanarity enables a better intermolecular interaction and a higher PCE of 19.44% from the WT3 based device (compared to that of 18.62% from the Spiro-OMeTAD reference device). Kang et al.[323] employed three different substituted electron-donating triarylamine (TAA) groups to extend the π-conjugation of the molecule (coded as SGT-061, SGT-062, and SGT-063 with structures being shown in **Figure 17d**). These molecules consist of a coplanar porphyrin core and different TAA bulky donor groups which possess a larger dihedral angle between the alkoxy-substituted phenyl ring and the donor TAA. This spatial effect gives rise to a strong interference for the dense molecular arrangement and a modulation on the π-π intermolecular stacking. Consequently, the SGT-061 with a less bulky donor group and a tighter molecular stacking exhibits a higher hole mobility of 2.60 × 10^{-5} cm^2 V^{-1} s^{-1} than that of SGT-062 (1.28 × 10^{-5} cm^2 V^{-1} s^{-1}) and SGT-063 (8.01 × 10^{-6} cm^2 V^{-1} s^{-1}). Although the device

exhibits relatively lower PCE of 9.0-12.6% (compared to the 16.6% from Spiro-OMeTAD-based reference cell) due to the low hole mobility, the rule of "the less bulky, the easier molecular stacking" is verified in practice. Overall the molecular stacking of the porphyrin materials plays the most important role in their HTL films for PSCs. Besides the modulation on such a coplanarity, the intermolecular stacking and the consequent film morphologies can also be influenced by the functional moieties surrounding the core porphyrin ring. For example, Lee et al.[324] designed a series of novel zinc porphyrins (PZn) with different diphenyl-2-pyridylamine (DPPA) moiety surrounding the porphyrin cores. These DPPA moieties had electron deficient pyridine bridging the core porphyrin (**Figure 17e**), so the energy level and spatial interaction of adjacent molecules could be adjusted in certain levels. The DPPA group also contributes to the orientated stacking of the molecules, as the 2D grazing-incidence X-ray diffraction (2D-GIXD) revealed that the PZn–DPPA film showed enhanced face-on π-π stacking compared to the PZn–TPA film (with the (010) out-of-plane (Qz) peak at around 1.70 $Å^{-1}$ corresponding to an intermolecular π-π distance

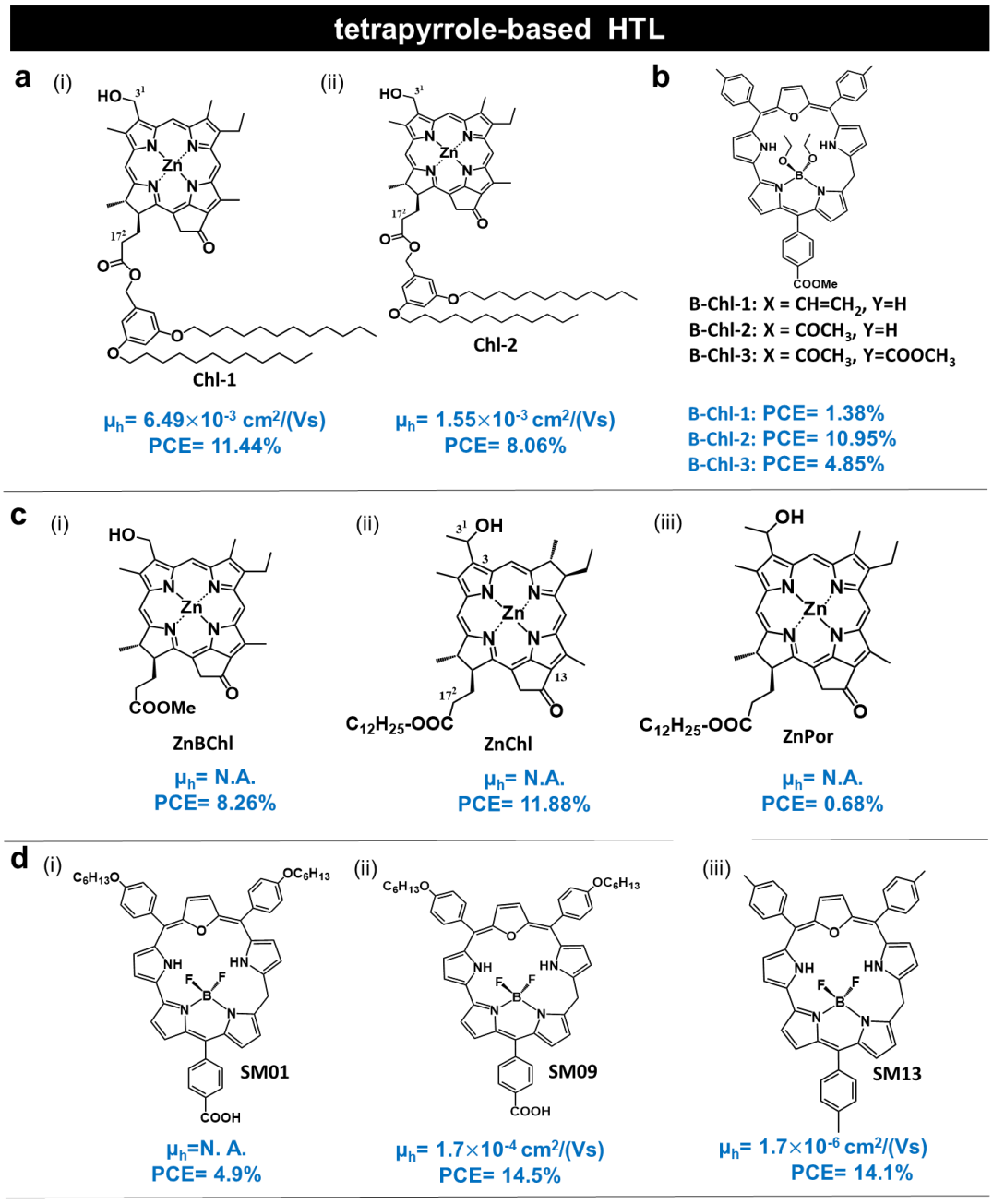

Figure 18 Molecular structure of some reported tetrapyrrole-based molecules, their hole mobility and the performance of PSCs. (a) (i) Chl-1 (ii) Chl-2, adapted with permission from Ref.[362], Copyright 2016 Wiley-VCH Verlag GmbH & Co. KGaA. **(b)** BChls, adapted with permission from Ref.[363], Copyright 2018 Elsevier. **(c)** (i) ZnBChl (ii) ZnChl (iii) ZnPor, adapted with permission from Ref.[364], Copyright 2017 American Chemical Society. **(d)** (i) SM01 (ii) SM09 (iii) SM13, adapted with permission from Ref.[365], Copyright 2017 American Chemical Society.

of ca. 3.70 Å). Such an improved face-on π-π stacking might be the reason for the promoted vertical charge transport, as observed in the mobility results. Consequently, the PZn–DPPA has the lowest HOMO of -5.36 eV and decent hole mobility of 4.10×10^{-4} cm^2 V^{-1} s^{-1}, delivering a PCE of 14.11%, comparable to the 14.61% from Spiro-OMeTAD-based reference device. Moreover, the modulation of the porphyrin based HTL can also be electronically changed through the adjustment of the functional groups. This will change the HOMO, for example, and affect the hole extraction at the perovskite/HTL interface. It has been well documented in OPVs that the incorporation of strong electron-withdrawing elements such as fluorine (F) can mitigate the π-electron cloud and downshift the energy level in certain degrees. Azmi et al.[325] employed this strategy to further decrease the HOMO energy level of porphyrin HTL to make an Ohmic contact between perovskite and HTL. Specifically, Zn porphyrin (P_{Zn})-based materials with four fluorinated triphenylamine (FTPA) substituents (P_{Zn}−2FTPA and P_{Zn}−3FTPA in **Figure 17f**) have been synthesized. As expected, the P_{Zn}−2FTPA displayed a lower HOMO of −5.37 eV compared to −5.14 eV from the non-fluorinated P_{Zn}−TPA. The P_{Zn}−3FTPA displayed a comparable hole mobility of 3.91×10^{-4} cm^2 V^{-1} s^{-1} and a higher PCE of 18.85% compared to the values of 3.37×10^{-4} cm^2 V^{-1} s^{-1} and 16.37% for the non-fluorinated P_{Zn}−TPA device. Additional works on engineering the molecular structure of porphyrin-based HTL have also been reported with the corresponding molecular structures being listed in **Figures 17g & 17h** and device performance parameters listed in **Table 5**. Beyond the scope of structural engineering of the porphyrin material, the oxidation state of the porphyrin HTL can tune the carrier concentration and consequently the electrical conductivity. For example, Cao et al.[326] developed dual valent Co(II)/(III) mixed incorporation into the porphyrins film. The Co(II)/Co(III) pair is typically known as one of the best combinations for redox process, which has been used as an electrolyte in the DSSCs.[327–329] A mixture of Co(II)P and Co(III)P [326] (**Figure 17i**) has been used as the HTL for PSCs as well. Normally the methoxy-substituted triphenylamine group in most above-mentioned porphyrin HTLs is responsible for the high solubilities in common organic solvents and the extended π-conjugation is responsible for efficient charge transport. The additional methoxy-substituted oxyalkyl chain attached at the triphenylamine group can further tune the solubility of the whole porphyrin molecule. In addition, the centered Co(II) and Co(III) serves as a redox couple to tune the oxidation level of the HTL. Consequently, both Co(II)P and Co(III)P HTLs exhibit similar hole mobility to that of Spiro-OMeTAD but slightly lower HOMO levels of -5.30 and -5.28 eV, respectively. The Co(II)P/Co(III)P mixed HTL displayed a PCE of 20.5% compared to that of ~19% from the Spiro-OMeTAD based reference cell. In addition to the role of charge transfer in PSCs, the porphyrin materials can also serve as dual functional layer that simultaneously harvests photon, excites the charges and transports these excited charges. Gao et al.[330] reported a hybrid PV cell comprised of a NIR-absorbing BHJ layer on top of the perovskite. The BHJ layer containing a mixture of DPPEZnP-TSEH and PCBM not only displayed a broad photoresponse to over 800 nm but also possessed suitable energy levels and high mobility to afford a high PCE of 19.02%. The NIR photon usage for PV conversion by the top BHJ layer is verified by the extended EQE as well as the transient absorption study. Above all, various examples referring to the changes in the meso-substitution of tetraaryl-porphyrin (such as variations of the substituents and metal centers) have been demonstrated and discussed, which can have different impacts on the energy levels, absorption feature, intermolecular interaction/stacking and its effect on the final film morphology as well as electrical properties. Additional versatility of porphyrin derivatives by reforming the cyclic tetrapyrrolic ring, such as other tetrapyrrole-based molecules (e.g., chlorins (Chl),[331] bacteriochlorins (BChl),[332] Zn(II)chlorophyll derivatives with BChl, Chl, and Por macrocycles,[333] and other core-modified porphyrins[334]) have been studied as potential HTLs for PSCs. **Figure 18** compares their molecular structures and relative performance as the HTL in PSCs. Although there have been a wide range of artificial porphyrin derivatives synthesized and employed in PV cells, the principle motif of using these porphyrin HTLs is to transfer the charge carriers through their π-conjugated electronic structure. This is relatively superficial in comparison to their delicate role in nature. For example, the *chlorophyll* in leaf cell is constructed in such a design that the energy transfer strictly follows the highly efficient Förster resonance mechanism. Instead of directly utilizing certain biomaterials as a disordered film in devices, delicately arranging the biomaterials into a subsystem (having ordered structure or delicately designed structure to evoke a highly efficient working mechanism) with maximal abilities of charge transfer might be a better solution.

4.4.2 Other natural conjugates

The porphyrins and analogous derivatives discussed above represent the most widely used materials in PVs. Particularly, their optical response featuring two absorbance bands in visible and NIR region also enable their applications as photoactive material (dye) in DSSCs. The high hole mobility also benefits their 'electron donor' role in the BHJ blend in OPVs. Apart from these porphyrins and analogous derivatives, natural pigments with aromatic fused π-conjugated structures can also be potential CTL materials in PSCs. Similar to porphyrin derivatives, most of them have been applied as photoactive dye in DSSCs. **Table 6** summarizes some of the natural conjugates, their corresponding properties and roles in nature. *Anthocyanins*, a type of flavonoid (a class of compounds with antioxidant effects), are the pigments that give different shades of red, purple, and blue to plants. *Anthocyanins* have higher chemical reactivity than other flavonoid classes, due to their specific pyrylium nucleus (C-ring) (**Figure 19a**). To exemplify, *Anthocyanins* are also ubiquitous water-soluble pigments having important roles in physiology of plants (repelling herbivores and parasites,[335] attracting pollinators and seed dispersers,[336] and protecting plants against biotic and abiotic stresses[337]), and humans (antioxidant,[338] antiinflammatory,[339] neuroprotective,[340] and anti-diabetic properties[341]). Chemically, *Anthocyanins* are weak

Table 6 Summary of natural dyes and their performance in DSSCs.

Plant source	Dye structure class	PCE (%)	Ref.
Black rice	Anthocyanin	N.A.	368
Kelp	Chlorophyll	N.A.	
Capsicum	Carotenoid	N.A.	
Mangosteen pericarp	α-Mangostin	0.92	369
Mangosteen pericarp	Rutin	1.12	
Hibiscus sabdariffa L.	Cyanidin-3-glycosides	0.37	362
Beta vulgaris rubra	Betalains	1.7	370
Bixa orellana L.	Bixin	0.37	371
Spinach	Neoxanthin	3.9	372
Spinach	Violaxanthin	3.7	
Spinach	Lutein	4	
N.A.	β-carotene	4.2	
Calafate fruit	Delphinidin	N.A.	373
Jaboticaba skin	Peonidin	N.A.	
Gardenia fruit	Crocetin	0.56	374
Red Sicilian orange "Moro"	Cyanin	0.66	375
Eggplant skin	Nasunin	0.48	

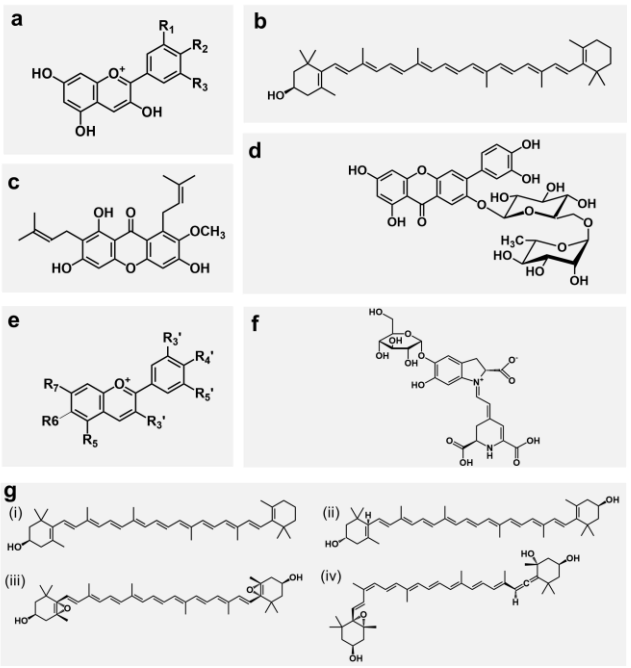

Figure 19 Other natural conjugates. Molecular structure of **(a)** *Anthocyanins*, adapted with permission from Ref.[402], Copyright 2013 Elsevier. **(b)** *Carotenoids*, adapted with permission from online resource.[403] **(c)** *Mangostin*, adapted with permission from Ref.[383], Copyright 2015 Springer. **(d)** *Rutin*, adapted with permission from Ref.[386], Copyright 2019 The Royal Society of Chemistry. **(e)** *Anthocyanins*, adapted with permission from Ref.[389], Copyright 2013 Springer. **(f)** *Betalains*, adapted with permission from Ref.[392], Copyright 2015 Elsevier. **(g)** (i) *β-Carotene* (ii) *Lutein* (iii) *Violaxanthin* (iv) *Neoxanthin*, adapted with permission from Ref.[393], Copyright 2014 Elsevier.

diacids, nucleophiles, hard and soft electrophiles, with high tendency to develop π-π stacking interactions and binding with hard metal ions.[342] The π-π stacking can facilitate the film to have higher intermolecular charge transfer, and the binding ability to metal ions can protentional passivate lattice defect in perovskites. They also exhibit the typical chemical properties of polyphenols, including an electron donor property and affinity with proteins. Their biological role in terms of transformation and catabolism in humans and effects on health is well-reviewed elsewhere.[342] *Carotenoids*, the tetraterpene pigments with yellow, orange, and red colors (**Figure 19b**) are widely distributed in photosynthetic bacteria, certain species of fungi and archaea, algae, plants, and animals, giving the characteristic color to pumpkins, carrots, corn, tomatoes, canaries, flamingos, salmon, lobster, shrimp, and daffodils.[343] The *Carotenoids* are conjugated double bond compounds with recurring isoprene units, which are responsible for the π-electron delocalization along the backbone and thereby a certain level of electrical conductance. All *carotenoids* are highly lipophilic and exhibit low solubility in water, making them potential materials for introducing hydrophobicity to the moisture-sensitive perovskite materials in PSCs. Their conjugated nature also makes them antioxidants (inactivate the reactive oxygen species and oxidative damage, which is essential to the immune system), attractants, and UV attenuators.[344] Recently, *carotenoids* have received growing attention because of their therapeutic values and health benefits and as well as their applications in the perfume and food industries.[345,346] *Mangostin*[347] is the major xanthone from *Garcinia mangostana* (whose fruits are referred to the 'queen of fruits' in Thailand[348,349]) and has been utilized as the starting material for semisynthetic preparation of multiple biologically active derivatives. Its structure is shown in **Figure 19c**, with presence of multiple instances of including two prenyl chains, three phenolic hydroxyl groups and two unsubstituted aromatic carbons. *Mangostin* displays chemopreventive properties in medical applications. In PV applications, *Mangostin* is used as the dye in DSSCs (exhibiting relatively low PCE of 2.63%.[350] *Rutin* (3,3',4',5,7-pentahydroxyflavone-3-rhamnoglucoside, shown in **Figure 19d**) is a flavonoid pigment in medicinal plants (usually found in sources such as *buckwheat*, *Japanese pagoda tree*, *Eucalyptus*, *hawthorn*, lime tree flowers, elder flowers, etc.) and is used to make medicine (responsible for various pharmacological qualities including antioxidant, anticarcinogenic, cytoprotective, vasoprotective, neuroprotective and cardioprotective properties). As the natural antioxidant, Rutin has been reported as the reducing agent in synthesis of Ag NPs[351,352]. The *Rustin*-modified Ag NPs can be used as a chromogenic probe for metal ions in aqueous environments.[353] Elseman et al.[354] reported the strategy of silver chelation on *Rutin* as an additive for increasing the hole conductivity in HTL. The *Rutin*-modified Ag NPs blended PHPT-py HTL led to a PCE of 21.1% for the PSC while the reference cell using the typical Spiro-OMeTAD HTL only has a PCE of 20.8%. This is due to the re-oxidation effect by *Rutin*–Ag NPs on PHPT-py HTL, enhancing the electrical conductance of the HTL. The deoxidized *Rutin* can be easily oxidized by oxygen and these oxidized states of *Rutin* can be further reduced by PHPT-py HTL. Hence, the catalytic role of *Rutin*–Ag NPs improves the property of the PHPT-py HTL. Meanwhile the chelation-like *Rutin*–Ag NPs complex restricts the migration of halides group in perovskite and consequently improves the

operational stability of the PSC device. Overall, the *Rutin*–Ag NPs could be a promising additive to the existing HTL materials in PSCs. *Anthocyanins* (a type of flavonoid with antioxidant effects, the structure is shown in **Figure 19e**) are found in vibrantly colored fruits, leaves, and flowers capable of attaching to transition metal oxides (TMO) such as TiO_2 surface which has been reported as the photo-sensitizer in DSSCs.[355,356] Although *Anthocyanins* pigments are abundant in nature, isolated *Anthocyanins* are highly degradable,[357] depending on several factors such as pH, storage temperature, and sunlight exposure.[358] *Betalains* (**Figure 19f**) are a class of yellow and red tyrosine-derived pigments found in the *cactus Mammillaria* flower petals, red *beets*, *Swiss chard*, *Amaranthus caudatus*, etc. *Betalains* exhibit many attractive properties including antioxidant, anti-cancer, anti-lipidemic and antimicrobial properties.[359] *Betalains* are water soluble with functional –OH and –COOH groups which can make it easy to attach TMOs. Other commonly used natural dyes as photon absorber in DSSCs include the chain-like molecules such as *β-Carotene* (non-polar compound and highly lipophilic, shown in **Figure 19g(i)**), *Lutein* (lipophilic and generally insoluble in water, shown in **Figure 19g(ii)**), *Violaxanthin* (a natural xanthophyll pigment, shown in **Figure 19g(iii)**), *Neoxanthin* (a carotenoid and xanthophyll, shown in **Figure 19g(iv)**).[360] There is a wide range of natural pigment materials where the large π-electron conjugation enables visible light absorption and hence the coloring properties of these materials. The π-electron conjugation and delocalization also make it possible for charge transport in a certain range. Considering their application as CTL in PSCs, an intermolecular hopping mechanism must be feasible, requiring close intermolecular packing of these natural pigment within the thin film. Additionally, intentional doping to increase the charge carrier density or improve other mechanisms such as radical assisted transport and/or organic transport can be possible routes

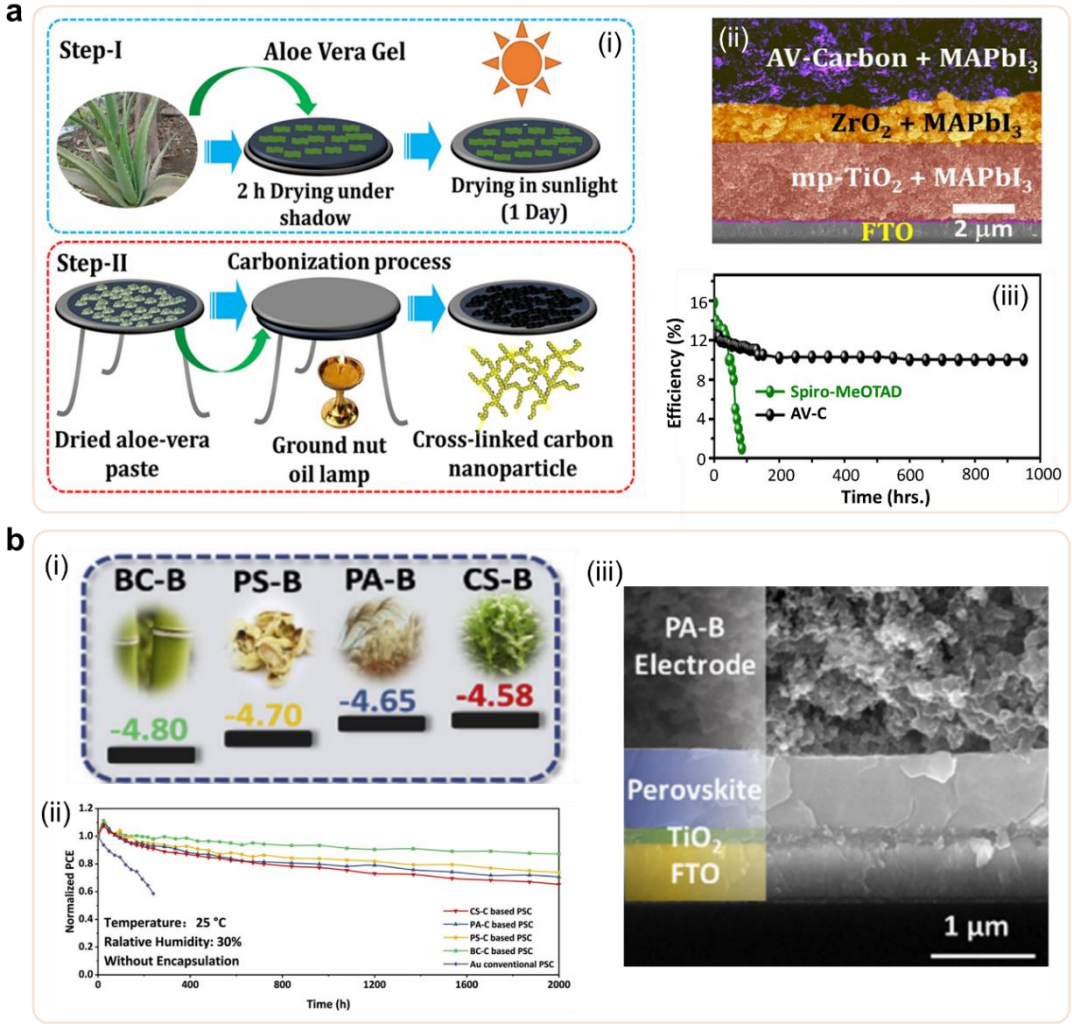

Figure 20 Carbonized natural materials for charge transportation in perovskite solar cell. (a) (i) Schematic illustration for preparation process of aloe-vera (AV) cross-linked carbon nanoparticles via an ancient Indian method. (ii) Cross-sectional SEM image of perovskite solar cell device based on AV-carbon electrode. (iii) Comparison of Air stability of unencapsulated conventional spiro-MeOTAD and AV-carbon PSCs at 35% relative humidity, adapted with permission of Ref. [415], Copyright 2018 American Chemical Society. **(b)** (i) HOMO level diagram of various bio-carbon electrode. (ii) Stability tests of perovskite solar cells with various bio-carbon electrode at 30 % relative humidity. (iii) Cross-sectional SEM image of perovskite solar cell with bio-carbon electrode, adapted with permission from Ref. [416], Copyright 2020 Elsevier.

towards highly efficient CTLs applied in PSCs. Although applications of these natural conjugates as CTLs in PSCs remains unexplored, their potentially high charge carrier mobility, tunable energy level, good solution-processability and benefits compared to artificial materials (*e.g.*, low-cost, abundance in supply, and reliable stability) may trigger new protocols for more efficient CTL for PSCs.

4.4.3 Carbonized natural materials

Carbonized materials can be directly obtained from natural sources through high-temperature sintering and are advantageous due to their low-cost, versatile microstructures and high chemical/thermal stabilities. Mei et al.[361] reported the pioneering work of using a porous carbon film as an efficient and stable hole collection layer in PSCs. Carbon-based hole collection materials also exhibit good air/water stability[362–364] and high compatibility for easy manufacturing such as doctor-blade,[365] screen printing,[366] and electrospray[367] printing. These attributes make it a promising material for an anode in PSC devices and their extended applications in MPS. Particularly from the cost perspective, carbon-based PSC could significantly reduce the levelized cost of electricity (LCOE) of the PV MPS in contrast to those using metal electrodes.[368]

Compared with the synthesis of existing state-of-the-art charge collection materials which requires tedious and complex processing and expensive precursors, carbonized natural organics with delicate microstructure are good alternatives. For example, activated carbon with microstructures (*e.g.*, hierarchical porous structure) for supercapacitor applications can be synthesized from natural corncob[369] and lignin of wood.[370] In application for Li-ion batteries, hierarchically porous nitrogen-rich carbon as the anode material has been derived from wheat straw.[371] Similarly in PSCs, using an ancient Indian method, Mali et al.[372] designed an ecofriendly route to extract cross-linked carbon nanoparticles from Aloe-Vera as HTL and electrode to achieve the printable PSCs, as schematically illustrated in **Figure 20a**. The authors extracted Aloe Vera gel from leaves and dried them under sunlight to obtain intermediate carbon powder. After being washed with acid, the product was annealed at a high temperature (1,000 °C). The final product was crosslinked carbon nanoparticles with uniform size (denoted as AV-C) (**Figure 20a(i)**). The screen-printed carbon film from the AV-C carbon paste showed outstanding conductivity (~7 Ω cm^2) compared to one made from a commercial colloidal carbon paste (~80 Ω cm^2). With the AV-C carbon, a fully printable triple-layered mesoporous scaffold consisting of TiO_2/ZrO_2/AV-C based PSC showed a PCE of 12.75 % (**Figure 20a(ii)**), higher than the device using commercial carbon ink (10.53%). In addition, unencapsulated device based on AV-C showed small PCE decrease after 900 hrs. in ambient air with relative humidity of 35% (while the reference PSC fails after 100 hrs. operation) (**Figure 20a(iii)**). Gao et al.[373] also synthesized various bio-carbon materials through pyrolysis of common plant waste including corn stalk (CS), peanut shell (PS), phragmites australis (PA) and bamboo chopsticks (BC) (**Figure 20b**). Results demonstrated that all of the aforementioned carbon materials could work as the HTL/electrode layer for PSC (**Figures 20b(i) & 20b(ii)**). The cell based on biocarbon extracted from BC exhibited the best performance compared to the others with a PCE of 10.30%. It should also be noted that the cell based on the biocarbon exhibited exceptional stability compared with the conventional PSC, and BC-based cell exhibited nearly 90% of PCE retained after 2,000 hrs. in ambient conditions with 30% relative humidity (RH) (while reference device failed after 300 hrs.) (**Figure 20b(iii)**).

Overall, carbon-based hole collector layer in PSC enables the exemption of expensive HTL and could further reduce the cost because of the replacement of noble Au with carbon. In addition, carbon and derivatives as highly conductive charge collectors are abundant in nature as most organics are carbon-based materials able to be carbonized through various established techniques. Employment of these natural carbonized materials still needs to follow the principles of (i) excellent electrical conductivity and charge carrier mobility, (ii) uniform micro-structures with minimized pores, traps and defects, (iii) small and uniform particle size as well as good and dense film morphology, (iv) high purity and stability, and (v) good compatibility to up-scaling manufacturing, in addition to their unique (vi) ability of inheriting microstructures from their original natural carbonate sources. In particular application in perovskite solar cells, carbon electrodes or carbonized CTL with extremely low manufacturing cost is one of biggest thrusts for commercialization. Utilization of already carbonized or direct use of carbon electrodes has been reported. While use carbonate sources in vitro followed by post carbonization in order to further simplify the manufacturing may offer additional potentials for innovative device fabrication.

5. Perovskite Photoactive Layer

The perovskite photoactive layer in PSCs is responsible for photon absorption and a subsequent quick conversion into a free electron and a hole, thanks to its low exciton binding energy, so room-temperature thermal heat can separate the excitonic electron-hole pair into free charges. To maximize the photovoltaic efficiency in these photoactive layers, properties including *(i) efficient photon absorption* (e.g., broad spectral response, high light-distinction coefficient, long lifetime of excited states, clean band structure with minimized density of shallow trap-states or in-band traps) and *(ii) efficient excited charge transport towards corresponding electrodes* (e.g., high electron & hole mobility to ensure less potential energy loss and charge density loss during transit, ambipolar transport ability that enables opposite drifting of excess photon-excited electrons and holes under external electric field). These requirements are exactly met by perovskite materials, which have a good band structure (direct bandgap and a high optical absorption coefficient of 10^5 cm^{-1}), tunable energy level (bandgap ranges from 1.15 to 3.06 eV), long exciton diffusion length (1 μm in polycrystalline film and 100s μm in single crystals), sharp DOS at VBM and CBM and low effective masses, and high electron & hole mobility.[11–15] This makes the perovskite the current optimal platform for PV application. In addition to this, PSCs

with specific type of production will need additional attributes. For example, for PV-MPS applications, PSCs may require high mechanical properties (*e.g.*, flexibility for curved UAV wings, fabrics and other wearable implementations), higher stability and efficiencies for outdoor applications (*e.g.*, PV-tile roof under extreme weather conditions), and some other specific features (*e.g.*, transparency for PV-window; high vacuum/pressure endurance for spatial application). Under these considerations, bio-inspired strategies (including delicate structures, chemically functional biomolecules and their hybrids with the target materials)[374] can be helpful in adding new functionalities to the current base-line PSC platforms. For more specific example in terms of mechanical properties, natural materials with sophisticated microstructures (such as columns of circular layers in wood or bone, or the complex helicoidal chitin fibers in the stomatopod club) can be simultaneously light-weight, strong, flexible and tough; some of them can be porous with a hierarchical design to provide paths for efficient mass transport and/or to reduce weight; many natural materials are also able to self-repair repeatedly without any external interreference; such natural materials can also be built with a relatively limited number of components and simple structure under minimized energy supply in a highly efficient manner. Finding the common design themes among them and developing novel bio-inspired paradigm is hence reliable; some of which have already been successfully applied in different fields.[375] In terms of PV, these bio-inspired strategies in enhancing the original properties or adding new attributes to current perovskite photoactive layers are expected to expand the horizon of the development of PSC-based MPS.

5.1 Biomimetic architecture

5.1.1 Nacre

Enhancing the mechanical properties (toughness, bendability, etc.) of PSC is important, particularly with consideration of portable, foldable and mobile power applications. Natural hybrid materials such as nacre and bone exhibit remarkable toughness and strength. **Figures 21a** and **21b** summarize and compare the mechanical properties between natural and artificial materials. In fact, most natural materials are composites of certain forms, including polymeric (e.g., polysaccharides, proteins) and ceramic (e.g., silica, calcium salts) components or composite building blocks.[376–380] From this toolbox, a wide range of hybrid materials (such as wood, bamboo and palm, comprising cellulose fibers within a lignin–hemicellulose matrix; insect cuticle, comprising chitin in a protein matrix) are assembled materials. Similarly for nacre, its hybrid composite design gives the primary strengthening and toughening mechanisms.[381] More specifically, nacre has a 'brick and mortar' micro-composite structure (**Figure 21c**). The bricks are crystalline *aragonite* ($CaCO_3$) platelets with a dimension of 0.5 μm thickness and 8-10 μm width, providing strength; while the mortar (20–50 nm thick) is a biomolecular adhesive composed of proteins and chitin, allowing for toughness and ductility.[382] This alternative laminar multilayer structure has multiple toughening mechanisms including crack bridging, pulling/sliding of *aragonite* platelets, crack propagation deflection and energy dissipation by the organic layer,[383,384] which are well discussed in prior review works.[375,385] Such a hierarchical structure from nacre has inspired the engineered materials in PSCs with remarkable toughness and mechanical strength. In PSCs, one of the major challenges is the brittle nature of halide perovskite film. It is difficult for the perovskite material to meet the stretchability, twistability and bendability requirements of the PSC device and the final MPS products able to accommodate the complex human body movements.[95,386,387] Inspired by the promising results for biomimicry study of nacre in other electronically applied materials (*e.g.*, interface-reinforced graphene-based fibers[388], reduced graphene oxide–poly(acrylic acid) nanocomposites[64]), researchers attempt to adopt the nacre concept to enhance the reliability of mechanically flexible PSC. Hu et al.[96] mimicked the natural mineralization process of nacre by introducing two polymers of poly(styrene-co-butadiene) (SBS) polyurethane (PU) into the perovskite (**Figure 21d**) to modulate the mechanical feature of the perovskite photoactive layer. The SBS serves as a scaffold that reduces the nucleation energy barrier and induces heterogeneous nucleation of perovskite. Meanwhile, PU undergoes chemical interactions with the perovskite precursors which suppresses the nucleation rate. Mediated by the synergistic effect from SBS and PU, the resultant photoactive film exhibits oriented grains. Owing to the stress release effect by the elastic polymeric matrix, the PSC exhibits outstanding bendability and stretchability (**Figure 21e**). The SBS-PU based PSC module shows no clear PCE decrease after bending in 2 mm curvature for 5,000 cycles compared to 80% PCE loss in a reference device.

5.1.2 Other promising structures

There is a wide range of potential natural examples for mimetic implementation in PSCs. These delicate structures can be applied in designing mechanically qualified PSCs and their terminal MPS products. Mechanically, beyond the aforementioned specific strength, stiffness, and Young's modulus in **Figure 21b**, another important figure-of-merit is the specific energy absorption (SEA), which defines the absorbed energy by a structure per unit mass. The SEA can be calculated from the force-displacement (F-D) characteristic (exemplified in **Figure 22a**) of the target material, by the equation of $SEA(d) = (EA(d))/m$, where d is the displacement, EA is the energy absorbed by the material as represented by the shaded area under the F-D curve, m is the mass of the target material. Similarly, SEA per unit volume (SEA_V) defining the energy absorbed per unit volume can also be calculated by the equation of $SEA_V(d) = EA(d)/V$, where V is the volume of the energy absorber. **Figure 22b** shows the SEA_V of various biostructures with respect to conventional (simple artificial) structures. Among them, the honeycomb-like sandwich architectures have been widely observed in nature, such as turtle shells and beetle forewings (**Figure 22c**), and has been utilized to design strengthened carbon fiber reinforced plastic (CFRP) panels[389] with greater energy absorption and lower peak load for construction application. Similarly, the telson (tail plate) of the

Stomatopoda (mantis shrimp)[390] (**Figure 22d**) exhibits excellent mechanical impact resistance because of its special structure, which has been mimicked for designing corrugated panels. The augment of the impact resistance comes from the significantly

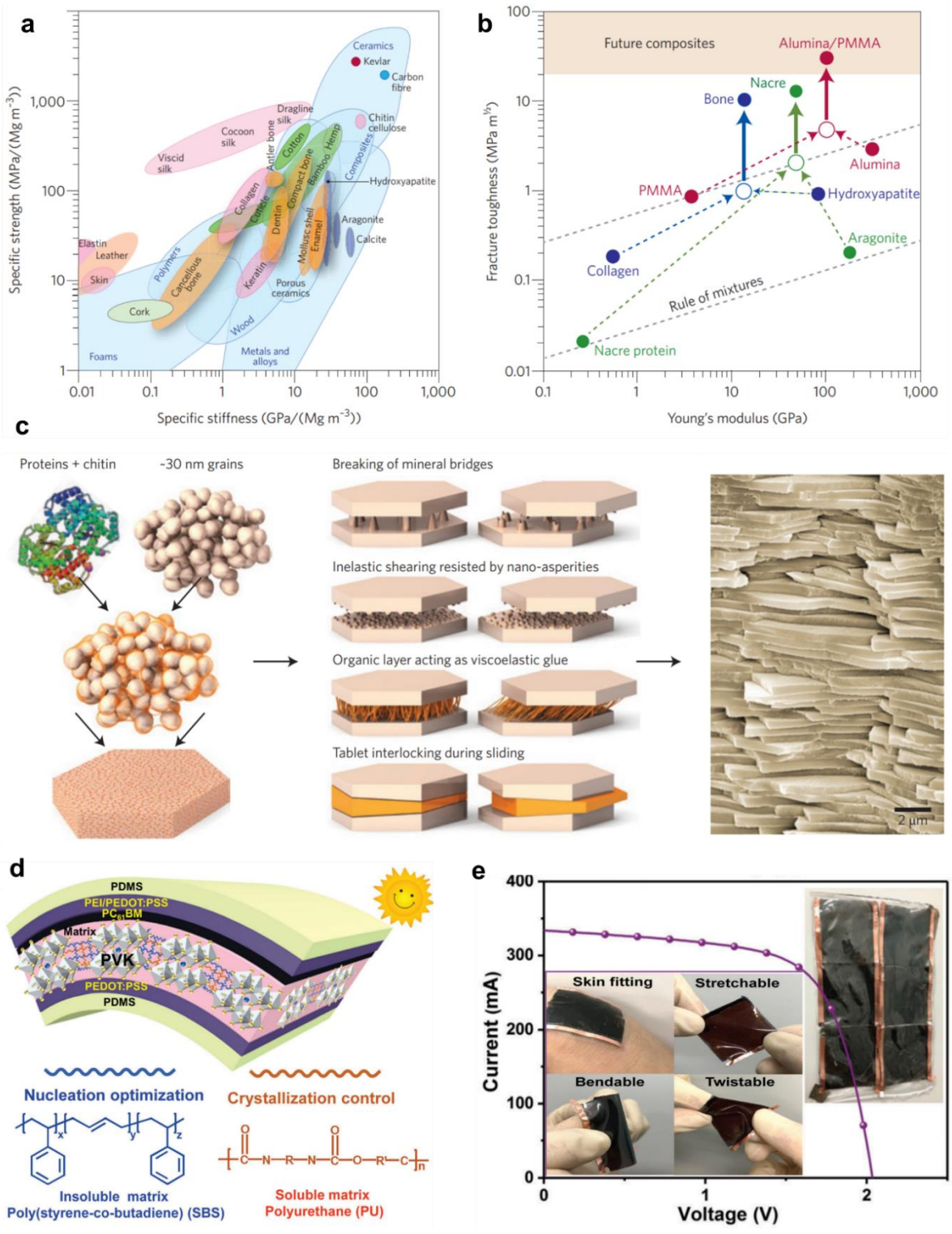

Figure 21 Biomimetic architecture of perovskite layer. (a) Ashby plot of the specific values of strength and stiffness (or Young's modulus) for various natural and synthetic materials. **(b)** Young's modules and Fracture toughness of various biomaterials as well as synthetic materials **(c)** The hierarchical structure pf nacre, adapted with permission from Ref.[418], Copyright 2014 Springer Nature. **(d)** Scheme showing the nacre-inspired wearable solar module and microstructure for the perovskite layer consisting of soluble PU (blue) and insoluble SBS (orange) matrix. **(e)** Photo image and measured I-V curve of the wearable solar module constructed with nacre-inspired perovskite layer, adapted with permission from Ref.[99], Copyright 2019 The Royal Society of Chemistry.

improved the crashworthiness and reduced initial peak force in these bio-inspired sandwich panels.[391] Another candidate for designing the bio-inspired structures for mechanical energy absorption is the head of a woodpecker.[392–394] Several studies in

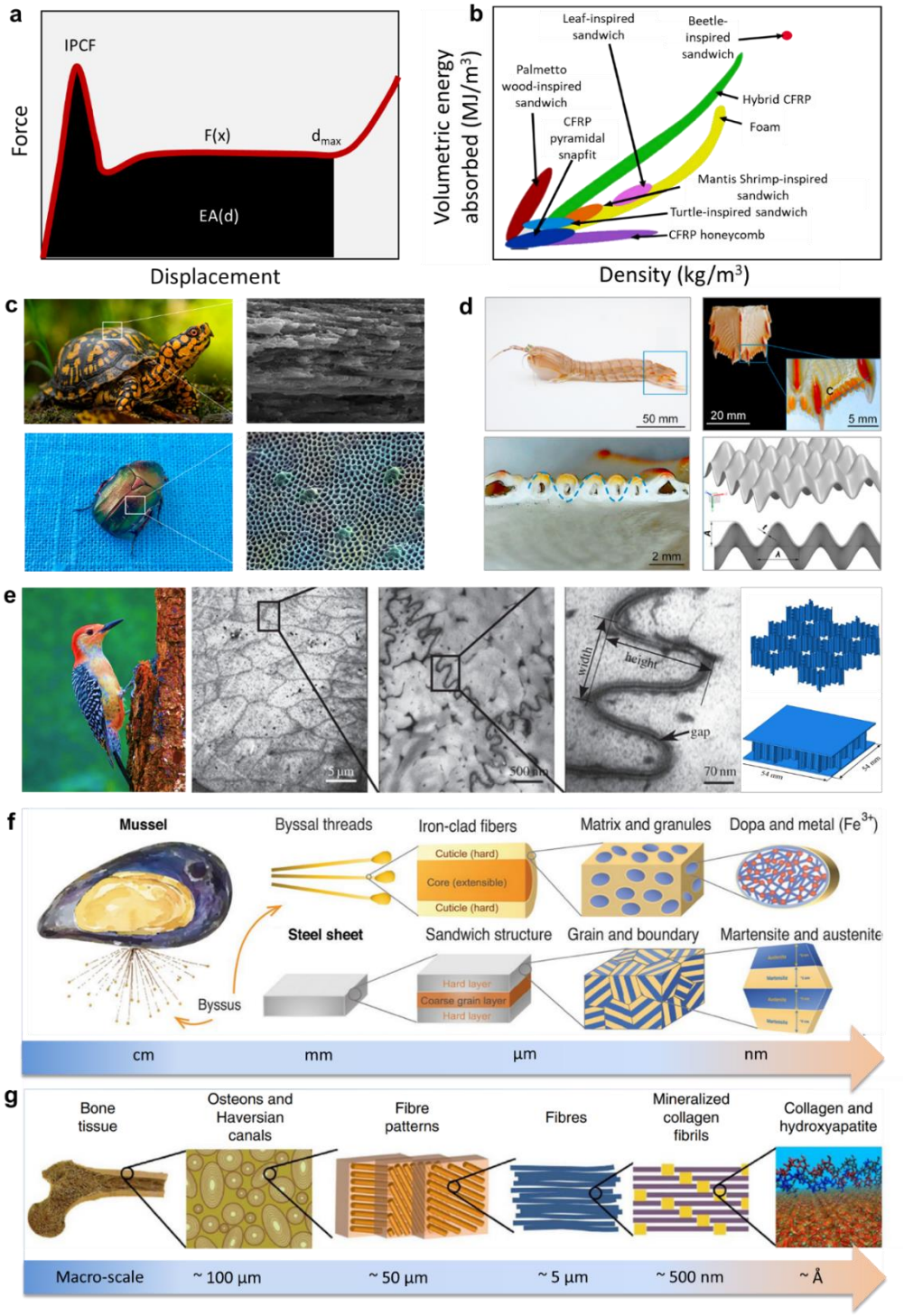

Figure 22 Other promising structures. (a) The Force-displacement relationship of various energy absorbers. The shaded area under the curve represents the energy absorbed. **(b)** The specific energy absorption (SEA) of bio-inspired sandwich structures, adapted with permission from Ref.[444], Copyright 2020 Elsevier. **(c)** Honeycomb sandwich structures in turtle shell and beetle forewings, adapted with permission from online resources[445–447] and Ref.[432], Copyright 2017 Elsevier. **(d)** Bio-inspired sandwich structure mimicking the shrimp, adapted with permission from Ref.[444], Copyright 2020 Elsevier. **(e)** Photo of a woodpecker, TEM image of the rhamphotheca of woodpecker's beak showing its nanostructure, and schematic illustration of the structure, adapted with permission from Ref.[448] and Ref.[437], Copyright 2014 The Royal Society and 2019 Springer. **(f)** A mussel inspired hierarchical Steels, adapted with permission from Ref. [442], Copyright 2017 Springer Nature. **(g)** Hierarchical structure of bone ranging from microscale skeleton to nanoscale collagen and hydroxyapatite. adapted with permission from Ref. [449] Copyright 2013 Springer Nature.

mechanical engineering have been done to mimic the woodpecker's head structure to improve low-velocity impact behavior for a sandwich beam structure (which is superior to the conventional beams, with a lower developed stress, smaller damage area and less deformation, while sustaining a higher maximum impact force).[392] Unlike conventional honeycomb, the walls of the woodpecker's beak-inspired honeycomb structure are wavy (**Figure 22e**).[394] This structure enables superior absorption capability of mechanical energy compared with 125% enlarged SEA. Besides those high SEA structures inspired by animals, structures from plant are also of interest. For example, by mimicking the composite structure of *Palmetto* wood, bio-inspired 'sandwich' composite structures using carbon fiber reinforced plastic sheets and polymeric foam core have been developed and well-investigated.[395] Similar examples can be found in the leaf structures,[396,397] where the core is designed by filling honeycomb into a proper ortho-grid, with improved specific strength and energy absorption. In addition, the hierarchical structures inspired by the leaf can further improve the loading capacity.[398] Another hierarchical design to enhance mechanical strength could be found in hard shell animals. For example, the hierarchical structured mussel shell is typically strong and tough. As can be seen from **Figure 22f**, the shell consists of micro byssal threads. The byssal threads are in a sandwich structure at the micro-scale, made of a matrix and granules which vary in cross-linking density. The granules contain a higher cross-link density than the matrix and this controls the difference in local mechanical properties and allows a good stress dissipation and mechanical energy absorption when the shell is stressed. Inspired by this design, researchers developed a hierarchical steel comprised of a hard layer and a coarse-grained layer to deliver vastly superior mechanical properties.[399] This hetero-composite design may also be applied in a perovskite solar cell device. For example, by using a polymeric matrix to blend with the perovskite to form a BHJ composite, so that the polymer could (i) allow sufficient stress-energy dissipation, store the strain and consequently lead to good mechanical toughness for the composite, or (ii) allow a 'healing process' after damage *via* re-bonding the neighboring broken grains to heal the crack. Either way, from an electrical perspective, a conjugated polymer with certain electrical conductivity is of paramount importance to ensure a good PCE. Stress-tolerance for PV-MPS also includes the dynamic endurance, which means the device needs to have a high lifetime able to handle many cycles of folding-opening-refolding. This will require a good inner friction tolerance to avoid any serious fractures of the multiple layers in the device under the condition a large bending angle. A natural example bearing both good hardness and flexibility or mobility is the bone and joint.[400] These could be attributed to the remarkable hierarchical architecture of bone, constituted by both the soft collagen protein and stiffer apatite mineral (**Figure 22g**). Bone's universal elementary building block is the mineralized fibrils, which is assembled by collagen molecules and mineralized by apatite crystals. In the body, the bone tissue functionality is related to stiffness that is determined by the collagen/mineral ratio. For instance, ear bone has over 80% of mineral content so that it is sensitive and vibratile with applied acoustics. In contrast, long bone with 20% mineral content, which is light-weight to enable mobility, could absorb the mechanical energy.

Overall, there are various promising structures formed at ambient temperature in creatures that have specific high mechanical properties. Nevertheless, there is limited success in mimicking such functional structures for applications to improve mechanical properties for PSCs. Challenges mainly include the lack of reliable approaches for translating these 'design motifs' found in natural materials to a specific utilization in solar cell application, as well as the technical challenges of making these bioinspired structures using perovskite materials that can be installed within a PV device. Nevertheless, there is exciting potential within the vast inventory of natural examples with delicate structures that may lead to inspiring design principles/rules and highly efficient functionalities implemented to minimize energetic consumption. For example, preparing a nanostructured perovskite layer using the precursor ink of perovskite and a micro-mold (*e.g.*, PDMS mold) could be a good way to manufacture a mechanically stable and optically multifunctional film, and the mold pattern could be mimicked from the nanostructures from shrimp shell, woodpecker's beak or beetle forewings. Learning and understanding these natural designs, and eventually manufacturing and implementing them in products requires the development of advanced nanomanufacturing techniques, which can be a long-term, costly project, but may have a ground-breaking impact to the broader community outside of the PV field. Overall, the nature provides a huge library of 'design manuscript', how to utilize them to optimize existing models and even make innovations, and the challenges in developing more advanced tools are the two prior problems to address now.

5.2 Self-cleaning

For real applications of PV-MPS, weather conditions such as rain, snow, wind, and dust need to be taken into consideration. A device with a self-cleaning feature could ensure a stable power output and extend its lifetime. In the following section, several natural prototypes for self-cleaning and corresponding self-cleaning solar cells will be discussed.

5.2.1 Lotus effect

Lotus leaves possess special water repellency and surface non-wettability, where water droplets cannot stably adhere to the surface of leaves (or petals in some cases) but spontaneously roll away or bounce off. In this way, dirt particles and dust can be routinely removed from the leaves or petals, which is usually called the 'lotus effect' or 'self-cleaning lotus' (**Figure 23a**).[401,402] This non-wetting property originates from the nano- and microscale hierarchical cilium-like structures superimposed on top of micro-papillae, as well as an epicuticular covering of low surface energy wax on these papillae (**Figures 23a(ii)** and **23(iii)**). This structural topography at the surface with a significantly large surface area could generate a higher energy barrier at the interface between the liquid and solid, but also trap

the air below the water droplets forcing them to partially sit on a membrane of air. These effects jointly give rise to a superhydrophobic property at the surface (contact angle >150° and a sliding angle < 5°).[401,403] Super-hydrophobicity of these

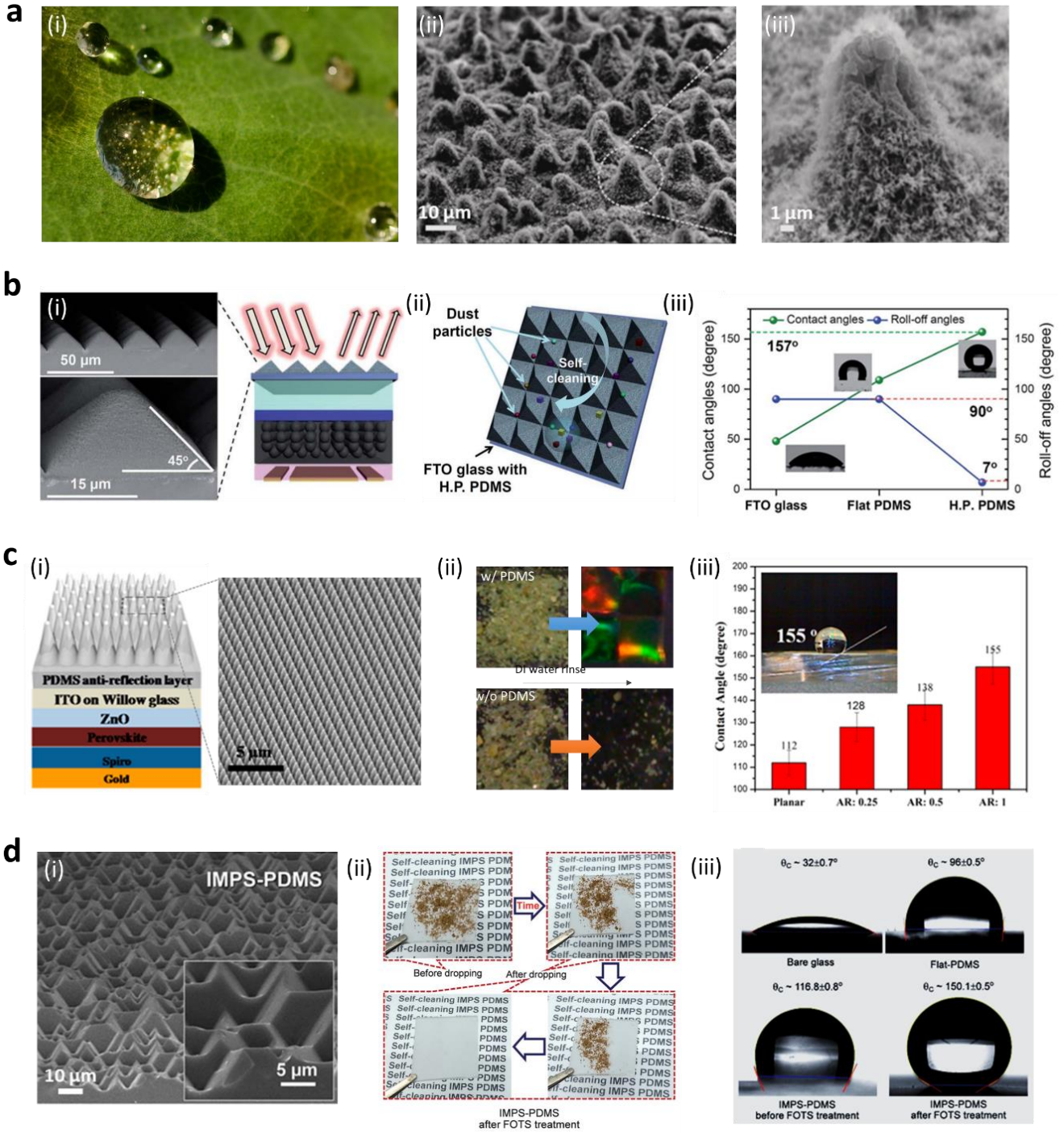

Figure 23 Lotus-inspired structures for self-cleaning. (a) (i) Image of water droplet on lotus leaf, adapted from online resource.[458] (ii)&(iii) SEM image of lotus leaf surface, adapted with permission from Ref.[450], Copyright 2008 Wiley-VCH Verlag GmbH & Co. KGaA. **(b)** (i) Schematic illustration and SEM images of the PDMS hierarchical pyramid arrays. (ii) Schematic illustration of the self-cleaning effect on the hierarchical pyramid PDMS surface. (iii) Static contact angles (green line) and roll-off angles (blue line) of water on three different surfaces, adapted with permission from Ref.[452], Copyright 2014 The Royal Society of Chemistry. **(c)** (i) Schematic illustration of the nanocone PDMS film attached on the top of a perovskite solar cell. (ii) Self-cleaning experiment of the perovskite solar cell devices with and without the nanocone PDMS film. (iii) Contact angles of water droplet on the structured PDMS layer with different aspect ratios, adapted with permission from Ref.[140], Copyright 2015 American Chemical Society. **(d)** (i) SEM image of the inverted micro-pyramidal structured PDMS layer (IMPS-PDMS). (ii) Sequential photographs of the water droplet cleaning behaviour of the IMPS-PDMS film with fluoro-octyltrichlorosilane (FOTS) treatment. (iii) Photographs of a water droplet on the surface of IMPS-PDMS samples before and after the FOTS surface modification, adapted with permission from Ref.[456]. Copyright 2016 The Royal Society of Chemistry.

solid surfaces is crucial for self-cleaning of glasses, anti-icing and prevention of snow adhesion to glass surfaces, and anti-corrosion/anti-biofouling.[404]

5.2.2 Lotus-inspired PSC

Such a self-cleaning property is an important attribute for practical usage of solar cells, particularly in application in remote desert areas (e.g., Africa, Middle East, four-season countries[405]), some industrial areas (e.g., with accumulation of dust, snowfall and airborne dirt from factories) and solar-driven robotic spatial exploration (e.g., The Mars 2020 Perseverance Rover mission of NASA's Mars Exploration Program[406]). The accumulation of particles from the surrounding environment on the surface will block the light and compromise the output power of PV cells/panels/modules. Currently, cleaning methods to remove these particles include the electrostatic method, mechanical method, and coating method for PV product surface cleaning.[405] Considering the energy for the cleaning process, the coating method with a specific surface microstructure design is of great interest. In the case of PSCs, Kang et al.[403] reported on the water-repellent PSCs based on PDMS films with lotus leaf-inspired hierarchical arrays well-equipped with a self-cleaning capability. The structured PDMS film is additionally attached (due to strong van der Waals interaction between PDMS and glass) to the glass side of a PSC which can enhance the light incidence by an anti-reflection effect while have a self-cleaning functionality. **Figure 23b(i)** shows the scanning electron microscopy (SEM) images of the PDMS layer with hierarchical pyramid arrays (having a 45° angle at the bottom edge side). This hierarchical structured PDMS layer creates a super-hydrophobicity on the surfaces leading to a self-cleaning effect (**Figure 23b(ii)**), where the dust particles could be removed easily by water droplets rolling off across the surface, due to the large contact angle of 157° (**Figure 23b(iii)**). This additional lotus-inspired PDMS thin sticker layer hence exhibits an easy but effective way to make self-cleaning PSCs. Similarly, Tavakoli et al.[137] also reported a nano-cone array of an antireflection film attached on to the front electrode of the substrate in order to improve the water-repellence as well as the optical transmittance. The PDMS film (thickness of 0.2 mm) with a nanocone array pattern (1 μm pitch and 1 μm depth, as shown in **Figure 23c(i)**) was fabricated by molding from an

Table 7 Self-healing/defense mechanisms found in living nature (partially referred from multiple references425).

Flora & Fauna		Healing activities (Physical change)	Healing/defence description	Mechanism(s)	Ref
Plants	***Herbaceous plants***	Wound closure	Seal-off and grow (production and maturation of callus parenchyma)	Cells swell, divide, and harden at the surface	442
		Secretions after injury	Latex, gum, or volatile oils are released to aid healing, upon breach	Punctured cell induces a localized response	426,427
		Innate immune response	Pattern-recognition of microbe attack	Cellular response for specific cell response	443
	Woody plants	Bark (epidermis) and roots (rhizodermis) growth	Continual production of thick outer layers (tree bark and root bark) protecting inner layers	Continual replenishment of the hard, protective layers	444–446
Animals	***Vertebrates***	Central nervous system (CNS) injury response	glial cells in the extracellular matrix quickly form scar tissue to maintain homeostasis	Clearing of debris and rapid system stabilization	447,448
		Peripheral nervous system (PNS) injury	Schwann cells clear the area around the axons and allow for repair	Clearing of debris and rapid system stabilization	447,448
	Vertebrate (hard tissue)	Bone break	Cellular response: inflammation, cartilage callus formation, lamellar bone generation and remodelling	A series cellular activity (bone sides stabilization, remodelling, mineralization, etc.)	433
	Vertebrate (soft tissue)	Wound	Cellular clotting, inflammation, proliferation, and remodelling	Cellular signalling from short-term clotting to long-term cell remodelling	449
		Stem cell response	Stem cells replicate and differentiate into target cell for new tissue growth	Adapted healing by tissue regrowth	450,451
		Molting (shedding) and replenishment	Replacing old and dead tissue to accommodate new growth (*reptiles*) or seasonally (*birds*)	Shedding of the outermost layer (*skin, feathers, hair*)	452,453
	Invertebrate (hard tissue)	Wound	(Incest's') endocuticle secretion from the cellular epidermis	Continual growth of exoskeleton from soft inner layer	454
		Exoskeleton growth and ecdysis	Organism outgrows its current exoskeleton	Periodic replacement of newly grown exoskeleton	455
	Invertebrate (soft tissue)	Wound	Clotting (plasma protein reactions, blood cell aggregation, or cell population increase) & cellular healing	Clotting through dense hemocyte network, hemocyte/plasma coagulation, cell reproduction	456

imprinted Al foil template which was first prepared via a multistep anodization coupled with a wet etching process. **Figure 23c(ii)** shows the 'dust self-cleaning experiments', where the dust/small particles can be easily removed from the device by rolling water droplets across the surface sufficiently cleaning the dusty surface. Furthermore, the aspect ratios (defined by height of nanocones over periodicity) of the PDMS nanocones can be tuned through the molding process. Besides the inverted micro-pyramidal structured (IMPS) PDMS coating film, incorporation of an additional hydrophobic layer can further enhance the self-clean effect for the device. Dudem et al.[407] reported the fluoro-octyltrichlorosilane (FOTS)-coating on the surface of the micro-pyramidal PDMS (**Figure 23d(i)**) and obtained a superhydrophobic behavior with a very large water contact angle of 150° (**Figure 23d(iii)**). The micro-pyramidal structured PDMS was prepared by peeling from a Si-mold after curing at 75 °C for 2 hrs., followed by a treatment (rinse) of a mixture of trichloro(*1H,1H,2H,2H*-perfluorooctyl) silane and *n*-hexane for several minutes and dried in an oven at 30 °C for 12 hrs. The self-cleaning behavior of a FOTS-treated IMPS-PDMS film was tested by dropping water on dust covered film. **Figure 23d(ii)** shows the efficient self-cleaning process. In real outdoor conditions, these nano/micro-structured PDMS films with a super-hydrophobic surface have exhibited an efficient self-cleaning ability when exposed to raindrops, and the PSCs integrated with the PDMS layer showed good device stability for 32 days.[408]

5.2 Self-healing

5.2.1 Self-healing in nature

'Healing' is defined as the act or process of curing or of restoring to health.[409] In nature, healing is an intrinsic ability diverse from plants to animal kingdoms, roughly classified into eight prevalent mechanisms: (i) reversible muscle control, (ii) clotting, (iii) cellular response, (iv) layering, (v) protective surfaces, (vi) vascular networks or capsules, (vii) exposure, and (viii) replenishable functional coatings[410] by the biological community. **Table 7** summarizes the healing in nature (*flora* and *fauna*) through an organizational approach. *Flora* includes *herbaceous plants* that die down to ground and regrow each year (*i.e.,* annuals, biennials, and perennials) and *woody plants* referring to trees that maintain a persistent woody stem above ground year-round; *fauna* includes *vertebrates* (animals with a spinal cord) and *invertebrates* (without spinal cord). Due to the huge variability of species, their specific self-healing mechanisms differ significantly. For example, **Figure 24a** shows the wound healing in a tree limb, where the cells at the wound (cut) are hardening to seal off the wound to prevent the exposure to harmful microbes. Some plants also have special secretion cells (or the vascularized networks throughout their tissues), which could release latex, gum or volatile oils at the cut to heal injuries and/or to repel predators.[411,412] **Figure 24b** shows a latex producing tree as an example, which has inspired the application of 'self-healing elastomers for dampers'[413–417]. In *vertebrates*, bone remodeling *via* a complex series of cellular and humoral activities are important to the species.[418] **Figure 24c** shows this process, which begins with the debris cleaning at the existing bone fracture by the *osteoclasts* (cells that breaks down bone tissue), followed by remodeling by pre-osteoblasts to wound the site, reproducing of extracellular matrix and mineralization to produce new bone. During the process, continuous 'precursor' supply of *Hematopoietic* and *Mesenchymal* stem cell is crucial to this 'synthetic reaction'. This concept has inspired 'self-sealing and self-healing concrete'[419]. As a broad overview, **Table 8** lists a chronological overview of some self-healing/repairing materials/applications inspired by nature according to prior literature.

In terms of perovskite, one challenge in this material is its high chemical activity with oxygen and moisture in air. Placing a halide perovskite thin film in the ambient atmosphere will introduce a gradual surface degradation (chemical impurities, surface trap, etc.) that is harmful for their use in PSCs.[420,421] Removing these already degraded surface layer inspired by the ecdysis and moulting of animals (**Figure 24d**) could be a potential solution. In fact, the concept of 'surface layer removal to obtain a high-quality fresh layer' has been widely used chemically and physically in manufacturing (e.g., surface cleaning of monocrystalline silicon wafer for chip manufacturing)[422] and in research (e.g., mechanically exfoliation of 2D materials for obtaining a fresh surface[423,424]). For a perovskite crystal, the surface trap has significant harmful impacts on the interfacial contact. **Figure 24e** shows a cross-sectional SEM image of a perovskite crystal with poor surface morphology. Properly polishing the top surface with techniques such as laser polishing or other fine lapping may help to passivate those unwanted surface defects. To prevent surface degradation of halide perovskite film, an alternative pathway could be a quick surface passivation before reaction with air. Like the wound sealing process at the epidermis in soft tissues of the *invertebrate*, covering the reactive surface with a clotting-like ultrathin layer may be helpful in inhibiting the reaction with ambient harmful agents. This spontaneous self-surface-protection could be conceptualized either by introducing specific additives in perovskite that can spontaneously form a robust top protecting layer on the halide perovskite[425] (will be discussed in **5.3 Bio-additive** section) or intentionally coating a capping layer on top of the wet halide perovskite film before its reaction with air.[426] Protective skin or an outer shell are widely used strategies in nature. **Figure 24f** shows the examples of cell walls of plants that can protect the cell, skin epidermis that can protect the inner tissues, exoskeleton of insects that can provide protection against harsh environmental stimuli, and marine collagens that can protect marine organisms. In comparison, for perovskite solar cells research, different protection strategies have been proposed (**Figure 24f**). For example, a core-shell structure could protect the core perovskite lattice, an ultrathin organic coating layer on the grain could protect the crystal grain of perovskite, and a 2D capping layer could protect the 3D perovskite layer underneath. This is particularly important for perovskite solar cells, where the surface traps account for a significant loss. Especially in single-crystalline perovskite solar cell, since the inner bulk

region is having no boundaries, the surface trap could lead to a serious issue in contact with CTL or electrodes. Passivating those surface traps or delaminating the top-rough 'skin' to induce a smooth inner surface during device assembly is the next hurdle to overcome. This may require sophisticated manufacturing techniques such as laser-annealing, laser polishing and flashing lamp annealing techniques.

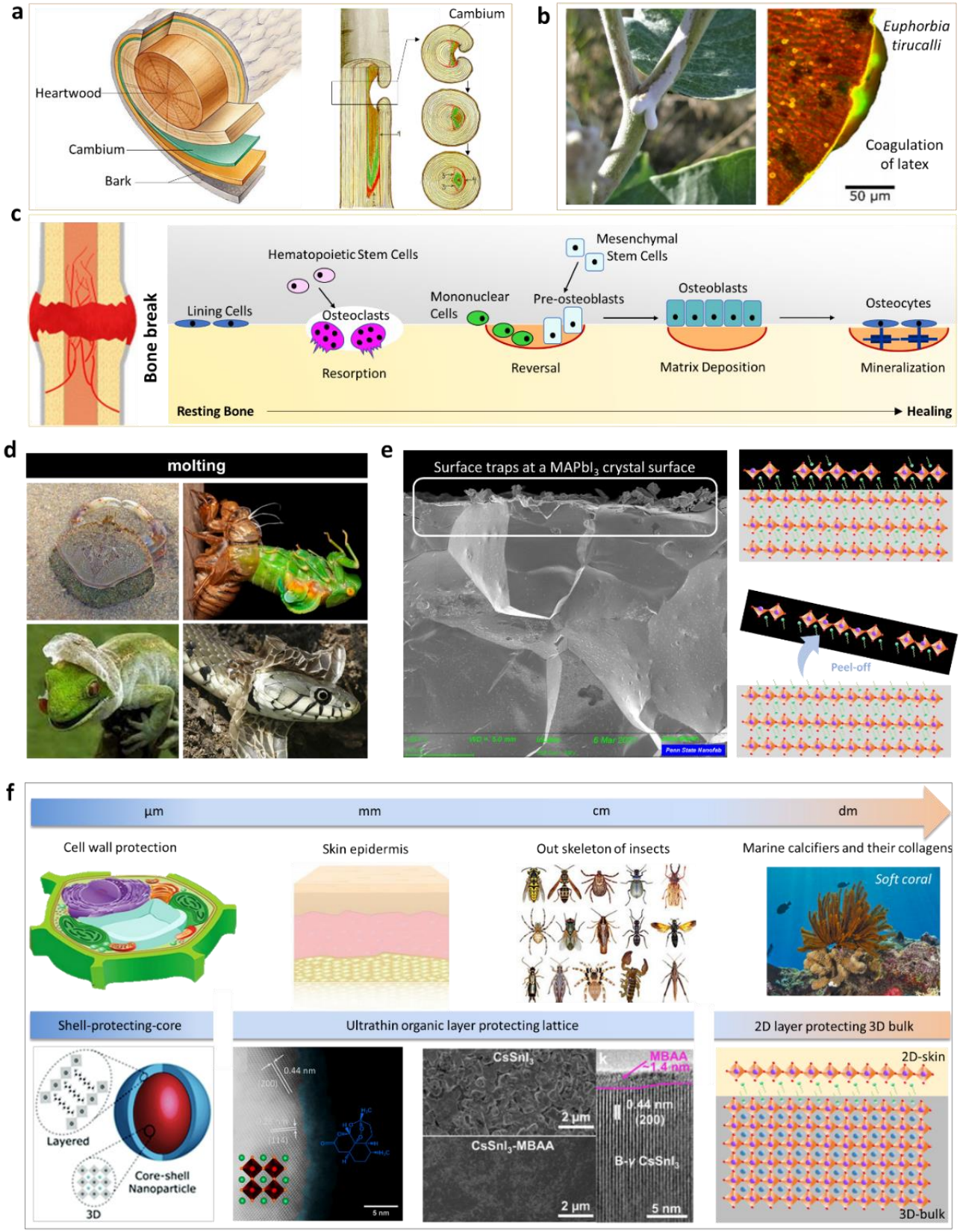

Figure 24 Natural examples of self-healing. (a) & (b): Several self-healing and defence mechanism in in herbaceous and woody: **(a)** Wound closure and growth **(b)** Secretion cells, adapted with permission from Ref. [460,492–494], Copyright 2005 Nature Publishing Group. **(c)** Schematic illustration showing the healing process in vertebrate hard tissue, adapted with permission from Ref. [495], Copyright 2011 Springer Nature. **(d)** (i) Photography showing the ecdysis/molting behavior of various animals, credits to multiple online sources [496–498]. **(e)** SEM image showing the poor and defective surface of a $MAPbI_3$ crystal. Mechanically exfoliation of top layers for obtaining a fresh surface is a commonly used method in material researches. **(f)** Schematic illustration showing the protection mechanism in species at different length scale: cell wall protects the cell of plant, skin epidermis protects the inner tissues, out skeleton of insects provides protection against harsh environmental stimuli, and marine collagens protects the marine creatures. In comparison, in the research of perovskite solar cells, different protection strategies have been proposed: a core-shell structure protects the core lattice, an ultrathin organic coating layer on the grain could protect the core crystal of perovskite, a 2D capping layer can protect the 3D bulk layer underneath. Pictures are adapted with permission from online resources [497,499] and from Ref. [475,500,501], Copyright 2020 Elsevier, 2016 The Royal Society of Chemistry, and 2021 American Chemical Society

5.2.2 Self-healing in PSCs

PSCs targeted for MPS applications may have soft and deformable attributes. However, soft elastic materials typically used for PSCs and other electronics are susceptible to puncturing and tearing, leading to mechanical failures, performance losses, and even the lead leakage from the perovskite layer. This potential failure greatly limits the use of MPS in applications such as autonomous field robotics or remote mission (e.g., spatial mission) where repairs are challenging or even impossible. Hence, soft MPS which are self-healable and functionally repairable, like natural skin or nervous tissue, are of great interest. In a higher-level field view of artificial self-healing materials, many nature-inspired mechanisms and materials have been proposed. These include semiconducting polymeric networks,[427–429] recoverable polymers,[430] ionic hydrogels,[431] liquid metal (LM) microfluidics,[432,433] and LM microcapsules patterned on solid lines[434]. These methods can also be transferred to be used into PSCs. At this point, self-healing in PSCs still is not fully developed. For specific consideration of halide perovskite, some aspects of this material are serious issues for

Table 8 chronological overview of some self-healing/repairing materials/applications inspired by the nature.

First Published in Year	Inspired by	Self-Repair in Biological Role Models	Self-Repair Mechanism	Bioinspired or Biomimetic Materials Learned from Nature	Bioinspiration or Biomimetic Approach	Key References
2010		Waxy surfaces of plant (Lotus)	Super-hydrophobicity by regenerating the eicular wax layer	Self-healing superhydrophobic coatings	Top-down approach or problem-driven BID	457
2010		Latex-bearing plants	Latex discharge and latex coagulation	Self-healing elastomers for dampers	Top-down approach	428–430,432,458
2011		Nepenthes pitcher plants	Liquid-repellent microtextured surfaces with a stable air-liquid interface	Self-healing, slippery, liquid-infused porous surface(s)	Top-down approach or problem-driven BID	434
2011	Plants	Stems of twining liana	Sealing cells squeezing into tissue fissures	Self-healing closed cell polyurethane foam coating for pneumatic systems	Top-down approach	459–464
2016		Surface of plant leaves (Lotus) and Nepenthes pitcher plants	Wax repair of leaves and slippery surfaces of pitfall traps	Self-repairing slippery liquid-infused porous surfaces	Top-down approach or problem-driven BID	465
2018		Follicles of the plant genus Banksia	Waxes at the suture of the two valves protecting the seed seal up microfissures	Wood platelets sealed by carnauba	Top-down approach or problem-driven BID	466,467
2018		Leaves of D. cooperi	Release of stored elastic energy	Phase-separated polymers with built-in shape-memory effect leading to self-healing	Bottom-up approach	468–471

2013		Byssal threads of marine mussels	Metal coordination-based cross-linking of proteins	Self-healing, multi-pH-responsive hydrogel	Top-down approach or problem-driven BID	472–475
2014	Animals	Byssal threads of marine mussels	Self-assembly	Wet self-mending polymers, surface-functionalized with catechol	Top-down approach or problem-driven BID	476
2015		Architecture of nacre	Self-assembly	Self-healing polymers with high dynamics	Bioinspiration	477
2016		Architecture of nacre	Sacrificial bonds in organic layer	Autonomous self-healing layers of supermolecular polymer	Bioinspiration	478
2017		Architecture of nacre	Hierarchical structure	Heat-triggered composites releasing sealant	Bioinspiration	479
2005		Hemostasis and bone healing	Delivery and reaction of healing agents	"Bleeding composites" for aerospace applications	Top-down approach or problem-driven BID	480–485
2013	Humans	Hemostasis of spongious bone	Delivery and reaction of healing agents in a porous concrete core	Self-sealing and self-healing concrete	Top-down approach	486
2018		Epidermis of human skin	Hierarchically stratified structure of a soft inner and a hard-outer material layer	Hierarchical coating system of hybrid multilayers with synergetic self-healing function	Top-down approach or problem-driven BID	487
2015	Living creature in general	Living tissues with self-regulated release systems of liquid	Continuous, dynamic, liquid exchange between shell-less droplets, matrix and surface	Self-healing droplet-embedded gel material	Bioinspiration	488

industrial implementation, including the environmental impact from the lead[435–437] as well as the materials' photo- and chemical-stability.[438–440] The material is intrinsically metastable with significant anharmonicity in the chemical bonds and consequent dynamic disordered states within the crystallographic lattice.[441] Restoring the properties from a 'damaged' state of halide perovskite to its original 'healthy' state to prevent device failure is of great importance. As an organic-inorganic hybrid material with a 'soft' attribute (much smaller Young's Modulus than that of typical inorganic semiconductors such as Si and GaAs), it is possible to heal the perovskite using the aforementioned methods applied in other 'soft' materials such as polymers. For example, using chemical/physical treatments (e.g., exposure to degrading chemical, thermal, or light treatments) on halide perovskite,[442,443] cracks and pin-holes can be merged well. Early studies have revealed that the incorporation of polyethylene glycol (PEG) additives to $MAPbI_3$ perovskite can revert the degraded crystal (yellow δ-phase) back to the black β-phase.[444] Specifically as shown in **Figure 25a(i)**, by infiltrating the perovskite into a PEG scaffold, the composite film exhibits a recovery behavior after degradation upon water spray, which otherwise would display an irreversible degradation if no PEG was involved. By constructing the PEG scaffold-based PSC (**Figure 25a(ii)**), a self-healing device performance has also obtained. The PCE decays with a reduced V_{OC} and J_{SC} upon exposure to water vapour but then returns back to its original number in less than one minute (**Figure 25a(iii)**). This self-healing phenomenon might originate from the excellent hygroscopicity of the PEG coupled by their strong interaction with perovskite lattice terminals. PEG has stronger interactions with water molecules than those of perovskite and water, so the water can be retained in the PEG phase instead of diffusing into the perovskite phase; PEG can also keep the MAI (through hydrogen interaction) from escaping away through a higher volume of water spray. By putting back into a dry atmosphere, as long as the retained water molecules evaporates, the non-perovskite yellowish phase turned back to the black β-phase. Similar to polymers, small organics with proper interactions with perovskite lattice can also assist the self-healing of PSC. Recently, Ran et al. reported the incorporation of large-volume amines (LVAs) in the Sn-based PSC with a self-healing property. After heating or exposing to air (Sn-based PSC is highly sensitive to heat and oxygen due to the quick oxidation of Sn^{2+} in $FASnI_3$), the LVA-based device could partially restore its PCE from 60% of its initial value to 80% after being placed in N_2 atmosphere for a specific time. This self-healing effect might be due to the steric hindrance effect of the LVAs.[445]

Similar 'self-healing' effects in PSC upon exposure and termination of proton radiation have also been observed.[446] This might be more important for outer space and space ship mission

applications. The proton (p) radiation, together with helium (He) (resulting from galactic cosmic radiation or solar flares, with a particle flux of 10^3 to 10^8 cm^{-2} s^{-1} depending on the distance from Earth)[447–449], are the major cosmic radiation sources for the solar cells and MPS used in spatial missions (e.g., spaceships and satellites in outer space). Protons with high energies (close to 1 MeV) can induce ionization and lattice displacement, and result in device damage to solar cells.[450] Lang et al.[446] found that the PSC exhibited compromised PCE upon proton irradiation but displayed a self-healing effect by returning the PCE to its original value after terminating the radiation (**Figure 25b(i)**). This can be understood by the proton irradiation-induced displacement of hydrogen. The proton irradiation typically results in the chemical bond breakage of C–H and N–H,

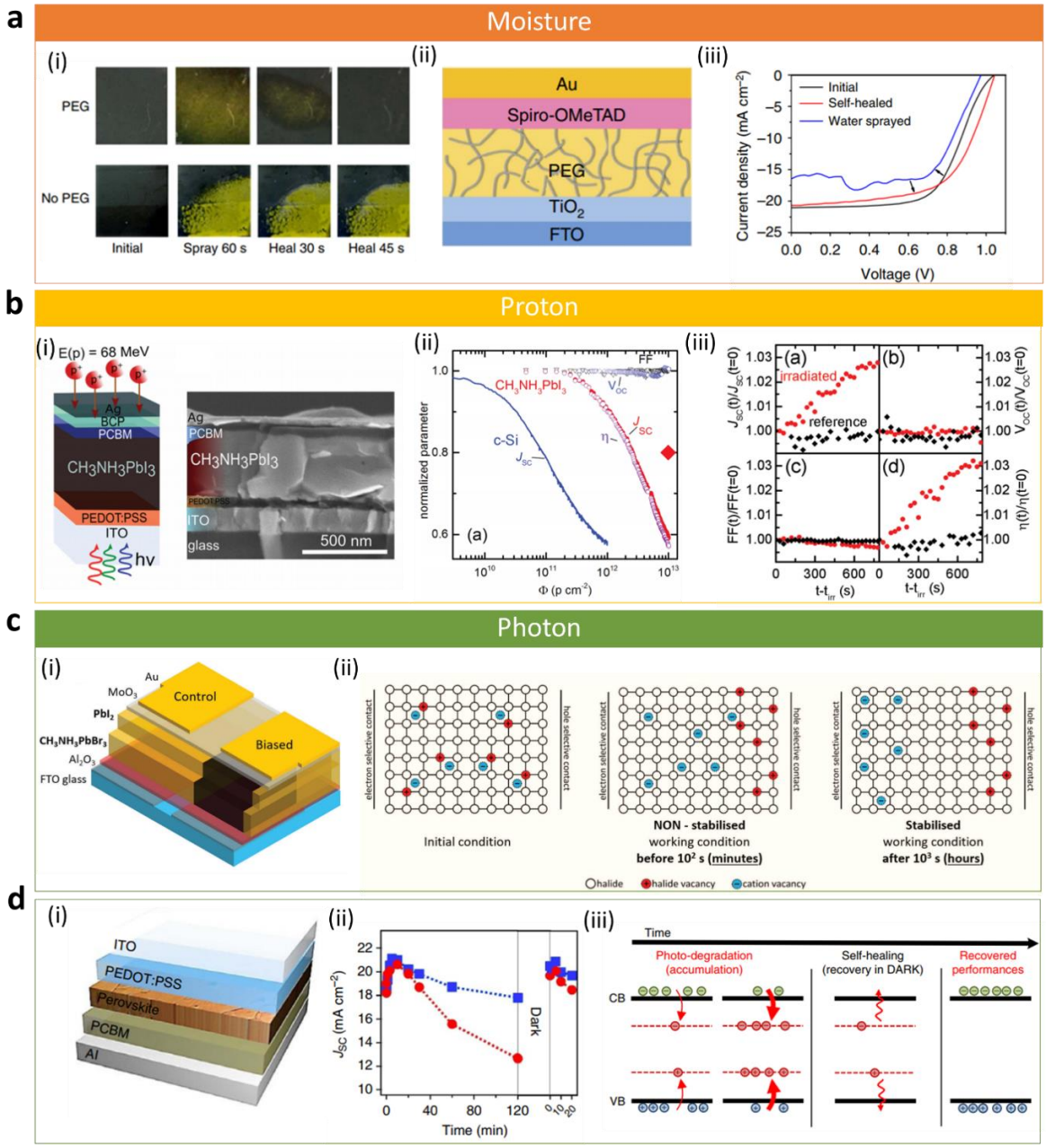

Figure 25 Self-healing perovskite solar cell against environmental degradation. (a) (i) Photographs of perovskite films with and without PEG showing color change evolution after water-spraying. (ii) Schematic illustration of the PEG scaffold structured perovskite solar cell (PPSC). (iii) J-V curves of PPSC before and after water spray showing the self-healing feature, adapted with permission from Ref.[551], Copyright 2016 Springer. **(b)** (i) Schematic illustration and cross-sectional SEM image showing an invert-structured perovskite solar cell. (ii) Normalized solar-cell parameters (V_{OC}, J_{SC}, FF) as a function of the proton dose, ϕ. (iii) Time dependence of the normalized solar-cell parameters after termination of the proton irradiation for a proton-irradiated device (red circles) and for a reference solar cell (black dot), adapted with permission from Ref.[553], Copyright 2016 Wiley-VCH Verlag GmbH & Co. KGaA. **(c)** (i) Schematic illustration for the biasing experiment. (ii) Schematics of the evolution of the ion distribution within the perovskite layer under solar cell working conditions, adapted wither permission from Ref.[561], Copyright 2017 The Royal Society of Chemistry. **(d)** (i) Schematic illustration of the planar structured perovskite solar cell device. (ii) Time evolution of J_{SC} under constant illumination and after resting the device in dark. (iii) Schematics of the proposed photocurrent degradation and self-healing mechanism, adapted with permission from Ref.[558], Copyright 2016 Springer.

rendering localized in-band states (further leading to Shockley-Read-Hall (SRH) recombination) (**Figure 25b(ii)**). After termination of the proton irradiation, the displaced hydrogen atoms migrate back towards the lattice and passivate the localized defects, recovering back to its original state. This self-healing process is verified in the recovery of the photocurrent (**Figure 25b(iii)**).

Besides above moisture and proton radiation stimulated self-healing, another type of healing is via illumination.[451] Several groups have reported such a photo-induced degradation and recovery of the device PV parameters under constant solar irradiation, applied external bias and storage in dark. In early 2015, Bag et al.[452] reported the first observation of photoinduced quasi-reversibility of PSCs ($MA_xFA_{1-x}PbI_3$) performance. The PSC degradation under sunlight contains both thermally activated fast ion transport and lattice-expansion, triggered by IR light in the solar spectrum. Interestingly, they also observed that after keeping a previously illuminated $MAPbI_3$ PSC in dark for 15 min, the lost PCE of the device can be recovered when re-illuminated. Similarly, Yadav et al.[453] also found that under conditions of illumination and bias, the J_{SC} of PSC decreased in a reversible pathway and recovered to its initial number after being kept in dark for a short time. The ion movement and accumulation, and the resultant interfacial change at selective contacts is concluded to be a possible mechanism restricting the PV performance recovery.[453] These ion-migration induced recoverable PCE changes in PSC have been further supported by the work from Domanski et al.[454] (**Figure 25c**). By *in-situ* cooling the working PSCs and exemption of thermally induced non-reversible PCE loss, the device exhibits a significant PCE loss under continuous operation (in light) and then shows a PCE recovery to its initial value after resting in dark. As shown in **Figure 25c(ii)**, at the initial condition, the ionic pairs (stoichiometric anion and cation) are randomly distributed in the perovskite layer; at the non-stabilized condition (devices are exposed to light and biased to MPP) anions (vacancies) migrate to HTL side and form a Debye layer at the interface, leaving the relatively immobile cation behind; at the longer timescales over 10^3 s (i.e., the stabilized condition), cations migrate and form another Debye layer at ETL sides. Both Debye layers at HTL and ETL sides are harmful for photocarrier extraction and hence lead to a PCE degradation, but can be recoverable. Particularly when the PSC device is given several hours 'resting' in the dark, the ionic distribution can thermodynamically return to its initial random state and thereby the device appears to be 'fresh' again and thus PCE is restored. Supported by modelling and elemental depth profiling results, the slow ionic migration (timescale $>10^3$ s) induced reversible PCE losses is further verified. Based on this timescale of $>10^3$ s, the natural day/night cycles (timescale of 10^4 s) can provide enough time for self-healing the device performance spontaneously. Similar recoverable behaviour of PSC was also observed by Lee et al.[455] After being exposed to 365 nm UV light for >1,000 hrs. under inert gas (<0.5 ppm H_2O) followed by one-sun soaking (allowing dispatching of stacked charges and neutralization of defects), the PSC showed the PCE recovery. In parallel, a claim of 'light-activated metastable trap-states'[451] to explain the recovery behaviour of PSC is also documented. Nie et al.[451] demonstrated that PSC degradation under constant solar illumination is due to the photocurrent loss, which can quickly self-heal within 1 min in dark to its original value (**Figure 25d(ii)**). PSC capacitance measurements and film time-resolved (TR) PL spectroscopy attribute the observed photocurrent loss to the 'light-activated metastable trap-states'[451] (**Figure 25(iii)**), which further leads to the space charges at the interface (resulting in non-homogeneous electric fields interfering with charge transport in the device) as supported by both experimental data and DFT analysis. Overall, in PSCs there have been several interesting phenomena observed for 'self-healing': (i) two distinct time regimes of recovery: fast recovery (i.e., <1 min,[451] retrieving ~96% of its initial PCE), slower recovery (tens of minutes to an hour, i.e., 10^3 s,[454] fully restoring the photocurrent); (ii) the photocurrent degradation can be attributed to the formation of light-activated, metastable and deep trap-states (>0.5 eV)[451]; (iii) both the degradation and self-healing of PSC are highly sensitive to temperature and light,[452] the former's dynamic (timescale of 10^3 s) is slower than latter's (timescale of 10^2 s); (iv) V_{OC} decrease by 40 mV has been observed and is due to the deep trap-states. To explain these behaviours, a more general and fundamental property of perovskite material needs to be clarified, the 'polaron' model.[456] The formation of small polarons are generally responsible for these experimental 'self-healing' behaviour in PSCs, based on the following considerations: (i) localized polaronic states can be manifested as deep trap-states in the forbidden band, which further gives rise to the space charge accumulation and a ≤40% photocurrent reduction; (ii) formation time of small polarons is faster than the time scales of PSC degradation; (iii) slow degradation of the photocurrent can be attributed to the accumulation of small polarons. Bearing these, Nan et al.[457] provided a first-principles calculation on the light-induced photocurrent degradation and self-healing in $MAPbI_3$ PSCs. It is demonstrated that under photoexcitation, changes of crystallographic lattice (due to photo-activation of site vacancies followed by a geometric relaxation) leads to the formation of partial localized excitons being trapped at the defects. In the meantime, the other excitons can be dissociated into free charges at the femtosecond scale due to their very small exciton binding energy.[458,459] Hence there is the coexistence of trapped excitons and free charges. The trapped excitons can be released (to yield a recovery effect) with an activation energy of 26 meV for the I-site vacancy and 38 meV for the Pb-site vacancy in $MAPbI_3$. Overall, the photocurrent degradation and recovery in PSC can be determined by the competition between the trapping and releasing of excitons. This mechanism is more general and can be applied for similar perovskites such as $FAPbI_3$, $MAPbBr_3$, and $FAPbBr_3$, but with a faster recovery dynamic.[456] The optical 'damage' to the perovskite film has also been investigated and found in the recovery of PL of multiple perovskite films.[456,460] Such observations indicate that illumination induced 'damage' of perovskite can be repaired continuously.

Outside of the self-healing of the perovskite crystals, another consideration can be the quarantine of leakage of the toxic lead

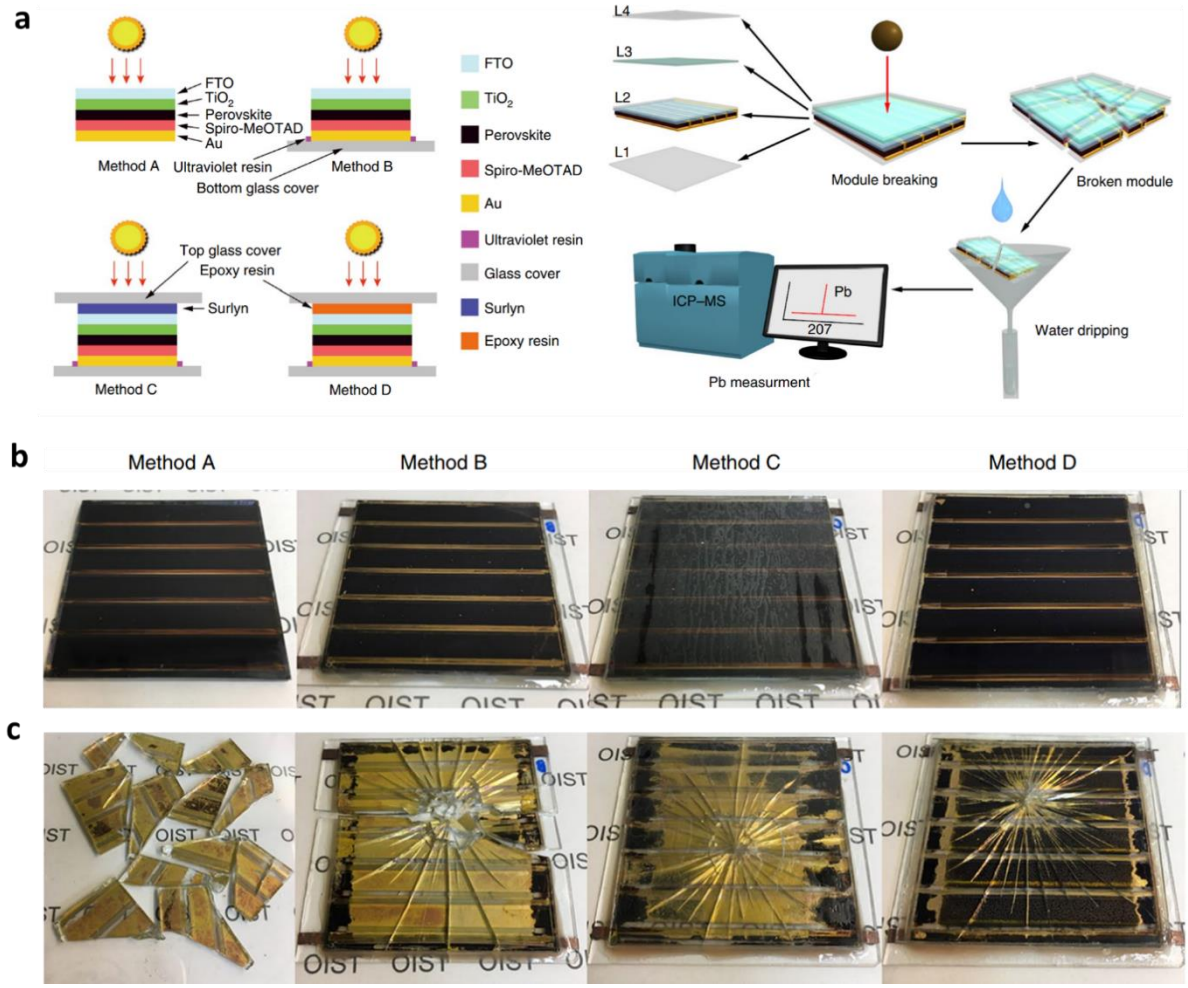

Figure 26 Self-quarantine strategies in PSCs. (a) Schematic illustration showing the different encapsulation methods (left) and the experimental procedure to assess the quantity of the toxic Pb leaked from a perovskite solar module that is damaged due to an external impact (for example, hail) (right). **(b)** and **(c)**: Perovskite solar modules using different encapsulation methods (b) before and (c) after impact and water dripping test, adapted with permission from Ref. [568], Copyright 2019 Springer.

by some self-healing encapsulation materials when the PSC is mechanically damaged. Recently, Jiang et al.[461] reported a self-healing polymer-based encapsulation to reduce the lead leakage from damage. Three encapsulation methods (**Figure 26a**) have been investigated coupled with a realistic simulated mechanical damage (to simulate the real hail impact) as well as Pb leakage rate. The crucial factor to minimize the Pb leakage is the self-repair ability of encapsulating polymers. **Figures 26b&c** compare the different encapsulation methods in terms of their effectiveness in limiting the lead leakage. **Figure 26b** shows the photographs of PSC modules with different encapsulation methods before impact and **Figure 26c** shows the photographs of these PSC modules after mechanical impacts (followed by two water dripping tests, the first by heating at 45 °C, and a second water dripping test). Different encapsulation methods yield various degrees of perovskite decomposition. Particularly, an epoxy resin (ER)-based polymer with a T_g of ~42 °C, when sandwiched between a PSC module and a top capping glass, can effectively reduce the rate of Pb leakage from 30 to 0.08 mg h^{-1} m^{-2} under various simulated weather conditions. Taking advantages of such 'self-healing' attributes from the polymeric encapsulation materials to protect the device, quarantine the lead, and even recover the partial performance loss is a promising pathway to extend the lifecycle of PSC based MPS products. On a broader scale beyond the epoxy resin, self-healing polymers involving various chemical processes (including incorporation of covalent,[462–464] free-radical,[465,466] supramolecular[467–469] dynamic bonds) and physical events (such as employing enhanced van der Waals interactions,[470] interdigitated copolymeric morphologies - embedded, reactive, encapsulated fluids that can infiltrate into a wound and trigger sequential chemical reactions for damage repairing[471] and cardiovascular networks[472]) are providing new insights. Although artificial self-healing in versatile systems may contain complex mechanisms, self-healing in living systems involves complex cascade reaction series, the exact chemistries of some of which are far from understood. Resembling these natural self-healing processes from learning and mimicking the reactions at a molecular scale is the major ongoing task in the

community of artificial self-healing materials. Learning, transferring, and applying these techniques into the more specialized PSC field may create a big leap to self-healable MPS products.

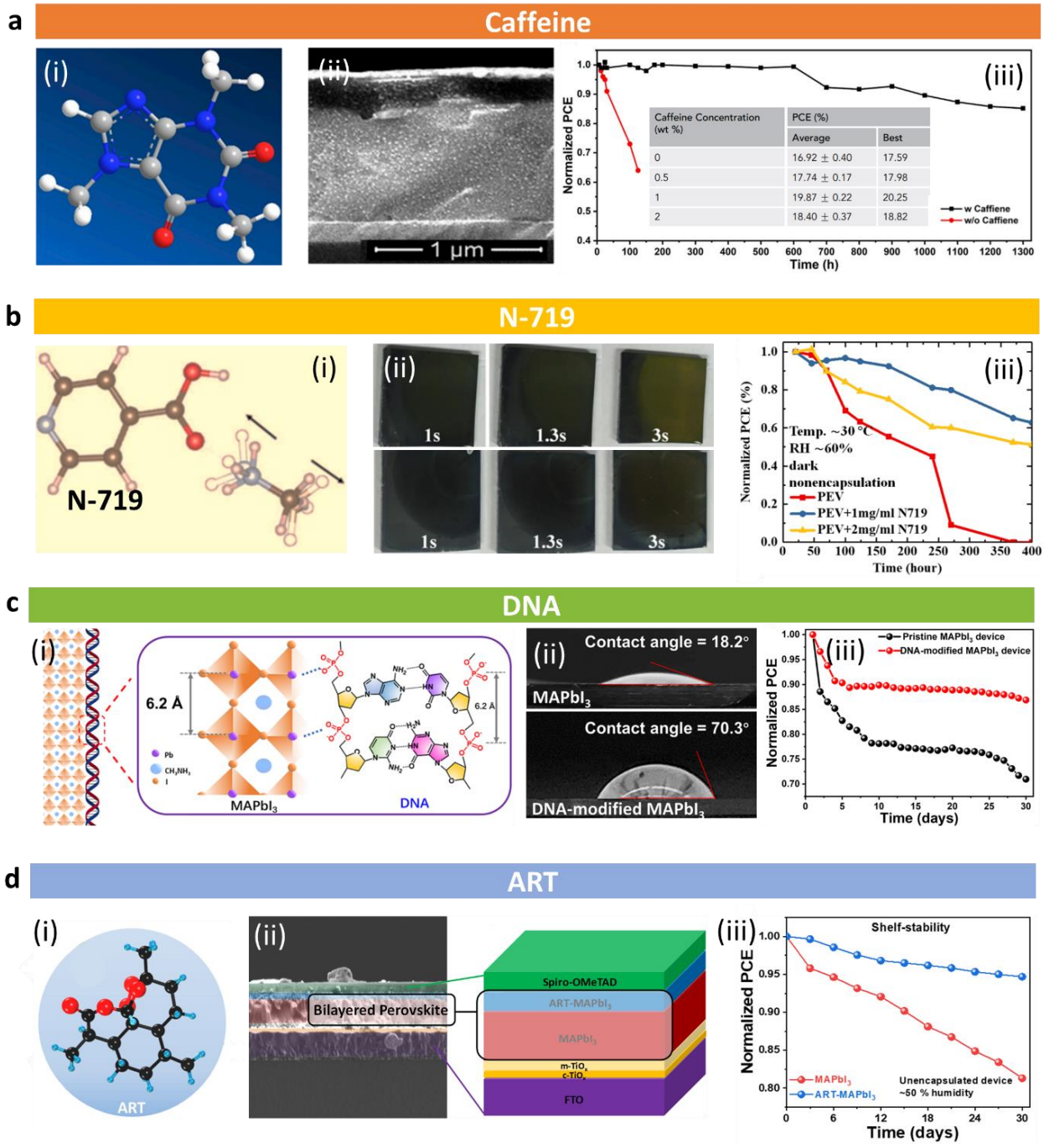

Figure 27 Bio-additives in perovskite solar cells. (a) (i) Molecular structure of Caffeine. (ii) Cross-sectional SEM image of the perovskite solar cell. (iii) Thermal stability test under 85℃ continuous annealing and photovoltaic performance of the Caffeine-incorporated solar cell, adapted with permission from Ref. [585], Copyright 2019 Elsevier. **(b)** Schematic illustration showing the interaction between MA^+ and N-719. (ii) Photography showing the degradation transformation process of perovskite film with and without N-719 additive. (iii) Stability test of perovskite solar cell under 60 % relative humidity condition, adapted with permission from Ref. [586], Copyright 2019 WILEY-VCH Verlag GmbH & Co. KGaA, Weinheim. **(c)** (i) Schematic illustration showing the interaction between DNA and perovskite. (ii) Contact angle of water droplet on the pristine and DNA-modified perovskite. (iii) Stability test of perovskite solar cell with and without DNA modification under relative humidity of 75%, adapted with permission from Ref. [275], Copyright 2019 American Chemical Society. **(d)** (i) Molecular structure of *Artemisinin* (ART) (ii) Schematic and SEM cross-sectional image showing the bilayer-structured perovskite solar cell induced by ART. (iii) Stability test of pristine and ART-modified perovskite solar cell under relative humidity of 50 %, adapted with permission from Ref. [475], Copyright 2020 Elsevier.

5.3 Bio-additive

Incorporation of processing additives into the photoactive layer is a universally effective methodology to boost PV cell performance. In OPVs, small molecule additives can tune the micromorphology of the BHJ blend and hence tune multiple electronic properties;[267] in PSCs, additives have been reported to have multiple effects on the device performance. There are various types of additives including salts, molecules, polymers, and even nanoparticles,[39,473–475] with varied effects, including modulating crystalline features, stabilizing perovskite phase, adjusting energy-level alignment, enhancing operational stability, eliminating hysteresis, suppressing nonradiative recombination, etc.[476,477] In contrast to those inorganic additives, biomolecular additives may have additional functionalities through molecular interaction with the lattice of perovskite by their specific functional chemical groups. A good example is in the *caffeine*[478], which is the active substance in coffee. A recent work has revealed the effectiveness of incorporation of *caffeine* in boosting the stability of PSC. The *caffeine* molecule has two C=O groups (**Figure 27a(i)**) with lone pair electrons that could interact with the Pb^{2+} from the perovskite lattice through strong Coulombic coordination, serving as 'molecular interlock' between adjacent perovskite grains. Meanwhile, these molecules can serve as Lewis bases passivating the Lewis acid-type defects like undercoordinated Pb^{2+} in perovskites, hence reducing the trap density. This molecular interlock effect also suppresses the ion migration, yielding a superior stability for a PSC based on the *n-i-p* structure (**Figure 27a(ii)**) to retain 90% of the initial PCE after 1,700 hrs. when annealed at 85 °C (in contrast to 60% of the initial performance remaining from the reference blank device after 175 hrs. annealing, as shown in **Figure 27a(iii)**). Similarly, Zhang et al.[479] introduced N719 (a dye derived from *chlorophyll*) into $MAPbI_3$ perovskite crystal. The-COOH groups from N719 were found to form complexes with the MA^+ ($MA^+ = CH_3NH_3^+$) in the perovskite lattice (**Figure 27b(i)**), which modifies the diffusion of water molecule in the materials. Theoretical calculation shows a much higher migration barrier of water molecules in the N719-based perovskite. As a result, the water penetration into perovskite layer can be greatly inhibited (**Figure 27b(ii)**), and moisture stability of the device is significantly improved. Nearly 70% of PCE can be retained in a high RH of 60% for 400 hrs. (**Figure 27b(iii)**). Our group also revealed that the incorporation of hydrophobic DNA-CTMA into perovskite crystal can sufficiently improve the device stability[261] by nanoscopically wrapping the perovskite nanocrystals (**Figure 27c(i)**). The strong hydrophobicity of DNA-CTMA also enhances the non-wettability upon contact with water (**Figure 27c(ii)**) and thereby improves the device lifetime (**Figure 27c(iii)**). Recently, our group reported a 'perovskite/perovskite' bilayer structure. The bottom perovskite layer is a bulk layer with typical grain size of hundreds of nanometers while the top perovskite layer consists of perovskite-*Artemisinin* core-shell nanocrystals. This bilayer structure is spontaneously formed by adding the *Artemisinin* molecules (**Figure 27d(i)**), which has been known as a medicine molecule against *Malaria*.[425,480] *Artemisinin* has a unique endoperoxide ring that produces free radicals to damage proteins of parasites and thereby cure the disease.[481,482] The sesquiterpene lactones structure and alkyls make *Artemisinin* insoluble in water, showing a hydrophobic behavior.[478] As a result, the hydrophobicity from the

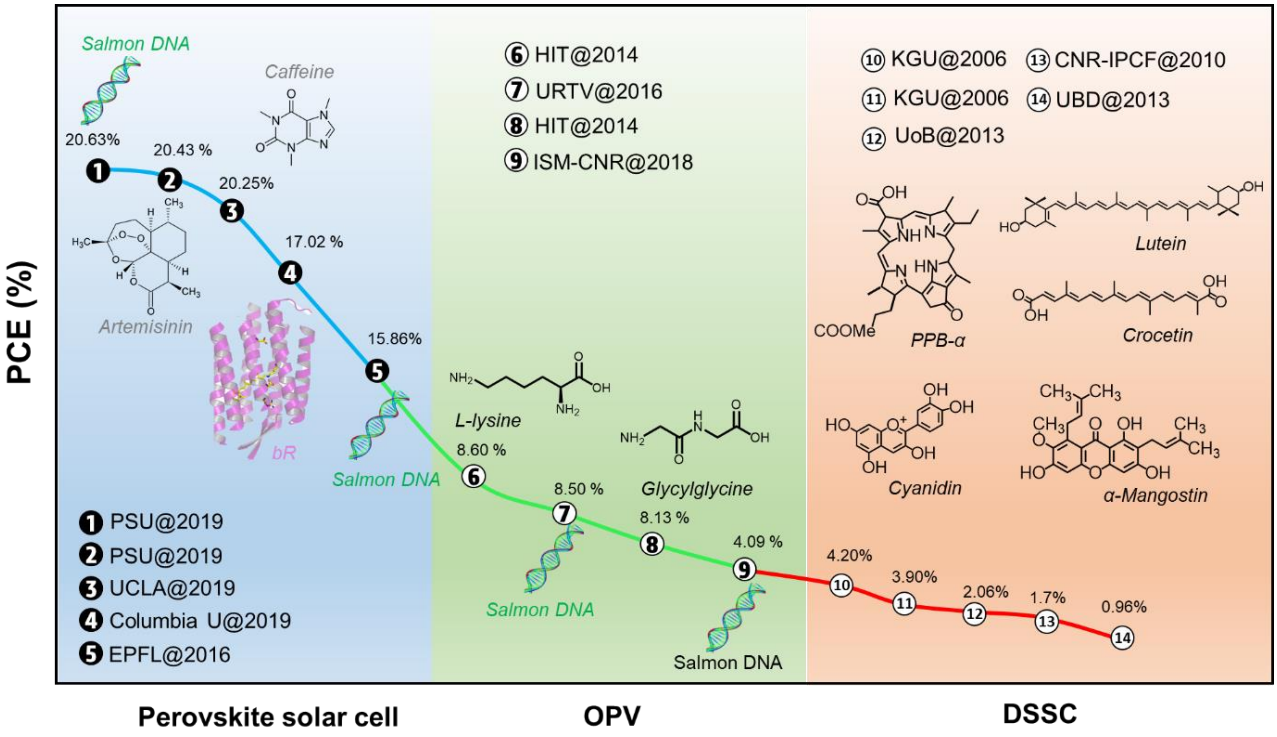

Figure 28 Summary of bio-additives in different class of photovoltaic devices: (1&2) Hou et al. Ref.[275] (3) Wang et al., Ref.[585] (4) Das et al., Ref.[322] (5) Yusoff et al., Ref.[274] (6) Deng et al., Ref.[590] (7) Dajar et al., Ref.[272] (8) Nie et al., Ref.[591] (9) Toschi et al., Ref.[591] (10&11) Wang et al., Ref.[398] (12) Henning et al., Ref.[592] (13) Calogero et al., Ref.[396] (14) Kumara et al., Ref.[593].

Artemisinin-incorporated $MAPbI_3$ top layer (**Figure 27d(ii)**) improves the device stability with a retained efficiency >18% which corresponds to ~95% of the initial PCE after one-month exposure in ambient environment (**Figure 27d(iii)**). Overall, by providing functional groups to anchor the terminal partially bonded atoms in perovskite lattice, the biomolecular additives are effective in improving the stability of the crystal. In addition, the PCE of the resultant PSCs can be improved in certain degrees mostly due to the enhanced crystalline quality. **Figure 28** summarizes the PCEs of PSCs incorporated with multiple bio-molecular additives. The highest PCE of 20.63% comes from a device structure of FTO/TiO_2/Perovskite/Spiro-MeOTAD/Au with the addition of DNA-CTMA into the perovskite layer. Nevertheless, biomolecules are naturally more complex than typically used artificial additives and their role in the cascade reaction series in a species can be even more complicated and delicate. Harnessing their specific chemical group as a functional agent to couple with those active terminal-atoms/crystallographic-sites in perovskite lattice might be a good way to improve performance, but it remains technically inefficient and scientifically unclear when using such complex molecules to execute simple redox chemical reactions between biomolecules and the perovskite lattice. Instead, simplifying the biomolecule structures, designing an optimal structure using the knowledgebase and knowhow from aforementioned successes, and utilizing a more functional-orientated bio-additives for PSC might be a better alternative.

5.4 Bio-hybrids

Extending from the scope of abovementioned nanoscale or molecular-scale-mixing of biomolecules and semiconductors, blending organisms with semiconductors at meso-scale is another research interest. Classic examples such as dye-sensitized solar cell where natural dyes are adsorbed at the surface of TiO_2 to execute the light-triggered biological processes across their interface, or the photo-bioelectrochemical cell and photobiofuel cell with biomolecules, cells or bacteria immobilized on the metal electrodes have been extensively studied for applications in energy harvesting, sensing and storage.[483–485] Particularly, similar to the photoactive layer of perovskite in perovskite solar cell, the photosynthetic proteins (*e.g.*, Reaction Centre – Light Harvesting 1 (RC-LH1)) from natural organisms such as Rhodobacter sphaeroides[486] plays the key role in natural photosynthesis reactions not only because of their similar role in photoexcitation of electrons to that of semiconductor but also their unique attributes such as ultrahigh quantum efficiency for energy transfer and charge separation as well as the maintenance of this high efficiency at low temperature as 4 K.[487,488] Recently, Tan et al.[487] took advantages of the wide response window of photosynthetic proteins upon light, temperatures, pressures, etc., and developed the self-powered all-weather sensory systems. By incorporating RC-LH1 into an electrolyte medium of a triblock copolymer (thermoreversible gel (TRG)), the photoelectrochemical cell even exhibited a self-healing behavior. This successful demonstration of photosynthetic proteins in solar-driven sensor applications revealed the underlying potential of natural photosynthetic proteins in innovating multifunctional solar devices.

Similarly, bacteriorhodopsin (bR) is another well-known photoactive protein usually found in the purple membrane of *Halobacterium salinarum*. In **Section 4.3**, we have discussed their role in charge transport layer in solar cells. Beyond the charge transport, in light of the enhanced potential for light-induced proton pumping and color switching, bR has also been adopted as platforms for various applications such as fuel cells, photodetectors, biosensors, artificial retinas, nanosensors, storage devices, holographic memory, security ink, and bio-defense or camouflage, which have been well documented in another review paper.[489]

Although not well studied so far, interfacing these relatively larger-size proteins with perovskite photoactive layer materials to render new composite could potentially extend the application domains of solar cells. For example, the low-temperature environment workable RC-LH1 could extend the solar cells' application to meet a critical environmental condition of extremely cold weather. Technically, employing these larger-size proteins in vitro in a perovskite polycrystalline layer still need to be properly strategized, where prior learnings from effective immobilization of proteins on electrode of photoelectrochemical device may be helpful. In parallel, fundamental research on the natural function of inner and intra the proteins and full understanding of the efficient transfer of photoinduced electrons across the interface are also necessary and important to guide us how to mimic it in real devices.

6. From Device to System Level

In above text, we have discussed the bio-inspired strategy for each individual component in the PSC device, including the electrode, charge transfer layer and the perovskite photoactive layer. Zooming out from these individual components towards the perspective at a device or system level, more intriguing and creative designs of the whole device system and their corresponding manufacturing inspired by the natural bio-systems are of great interest. In the following section, bio-inspired design with successful reported demonstrations at a whole device level and unconventional manufacturing techniques replicating the sophisticated nano-/microstructures from biology will be discussed.

6.1 Bio-inspired design

6.1.1 Solar tracker

Many living creatures can track the light adaptively to maximize their exposure to the light. Such a light-tracking phenomenon is known as *phototropism*, which can be found in the example of a sunflower that can self-orient itself to face the sun throughout the day. In these tropistic movement, organisms not only spatially 'sense' the light stimuli, but also spontaneously and continuously adjust their movements to strictly follow the incident light directions. This presents intelligence in self-regulation through

the natural feedback control inherent in dynamic interactions between the stimulus and the organisms. As the natural sunlight is dynamic (Earth rotating), there is an inevitable oblique-incidence energy-density loss (OEL, sunlight density reduction when the emissive energy projects on a surface obliquely, as shown in **Figure 29a**). The loss could be enormous if the incident angle is large (e.g., 75% loss at 75° incidence). In order to maintain the high-level light-reception, many plants developed such *phototropism* behavior. This *phototropism* could provide an efficient solution to address the universal OEL issue and huge energy loss in existing solar panel farm, although the solar trackers have been invented to reduce the OEL but mostly need additional power to supply their rotation (discuss latter). Harnessing such *phototrophic* behavior autonomously, without external controls or power supply, is of great significance in achieving highly efficient and intelligent PV systematic

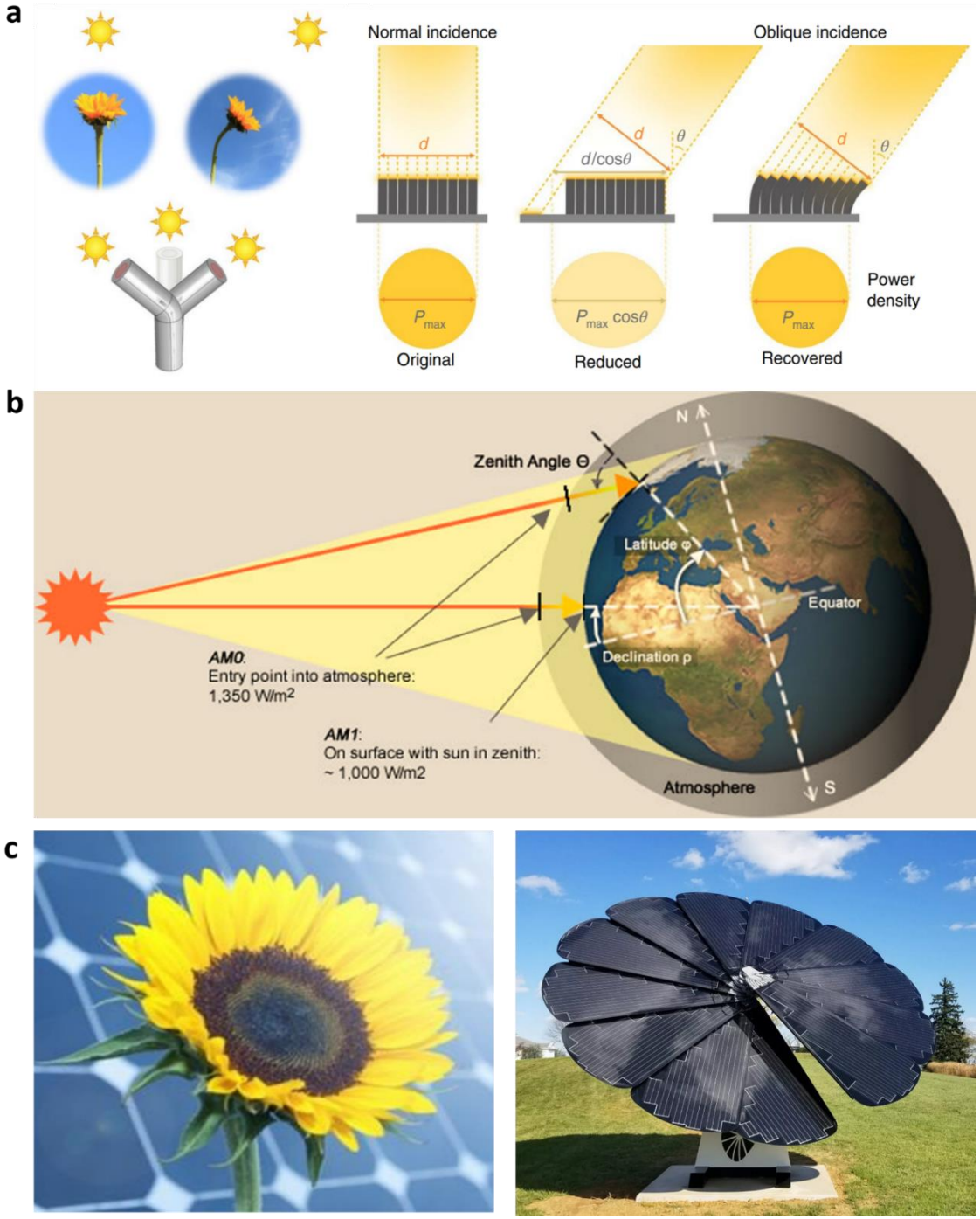

Figure 29 Solar tracking. (a) Schematic illustration showing concept of the artificial phototropism and the sunflower-like biomimetic omnidirectional tracker, adapted with permission from Ref.[605], Copyright 2019 Springer. **(b)** Schematic illustration of the solar hour angle which is controlled by the daily rotation of the earth, adapted from online resource.[619] **(c)** Photography of a sunflower (left), adapted from online resource,[620] and a sunflower-shaped solar panel (right), adapted from online resource.[621]

platforms with smart autonomous adaption to complex ambient environments (such as clouds and sunset). Although many reversibly photoresponsive soft materials such as hydrogels,[490–495] liquid crystal elastomers[496–498] and azobenzene/spiropyran-

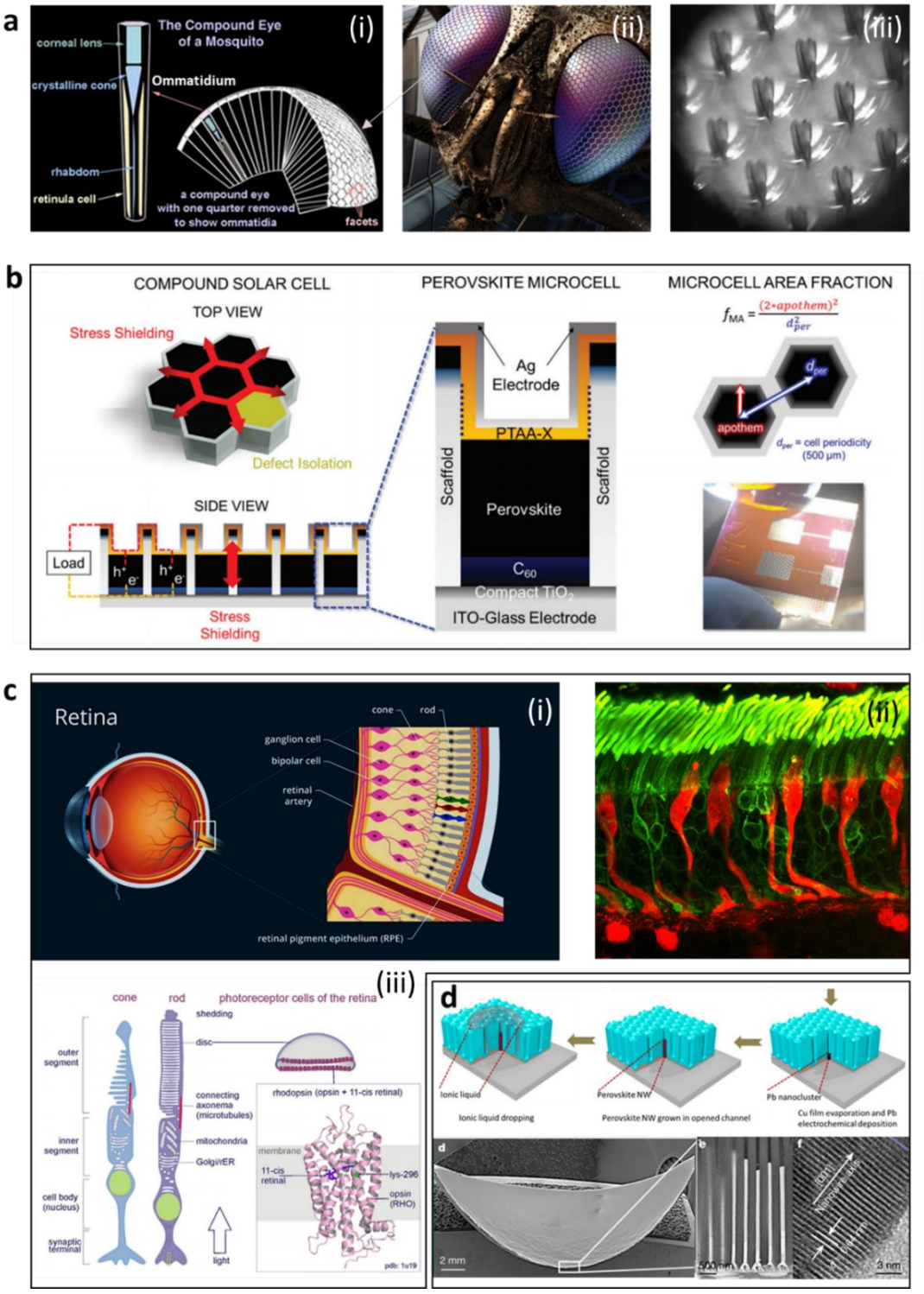

Figure 30 Scaffold for individual micro-cell. (a) (i) Structure of a compound eye, adapted from online resource.[624] (ii) Photography of the compound eye of a fly, adapted with permission from Ref. [429] (iii) Image of object formed in the compound eye, adapted from online resource.[625] **(b)** Schematic illustration of the "compound" perovskite solar cell design inspired by the compound eye concept, adapted with permission from Ref. [429], Copyright 2017 The Royal Society of Chemistry. **(c)** (i) Schematic illustration of human eye structure. (ii) Confocal microscope image of rod and cone photoreceptors in a human retina, adapted from online resource.[626] (iii) Illustration of structure of cone and rod photoreceptor in human retina, adapted with permission from Ref. [627], Copyright 2016 Elsevier. **(d)** Schematic illustration and microstructure of the artificial retina based on perovskite nano wire, which is mounted on a concavely hemispherical artificial eye, adapted with permission from Ref. [623], Copyright 2020 Springer.

based polymers[499,500] have been proposed as good candidates for achieving this artificial *phototropism* behavior,[501] while their applications in solar trackers of PV remains fully unexplored.

In the case of PV, output electrical power is heavily dependent on the solar irradiation that reaches the PV cell surface.[502,503] The more orthogonal the sunlight reaching the cell surface is, the higher the output power can be achieved. The Earth is constantly spinning and the incident angle of the Sun's rays on the cell surface is dynamically changing, causing significant power loss of the PV cell. In addition to the Earth's daily rotation, the annual rotation of the tilted Earth (**Figure 29b**), the latitude of the surface, and the local weather conditions will also affect the light absorption of PV cell. In order to expand the overall solar harvesting, the solar tracking technology inspired by the *phototropism* is a good solution. The state-of-the-art solar tracking techniques (**Figure 29c**) include the passive tracker (e.g., liquid or gas-based thermal expansion mechanism by the company, Zomewords,[504] researchers like Clifford et al.[505], Castañeda et al.[506]) and the active tracker (e.g., control logic and algorithm based mechanism, first presented by McFee[507], a control system with microprocessor and electric-optical sensor[508–513]). The former is advantageous as it has less energy/cost consumption of the tracking system, but it lacks intelligent reaction to the weather (as they are mostly thermally driven, hot weather will significantly interfere the tracking motion). The latter is advantageous in dynamically adapting the complex environmental condition, but requires additional power supply to maintain their response to environmental stimuli, algorithm to respond the temporally weather change and responding motion.

The ultimate way of harvesting the solar energy is to construct a sphere surrounding the light source. In a more Cosmoscopic level, efficiently utilizing the solar energy in the Solar System by future PV technology beyond the ongoing state-of-arts might be more exciting although unrealistic. For example, it could be a megastructure or the so-called '*Dyson sphere*'[514] conceived of as a gigantic shell of solar cells enclosing the sun and harvest 400 septillion watts of energy per second (a trillion times our current worldwide energy usage).

6.1.2 Scaffold for individual micro-cell

In real applications, the failure tolerance (property that enables a system to continue operating properly in the event of the failure of (or one or more faults within) some of its components) is an important index for the product. Particularly for PSC, the perovskite is highly sensitive to the ambient environment, making it easy to degrade under normal outdoor operation. As soon as one 'strip' cell in the PV module fails (e.g., may be due to small mechanical fracture, a small hole or even a microscale contact issue), the whole module may not work. While in nature, such issue can be avoided through design of features like an insect's compound eye (**Figure 30a**). The compound eyes are composed of many thousands (30 thousands in larger *Anisoptera dragonflies*) of *Facets* (or *Ommatidium*, hexagonal in cross-section and a large aspect ratio with ten times longer than wide) (**Figure 30a(i)**). Each *ommatidium* works as an individual photon sensor (as there is a cluster of photoreceptor cells at the inner wall of *ommatidium* which can convert the light signal into nerve pulse for reception by optical nerves). Hence, each *ommatidium* is innervated by one axon and thus providing the brain with one picture element. The brain forms an image from these independent picture elements. Such a design enables the independent work of *ommatidium* with exemption of the interreference from neighboring *ommatidium*. In other words, the failure of an *ommatidium* will not affect the normal function of neighboring *ommatidiums*. Using this concept, 'compound eye' PSC has been developed recently,[386] which contains individual cells being partitioned by a scaffold and arranged into a vast array of microcells with characteristics including a smaller size, encapsulation, and mechanical and chemical isolation. **Figure 30b** shows the design. The (gray) partitioning scaffold shields the individual perovskite microcells. The microcells (in the array) are connected in parallel by both the top and bottom electrode. The array has a pitch of 500 μm, which can be further modulated by adjusting the design of the scaffold substrates. As a result, thanks to the mechanical stress de-concentration, this 'compound' PSC displays a significantly enhanced fracture energy of ~13 J m^{-2} (30-fold increase over prior reported planar PSC with a number of ~0.4 J m^{-2}) with PCE over 15%. This design could also improve the failure tolerance since all the microcells are electrically connected in parallel, failure of any device is expected to not cause the failure of the whole device.

This individual array design for vision system prevails in nature, although the detailed mechanism in photon-sensing can be versatile. An analogous example is the retina's neurons that can recognize the light and convert it into neural signals. The retina is composed of three different layers of (i) outer nuclear layer (ONL, where the well-known cone and rod cells can sensor the light and convert it into neural signals), (ii) inner nuclear layer (INL, where the horizontal, bipolar, and amacrine cells can transmit neural signals from ONL to GCL), and (iii) ganglion cell layer (GCL, where the retinal ganglion cells can receive neural signals from INL and further transmit the action ionic potentials to the visual cortex through optic nerves) (**Figure 30c(i)**).[515] **Figure 30c(ii)** shows the picture of real cone cells (typically 40–50 μm long and 0.5 to 4.0 μm wide) and rod cells (typically 100 μm long and 2 μm wide). The most important part composing the rod and cone cells are the numerous membrane disks (**Figure 30c(iii)**) containing large numbers of photoreceptor proteins, *rhodopsin*. It is the *rhodopsin* that act as the visual pigment to convert the light into biochemical signal. As the *rhodopsin* photoreceptor proteins is inserted in the membrane, the disk-like packing of membrane can enhance the population of photoreceptor proteins and improve the light sensitivity. Such individually arrayed rod and cone layout perpendicularly inserted at the retina layer enables an efficient integration of a large quantity of individual cells, leading to a high visual resolution. Designing a retina-like photoactive array layer for PSC on a hemisphere substrate (**Figure 30d**) to panoramically harvest the light might be an alternative design to the dynamic solar tracker-system. One recent work on artificial retina conceptualized the perovskite nanorod (NR) array on a

concavely hemispherical artificial eye (field of view (FOV) of 150°–160°).[516] A hemispherical porous aluminum oxide membrane (PAM) was used as the template with numerous microchannel where the perovskite single crystalline NR can grow (**Figure 30d**).

Overall, many examples exist with a large potential for use of nature-inspired designs into novel structured PSCs. Shifting our attention from the focus on individual component such as each functional layer or material towards the whole device level design, system level implementation, temporal life-cycle and recycling, network overall planning with those power consumers and other power plant, could bring new insights to upgrade the device to the next level, which definitely will still need more knowledge and intelligence. These knowledgebases may have already been stored in the library of nature.

6.2 Bio-inspired manufacturing

Natural micro/nano- structures (including above discussed nacre, bone, Lotus leaves, insect's eye & wings, *etc.*) have provided enormous inspiration to many important applications. In addition to those research efforts devoted to further understanding the underlying mechanisms, there is a growing effort to manufacture artificial materials with those unprecedented properties *via* mimicking those found in nature. Focusing on superhydrophobicity and superhydrophilicity in nature as examples, Jiang *et al.* proposed the general procedure of designing and synthesizing related artificial materials:[517] (i) a unique property selection from the biological system (bio-target), (ii) an in-depth understanding of the correlation between the natural structure and their macroscopic properties, (iii) selection of the target artificial material, and (iv) construction of the

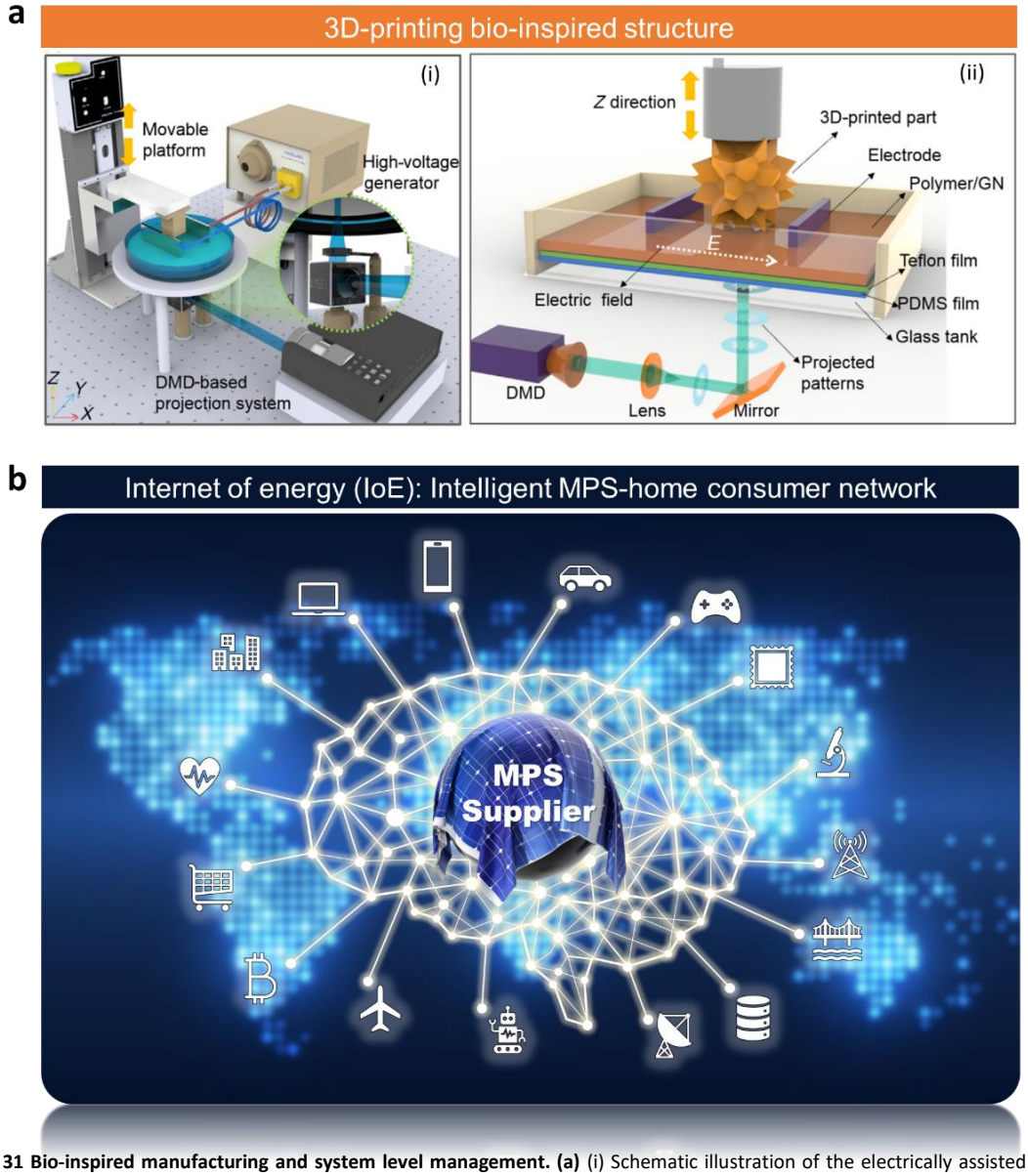

Figure 31 Bio-inspired manufacturing and system level management. (a) (i) Schematic illustration of the electrically assisted 3D-printing equipment (ii) Illustration of the bottom-up projection-based stereolithography process, adapted with permission from Ref.[651], Copyright 2019 AAAS. **(b)** Illustration of the concept internet of energy (IoE).

architecture to realize the aimed function. Nevertheless, the major challenge lies in techniques chosen to assemble the molecules at both nano- and microscales. So far, various strategies to synthesize functional materials that resemble natural species' architecture and function have been developed, including chemical vapor deposition (CVD),[518–521] self-assembly,[522–527] lithography,[528–534] and other 3D printing techniques.[535] Particularly, additive manufacturing (3D printing, exemplified in **Figure 31a**) has opened new opportunities for mimicking and manufacturing the intrinsic multi-scale, multi-material, and multi-functional structures found in nature.[536] Nevertheless, in contrast to most man-made materials, natural materials are built in much milder inner environments within the species' body which has ambient temperatures and aqueous environment. The 'manufacturing' of natural materials is more delicate and using bottom-up strategies in a tiny system, making them difficult to duplicate in large-scale artificial manufacturing.[537] Importantly, natural materials combining the desirable properties of their components usually perform significantly better than the sum of their parts (similar to the *emergent properties*) — a natural coupling effect that has inspired much of the ongoing interest in design of bioinspired materials. Many natural systems simply follow basic mathematical rules but turned out into sophisticated functionality (e.g., ant's route selection of emergency logistics algorithm)[538]. Exploring and learning the secrets from natural material and system offer a pathway towards solving manufacturing challenges that exist in the current PSC-based MPS. By using bio-inspiration, innovations may exist either in the individual manufacturing of the PSCs, or their integration with the MPS in a higher-level network incorporating both energy supplier and energy consumer for advanced internet of energy (IoE) system. Stream-line manufacturing with a continuous producing attribute could make the PSC fabrication in a highly efficient way, which will need to balance the conflicts between each individual component in the device and eventually unite them into a whole device with consistent functionality. Since the PSC consists of multiple components including bottom electrode (front contact), ETL, perovskite light absorber, HTL, and top electrode (back contact) as well as interfacial modification layers sometimes. Each component will need a specific individual manufacturing process to obtain its optimal performance, and this diversification in manufacturing processes will make it costly and time-consuming for the whole device fabrication. In comparison, streamlined manufacturing in conjunction with a joint consideration on both cost and performance of the whole device will need to minimize the conflict behaviors and maximize the reciprocal behaviors between each individual component. A natural prototype of this strategy could be the human gut microbial ecosystem (HGME) that consists of hundreds to thousands of species of bacteria, archaea, and eukarya as well as viruses.[539] In order to maintain a eubiotic state that promotes homeostasis of the whole bodily function, individual species in HGME (individual component in the system) could sacrifice in certain level to reduce conflicts and enhance the reciprocals to keep this mutualism as well as their own sustainability. Regulating the individual components in aim of achieving an optimization of the whole system is thus an important scenario in nature species. Smart regulation, intelligent and timely communication between components could thus lead to a more efficient resources/information/energy usage, which has been recognized as the internet of things (IoT) technology. Similarly, distributed energy systems could also optimize the efficiency of energy infrastructure and reduce the waste (**Figure 31b**). Focusing on energy efficiency, this system-level design mainly includes the insertion, implementation, installation, and coordination of the MPS in a higher-level system. For example, MPS can be used as the power plant for a 'MotorHome', supplying powers to all the appliances used in the recreational vehicle (RV), where an intelligent mini-IoE system can more efficiently manage the supply-consumption correlation between the MPS and the consumer streams. This MPS-incorporated smart IoE concept can be further used in those 'smart home' and 'smart city' projects, where multiple types of MPS such as solar window, solar tile, solar roof and solar farm, can be incorporated as a nod in the energy cyber network analogous to the nature's "ant's nest" where the delivery of electricity follows a highly efficient traffic way that is free from any jam or shortage.

7. Conclusion

High-performance natural materials and systems have been well-developed over millions of years' evolution and present valuable sources for inspiration in engineering both the (i) individual material components in a subsystem and the (ii) whole integrated system. PSC incorporating the biomimicry by learning from the nature's concepts and designs is expected to be a new route towards next-generation PV-MPS technologies, like their prior success in driving a paradigm shift in development of other modern science and technology communities. In terms of individual material components in a PSC subsystem, there have been successes in demonstrating highly efficient bio-inspired strategies to improve the performance and properties of electrodes (e.g., 'biomimetic ant-nest electrode structure', 'leaf vein electrode network', other nature's fractural design inspired hierarchy electrode), CTL (e.g., DNA, fractal neuron network, bR-inspired composite charge transfer materials, and other natural molecules such as porphyrins, natural conjugates and carbonized material incorporated CTL), and perovskite photoactive layer (e.g., specific micro-composite inspired by Nacre, bamboo, and wood, functional microscopic design aiming at self-cleaning and self-healing inspired by many natural examples, and many bio-molecular additives to improve specific property of the perovskite crystal) of the PSC. In the case of system and overall device design, potential bio-inspiration for MPS application include the solar tracker (inspired by sunflower and *phototropism* of plants), micro-cell array that is composed of sub-cells separated by a scaffold (inspired by insect's compound eye array), and various bio-related manufacturing that have been or are being developed (although perfectly mimicking the manufacturing of natural species remains an open question in the

whole field of biomimicry, 3D printing and other state-of-art techniques are helping to get a closer step).

7.1 Prospects

In the specific case of PSC-based MPS, the future bio-inspiration may focus on the downsides of current PSCs. Compared with incumbent PV techniques such as Si, CIGS, CdTe PVs and OPVs, PSCs are more advantageous in the relatively high PCE (due to the superior optoelectronic properties of halide perovskite materials), low cost (solution-processability of the core perovskite photoactive layer and other charge transfer layers), high degree of flexibility and large power density (light weight device for high output power due to the large light extinction coefficient of perovskite so that a thin layer can harvest high intensity of light), which enable them potential candidates for the next-generation PV-MPS. Nevertheless, the drawbacks of PSCs include the (i) mechanical fragility and brittleness, (ii) environmental impact, (iii) life-time & life-cycle issue, and (iv) limitations in scale-up manufacturing might be the specific focus where the bio-inspiration can pop in. In addition to this, (v) the system-level design to intelligently coordinate MPS with other electricity consumers could be another dimension to consider the bio-inspiration. **Figure 32a** shows the '*Cannikin Law*' (Wooden Bucket Theory) of PV-MPS, where the bio-inspiration can serve to fill up the gap from the shortest staves (five drawbacks of PSCs mentioned above). In particular, for each issue, potential solutions to the shortage of current PSC-based MPS inspired by nature are shown as follows:

(i) Mechanical robustness: At material level, for each component in a PSC, the trade-off between mechanical property and optical (electrical) properties remains a challenge, particularly for the MPS aimed at the portable, foldable and stretchable applications. For example, the front transparent electrode of PSC for wearable MPS requires certain levels of flexibility with qualified optical transmittance and electrical conductivity. While most commonly used flexible TCO-based transparent electrodes (e.g., ITO) coated on plastic substrates (e.g., PET and PEN) usually have an electrical conductance failure after long-term mechanical bending. Designing a flexible metal NW network inspired by nature's fractal hierarchy structure (e.g., leaf veins, neuron network) could help boost the charge transport efficiency meanwhile maintaining the mechanical endurance; employing the nacre laminar composite structure could further assist in enhancing the mechanical strength. In case of the CTL, design of an insect's compound eye and/or butterfly wing inspired periodic nanostructure could uniformly disperse the stress to avoid the concentrated stress induced fracture. Moreover, engineering the micromorphology of the perovskite layer by introducing either ordered micro-composite structures inspired by nature's micro-patterns found in various plants, or molecular dye that can simultaneously boost the mechanical strength and electronic properties (through molecular bonding) are of great promise. At device level, designing and innovating the device architecture inspired by the hemispheric retina to redistribute external stress but also enlarge the light harvest could be another pathway. Such hemispheric design with PSC sticking outside can further be utilized in those curved roofs, UAV wings, etc. Overall, there have been various strategies in enhancing the mechanical properties of PSC through versatile bio-inspired designs and materials. As the learning and investigation of nature's secret goes by, there will be growing ingenious strategies inspired and applied for PSC based MPS.

(ii) Environmental impact: The major safety concern of the PSC is the heavy metal pollution of the B-site atom (Pb, Sn, etc.) in the halide perovskite material. Mostly the Pb poisoning will increase oxidative stress and consequently cause various deleterious effects on hematopoietic, reproductive, renal, and central nervous system.[540] The US Centers for Disease Control (CDC)[541,542] has set the upper limit of blood lead at 10 μg/dl (10 μg/100 g) and at 5 μg/dl for adults and children, respectively. Additionally, elevated Pb in the environment can originate in decreased growth and reproductive rates of plants and animals, as well as neurological effects in vertebrates. Hence, there is an urgent requirement to prevent the Pb leakage and contamination.

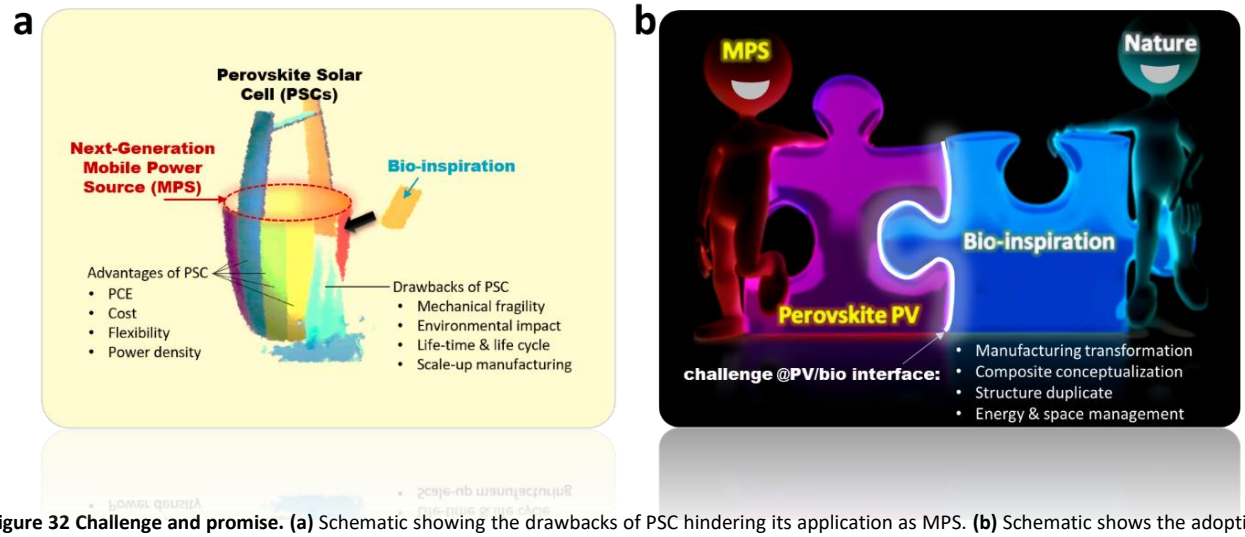

Figure 32 Challenge and promise. (a) Schematic showing the drawbacks of PSC hindering its application as MPS. **(b)** Schematic shows the adoption of bio-inspired strategy to realize perovskite solar cell MPS.

So far, the best practical policy is to screen the Pb within the PSC to prevent the leakage, which however is a heavily under-researched field that needs attention. Some 'self-healing' strategies have been introduced recently to sufficiently quarantine the Pb from a broken device.[461] The encapsulation of the perovskite within protective shells or alternatively adding reactive agents to bind and quarantine Pb to avoid leakage can also be possible solutions.[543] Pharmacologically, the removal of lead is usually relay on the 'chelation therapy'[544] (a medical procedure involving administrations of chelating agents to react and remove heavy metals from the body). For the specific case of Pb, ethylenediaminetetraacetic acid (EDTA) is used as the agent which can binds and holds on to (chelates) Pb. Using such chelating agents in PSCs may also help to 'hold' the Pb in case of PSC broken under rain (otherwise rain will wash the leaked lead into the environment). In nature, Pb also binds to a variety of different biomolecules ranging from enzymes and proteins, though interactions of Pb in thiolate-rich sites found in metalloregulatory proteins (e.g., Pbr, Znt, and CadC) and in enzymes (e.g., δ-aminolevulinic acid dehydratase (ALAD)).[545] Incorporating certain biomolecules into the encapsulation of PSC may further anchor the Pb within the device in case of device broken and bad weather that would otherwise accelerate the Pb leakage. In addition to these, as the water is the major agent that can accelerate the Pb escaping from the PSC, sufficiently preventing the water infiltrating the device can be effective to prevent the Pb leakage. Following this, some self-cleaning strategies resembling the lotus leaf (non-wettability) can help.

(iii) Life-time & life-cycle issue: Life-time, life-cycle analysis, investment, pay-back time, levelized cost of energy (LCOE), etc., are important indices to establish a benchmark for pre-industrial and laboratory-scale processes as well as individual MPS applications. As the life-time of PSC is notoriously shorter (ranging at month to year scale, state-of-art lifetime ~10^{-1} to 10^{0} yrs.) than their commercial counterparts (> 10^{1} yrs.), the first priority of the PSC industry should be the stability issue. In case of real application, critical weather (rain, hail, and snow), hot temperatures, day-night cycling induced light intensity change, and other environmental activities will further evaluate the baseline requirement of the device lifetime. On the other hand, recycling of the used device at the end of the life-cycle is also important but lacks sufficient research efforts. These fields require highly efficient and intelligent strategies to push the PSC based MPS closer towards the market. Prior bio-inspiration has resulted in the early attempts in enhancing the PSC's stability (e.g., bio-molecular doping to anchor the crystal lattice, introducing hydrophobic bio-molecules in each layer of the device and designing a lotus-like surface structure to repeal the water), adaptation to the light change, and other functionalities to adapt the dynamic changes in the environment for elongating the practical lifetime (e.g., self-healing, self-cleaning). More attentions may be needed at the life-cycle end. In fact, the arrival of the end-of-lifecycle of a PV is unavoidable in any case. International Renewable Energy Agency (IRENA) estimates that the recyclable materials in retired solar modules will be worth $15 billion in recoverable assets by the year 2050.[546] At that specific end point, how to deal with the retired perovskite PV should be an important topic. The conventional way to deal with the PV waste is a disposal process, either by landfill or by incineration. While both of these disposal methods need capital investment, energy/labor consumption and even consideration on environmental impact (lead leakage). Alternatively, regenerating the retired PVs via recycling the raw materials and re-collect them from the PV waste could circumvent these issues. From this scenario, development of a simple but efficient method to regenerate perovskite PV and extend their lifecycle is of importance.

(iv) Limitations in scale-up manufacturing: The efficient manufacturing capable of continuously producing the PSC-based MPS is important. As perovskite-based MPS can be developed for numerous portable uses, their form or design cannot be limited to certain types. For this, suitable manufacturing techniques are required to properly upscale the lab-level PSC device toward MPS-oriented production. For example, MPS products with a 'wallpaper-like' feature that can be attached and detached at anywhere anytime could be of great interest. Realization of such MPS will need a mature up-scaling manufacturing that can print large-area PSC device on flexible substrates. Bio-inspired additive manufacturing (e.g., 3D printing bio-photovoltaics) might be a good starting point. While considering the (a) materials' uniqueness (crystal, instability in ambient, critical crystallization requirement), (b) device's complexity (multiple nanometer-scale layer-by-layer structure), (c) high optical and electrical requirement (transmittance, electrical conductance, contact between each layer), and (d) tradeoff between cost and payback, PSC manufacturing will need more delicate design and intensive efforts. Ingeniously designing and innovating a PSC-customized processing by incorporating newly-concepted bio-inspired strategies will be a big leap. In parallel, the energy consumption in the PSC manufacturing is an important factor affecting its potential in market. Instead of energy-intensive and cumbersome processing, biological system can synthesize high property materials (robust mechanical properties in woods and bamboo, magnetic single crystals in jelly fish) through multiple biochemical reactions (e.g., *biomineralization*[547]) at room-temperature, aqueous environment (in contrast, TiO_2 in PSC require high temperature sintering and perovskite crystallization needs over 100 °C annealing). Simplifying those bio-synthetic method into an artificial synthetic paradigm that can have a bunch of advantages in application of PSC manufacturing would be intriguing.

(v) System-level design: By bringing the bio-inspired strategies into the nano-/micro- scale design and the manufacturing techniques, the functionality of PSCs can be strengthened. For example, a solar tracking technology inspired by sunflower has been introduced to solar cell technologies. By dynamically tracking the direction of sunlight, the loss of electricity generation of PSC from the tilted incident light will be complemented. The angle of incident light is influenced by the various spatial status of Earth (the daily and the annual rotation) and the local environment of the system. The state-of-the-art

solar tracking technology should be able to dynamically react with the change of direction of sunlight in energy-efficient and cost-effective ways. Additionally, a scaffold to make a single device into separated into multiple devices can be a solution. By adopting the scaffold design, inspired by *ommatidium* (unit of the compound eyes of arthropods like insects, crustaceans and millipedes), and rhodopsin of retina, for PSC, their stability against various stimuli from temperature change and humidity can be improved. Since each partitioned device can generate electricity individually, the whole device failure can be avoided if the system is partially broken or damaged by the external factors. Such the spatial design of the scaffold was done by nature to have an efficient arrangement of sub-cells so that each component device can be densely positioned inside. The scaffold also allows the system to have mechanically resilience against fracture, which is enabled by the stress-deconcentrating feature of the scaffold. Synchronization and coordination at system level can also be found at manufacturing and synthesis sides. Natural 'organ factory' could efficiently synthesize multi-functional structures and/or materials. The mimicry of the natural synthetic ways to manufacture artificial materials and a system production of certain functional proteins can bring new opportunities to boost the manufacturing of both perovskite materials and the PSC devices.

7.2 Challenges

Bio-inspiration for next-generation MPS is a multidisciplinary topic that requires expertise related with biology, material science, engineering, electrics, chemistry and physics. This will require researchers with different backgrounds teaming up a more comprehensive group to have a higher-level overview of the whole field and then come up with targeted strategies to fill up the 'shortest staves' of the 'Wooden Bucket' in **Figure 32a**. Bio-inspiration can provide the shortcut solution to those targeted strategies but remains to be a more general and abstractive concept. Most prior built bio-inspirations are focusing on mechanical and structural engineering, as provided by several well-documented review papers.[374,375,536,548–550] For the specific application in PSC and PV-MPS remains not fully explored. This will require more efforts to interface between the parallelly developing PSC and bio-inspiration, as conceptualized in **Figure 32b**. Nevertheless, several challenges are deemed to be addressed:

(i) The synthesis mechanisms found in nature need further investigation and the transformation of the bio-manufacturing to the artificial needs more studies. For application purpose, bio-inspired manufacturing needs to be developed to reveal underlying mechanisms behind the intriguing properties. For example, nature grows organisms in mild environment but needs a long period (bones need years to grow), while artificial manufacturing of PSC requires a high time efficiency from minutes to hours scale. Understanding the nature's mechanism of the material formation (growth) and identifying the origin of the long-time necessity may inspire the creation of a substitutive way to mimic the natural process in a much shorter time. For example, the crystal growth in natural mild conditions (e.g., biomineralization, biological investigation on produced materials, such as shells, teeth and bone, as well as the processes that lead to the formation of these hierarchically structured organic−inorganic composites) may provide implications of designing new synthetic routes. The chemical reaction route and new mechanism found in those bio prototypes could provide opportunities for growing the perovskite in a milder ambient environment instead of the current critical requirement of high temperature and low moisture. This, however, will require an improved understanding and knowledgebase of these nature's synthesis.

(ii) Materials in nature are structured and usually a mixture of various kinds of sub-components (e.g., polysaccharides, proteins, and collagen fibers) instead of a single component. They usually have a synergistic '1+1>2' effect as the property of each component is meager but the whole hybrid is of high-performance. While in PSCs, for each functional layer material it requires very high purity and any impurities will significantly compromise the overall device performance. In addition, there is a limited material inventory from which the specific layer could choose from. Making composite materials and use them as functional layers in the PSC could possibly reduce the cost in synthesizing high purity material but also expand the material inventory for PSC. However, before truly understanding the synergistic mechanisms of a composite, it will be trial and error for down selecting 'the' composite material.

(iii) The periodic microstructure found in nature (e.g., nanostructures on butterfly wings providing the camouflage colors and superhydrophobicity for self-cleaning; nanostructures on Gecko feet providing striking attachment and detachment on wall and also giving self-cleaning, self-repairing, and wear-resistant properties) is abundant. While in most state-of-art PSCs, each layer is a simple planar layer and it is difficult to design a self-assembly process to manufacture the functional layer with a designed micro-structure. Duplicating these natural microstructures with impressive performance in optical and mechanical function is still beyond the ongoing PSC manufacturing techniques.

(iv) Nature utilizes the energy and space in a highly efficient and elegant way. PSCs still have a huge energy loss limiting their efficiency below the Shockley−Queisser Limit (SQ) limit. The SQ limit refers to the maximum theoretical efficiency of 33.7% for a single-junction solar cell, mostly due to the spectral mismatch between the wide spectrum of sunlight and a single-bandgap of a solar cell. The thermalization (short wavelength light generated hot carrier and a fast cooling of hot carrier to release energy to heat) and in-band transparency (no absorption of long wavelength light below bandgap) are the major losses and sum up to over 50% efficiency losses for a solar cell. In the vertebrate animals' retina, there are different types of optical-responsive proteins in different cells that are reactive to light of different wavelength. These individual cells are responsive to the light independently and parallelly aligned in the array to detect the monochronic light individually from the white sunlight. In solar cell, tandem solar cell could mitigate the thermalization loss by incorporating multiple individual light absorber in the

tandem stacking. As most tandem PSCs vertically stack the short-wavelength responsive cell and long-wavelength responsive cell, a parallel design of individual cells coupled by a prism to split the light might be another design for the tandem solar cell. On the other hand, coherence phenomena are prevailed in biophysical system, which could lead to nontrivial optoelectronic behaviors.[551] For example, fluorescence interference pattern obtained from polydiacetylene (PDA) indicates an extraordinary microscopic coherence length for a single exciton.[552] In the field of solar cell, utilizing nontrivial behaviors such as multi-excitation generation (MEG) could make it possible to break the SQ limit. One example is the singlet-fission in certain organic chromophores (e.g., pentacene, rubrene, perylene) where one excited singlet-state transforms into two triplet states upon close interaction with a ground-state molecule of the same kind. In this way, doubled external quantum efficiency (EQE) of the device at short wavelength regions to 200% is of possible. By incorporating SF chromophores into solar cells, total exciton yield of 133%, EQE to 130%, and IQE (internal quantum efficiency) to 170% have been observed in tetracene sensitized silicon solar cells,[553] pentacene incorporated organic solar cell,[554] and TIPS–pentacene/PbSe QD solar cells,[555] respectively. Yet these prior conceptualizations are not likely to break the Shockley–Queisser limit in the near future, because of the low starting PCE point (even the tetracene sensitized silicon solar cell exhibit low PCE of 5.1% due to the lateral structure and many technological challenges such as overall thickness control, stoichiometry and trap density[553]). Hybridizing the perovskite with those chromophores to trigger MEG in aim of exceed SQ limit could be one promising solution, while many other issues such interface, disordered states in organic chromophores and delicate design of an energy/electrical transduction in the system remain to address.

Conflicts of interest

There are no conflicts to declare.

Acknowledgements

K.W. and Y.H. acknowledge the support from Air Force Office of Scientific Research under award number FA9550-17-1-0341. S.P. acknowledges the financial support from the Office of Naval Research through grant number N000141912461. D.Y. acknowledges the support from NSF-Crest grant number HRD 1547771. T.Y. and J.Y. acknowledge the support from Office of Naval Research through grant number N000141712520.

References

1 S. L. Miller and H. C. Urey, *Science*, 1959, **130**, 245–251.
2 D. Deamer and A. L. Weber, *Cold Spring Harbor perspectives in biology*, 2010, **2**, a004929.
3 G. W. Crabtree and N. S. Lewis, *Physics today*, 2007, **60**, 37–42.
4 R. J. Rapf and V. Vaida, *Physical Chemistry Chemical Physics*, 2016, **18**, 20067–20084.
5 H. Kirst, C. Formighieri and A. Melis, *Biochimica et Biophysica Acta (BBA) - Bioenergetics*, 2014, **1837**, 1653–1664.
6 C. T. Rodgers and P. J. Hore, *Proceedings of the National Academy of Sciences*, 2009, **106**, 353–360.
7 J. S. Ishay, B. Perna, Y. Hochberg and M. Goldstein, *Bulletin of Mathematical Biology*, 1980, **42**, 681–689.
8 J. S. Ishay, *Microscopy*, 2004, **53**, 623–633.
9 J. L. Behler and D. A. Behler, *Frogs: A Chorus of Colors*, Sterling Publishing Company, Inc., 2008.
10 R. Madurai Elavarasan, G. Shafiullah, K. Raju, V. Mudgal, M. T. Arif, T. Jamal, S. Subramanian, V. S. Sriraja Balaguru, K. S. Reddy and U. Subramaniam, *Appl Energy*, 2020, **279**, 115739.
11 A. K. Jena, A. Kulkarni and T. Miyasaka, *Chem. Rev.*, 2019, **119**, 3036–3103.
12 M. Saliba, J.-P. Correa-Baena, M. Grätzel, A. Hagfeldt and A. Abate, *Angew. Chem.*, 2018, **130**, 2582–2598.
13 H. S. Jung and N.-G. Park, *small*, 2015, **11**, 10–25.
14 N.-G. Park, *Materials today*, 2015, **18**, 65–72.
15 S. D. Stranks, G. E. Eperon, G. Grancini, C. Menelaou, M. J. Alcocer, T. Leijtens, L. M. Herz, A. Petrozza and H. J. Snaith, *Science*, 2013, **342**, 341–344.
16 A. Kojima, K. Teshima, Y. Shirai and T. Miyasaka, *Journal of the American Chemical Society*, 2009, **131**, 6050–6051.
17 NREL, Best Research-Cell Efficiency Chart, https://www.nrel.gov/pv/cell-efficiency.html, (accessed May 11, 2020).
18 M. Kaltenbrunner, G. Adam, E. D. Głowacki, M. Drack, R. Schwödiauer, L. Leonat, D. H. Apaydin, H. Groiss, M. C. Scharber, M. S. White, N. S. Sariciftci and S. Bauer, *Nature Mater*, 2015, **14**, 1032–1039.
19 M. Kaltenbrunner, M. S. White, E. D. Głowacki, T. Sekitani, T. Someya, N. S. Sariciftci and S. Bauer, *Nature Communications*, 2012, **3**, 770.
20 X. Zhang, V. A. Öberg, J. Du, J. Liu and E. M. J. Johansson, *Energy Environ. Sci.*, 2018, **11**, 354–364.
21 X. Zhang, C. Zhang, D. Li, S. Cao, M. Yin, P. Wang, G. Ding, L. Yang, J. Cheng and L. Lu, *Nanoscale Res Lett*, 2019, **14**, 1–9.
22 A. Romeo, G. Khrypunov, F. Kurdesau, M. Arnold, D. L. Bätzner, H. Zogg and A. N. Tiwari, *Solar Energy Materials and Solar Cells*, 2006, **90**, 3407–3415.
23 S. Kang, J. Jeong, S. Cho, Y. J. Yoon, S. Park, S. Lim, J. Y. Kim and H. Ko, *J. Mater. Chem. A*, 2019, **7**, 1107–1114.
24 Ryan Genz + Francesca Rosella, https://www.msichicago.org/explore/whats-here/exhibits/fast-forward/previously-featured/ryan-genz-francesca-rosella/, (accessed March 19, 2021).
25 Meet Project Jacquard, Google's Plan To Turn Your Clothes Into A Touch, https://www.fastcompany.com/3046864/meet-project-jacquard-googles-plan-to-turn-all-your-clothes-into-a-touchscreen, (accessed March 19, 2021).
26 Andrew Carp, Wearable Electronics | Electrical and Computer Engineering Design Handbook, https://sites.tufts.edu/eeseniordesignhandbook/2015/wearable-electronics/, (accessed March 19, 2021).
27 *Wikipedia*, 2020.
28 Ryan Genz + Francesca Rosella - Museum of Science and Industry, https://www.msichicago.org/explore/whats-here/exhibits/fast-forward/previously-featured/ryan-genz-francesca-rosella/, (accessed July 25, 2020).

29 Meet Project Jacquard, Google's Plan To Turn Your Clothes Into A Touch, https://www.fastcompany.com/3046864/meet-project-jacquard-googles-plan-to-turn-all-your-clothes-into-a-touchscreen, (accessed July 25, 2020).
30 Solar-Powered Drone Could Fly Nonstop For Five Years, https://www.iflscience.com/technology/solar-powered-drone-could-fly-nonstop-five-years/, (accessed March 19, 2021).
31 Solar-Powered Drone Could Fly Nonstop For Five Years | IFLScience, https://www.iflscience.com/technology/solar-powered-drone-could-fly-nonstop-five-years/, (accessed July 25, 2020).
32 W. W. Zhang, L. G. Zhang, Z. W. Yan and L. Wang, *IOP Conf. Ser.: Mater. Sci. Eng.*, 2019, **608**, 012016.
33 C. H. M. Jenkins, *Bio-Inspired Engineering*, Momentum Press, 2011.
34 R. L. Ripley and B. Bhushan, *Philosophical Transactions of the Royal Society A: Mathematical, Physical and Engineering Sciences*, 2016, **374**, 20160192.
35 J.-W. Yoo, D. J. Irvine, D. E. Discher and S. Mitragotri, *Nature Reviews Drug Discovery*, 2011, **10**, 521–535.
36 A. Diamond, T. Nowotny and M. Schmuker, *Front. Neurosci.*, , DOI:10.3389/fnins.2015.00491.
37 H.-S. Kim, C.-R. Lee, J.-H. Im, K.-B. Lee, T. Moehl, A. Marchioro, S.-J. Moon, R. Humphry-Baker, J.-H. Yum, J. E. Moser, M. Grätzel and N.-G. Park, *Scientific Reports*, 2012, **2**, 591.
38 K. Kalyanasundaram and M. Graetzel, *Current opinion in Biotechnology*, 2010, **21**, 298–310.
39 S. Bai, P. Da, C. Li, Z. Wang, Z. Yuan, F. Fu, M. Kawecki, X. Liu, N. Sakai, J. T.-W. Wang, S. Huettner, S. Buecheler, M. Fahlman, F. Gao and H. J. Snaith, *Nature*, 2019, **571**, 245–250.
40 G. Lee, M. Kim, Y. W. Choi, N. Ahn, J. Jang, J. Yoon, S. M. Kim, J.-G. Lee, D. Kang and H. S. Jung, *Energy & Environmental Science*, 2019, **12**, 3182–3191.
41 J. Feng, *APL Materials*, 2014, **2**, 081801.
42 M. Park, H. J. Kim, I. Jeong, J. Lee, H. Lee, H. J. Son, D.-E. Kim and M. J. Ko, *Advanced Energy Materials*, 2015, **5**, 1501406.
43 S. Ahn, E. D. Jung, S.-H. Kim, H. Kim, S. Lee, M. H. Song and J.-Y. Kim, *Nano Lett.*, 2019, **19**, 3707–3715.
44 S. Sun, Y. Fang, G. Kieslich, T. J. White and A. K. Cheetham, *J. Mater. Chem. A*, 2015, **3**, 18450–18455.
45 Y.-C. Lin, X.-Y. Peng, L.-C. Wang, Y.-L. Lin, C.-H. Wu and S.-C. Liang, *J Mater Sci: Mater Electron*, 2014, **25**, 461–465.
46 M. Pander, S. Dietrich, S.-H. Schulze, U. Eitner and M. Ebert, in *2011 12th Intl. Conf. on Thermal, Mechanical Multi-Physics Simulation and Experiments in Microelectronics and Microsystems*, 2011, p. 1/6-6/6.
47 Y. Kato, L. K. Ono, M. V. Lee, S. Wang, S. R. Raga and Y. Qi, *Advanced Materials Interfaces*, 2015, **2**, 1500195.
48 J. Chen, D. Lee and N.-G. Park, *ACS Appl. Mater. Interfaces*, 2017, **9**, 36338–36349.
49 L. Meng, C. Sun, R. Wang, W. Huang, Z. Zhao, P. Sun, T. Huang, J. Xue, J.-W. Lee, C. Zhu, Y. Huang, Y. Li and Y. Yang, *J. Am. Chem. Soc.*, 2018, **140**, 17255–17262.
50 E. M. Sanehira, B. J. Tremolet de Villers, P. Schulz, M. O. Reese, S. Ferrere, K. Zhu, L. Y. Lin, J. J. Berry and J. M. Luther, *ACS Energy Lett.*, 2016, **1**, 38–45.
51 H. Back, G. Kim, J. Kim, J. Kong, T. K. Kim, H. Kang, H. Kim, J. Lee, S. Lee and K. Lee, *Energy Environ. Sci.*, 2016, **9**, 1258–1263.
52 K. Domanski, J.-P. Correa-Baena, N. Mine, M. K. Nazeeruddin, A. Abate, M. Saliba, W. Tress, A. Hagfeldt and M. Grätzel, *ACS Nano*, 2016, **10**, 6306–6314.
53 M. Jørgensen, K. Norrman and F. C. Krebs, *Solar Energy Materials and Solar Cells*, 2008, **92**, 686–714.
54 J. Zhao, X. Zheng, Y. Deng, T. Li, Y. Shao, A. Gruverman, J. Shield and J. Huang, *Energy Environ. Sci.*, 2016, **9**, 3650–3656.
55 H. Zhang, J. Xiao, J. Shi, H. Su, Y. Luo, D. Li, H. Wu, Y.-B. Cheng and Q. Meng, *Advanced Functional Materials*, 2018, **28**, 1802985.
56 S. He, L. Qiu, D.-Y. Son, Z. Liu, E. J. Juarez-Perez, L. K. Ono, C. Stecker and Y. Qi, *ACS Energy Lett.*, 2019, **4**, 2032–2039.
57 C. D. Bailie, M. G. Christoforo, J. P. Mailoa, A. R. Bowring, E. L. Unger, W. H. Nguyen, J. Burschka, N. Pellet, J. Z. Lee, M. Grätzel, R. Noufi, T. Buonassisi, A. Salleo and M. D. McGehee, *Energy Environ. Sci.*, 2015, **8**, 956–963.
58 F. Guo, H. Azimi, Y. Hou, T. Przybilla, M. Hu, C. Bronnbauer, S. Langner, E. Spiecker, K. Forberich and C. J. Brabec, *Nanoscale*, 2015, **7**, 1642–1649.
59 N. Ahn, I. Jeon, J. Yoon, E. I. Kauppinen, Y. Matsuo, S. Maruyama and M. Choi, *J. Mater. Chem. A*, 2018, **6**, 1382–1389.
60 Z. Wei, H. Chen, K. Yan, X. Zheng and S. Yang, *J. Mater. Chem. A*, 2015, **3**, 24226–24231.
61 Z. Li, S. A. Kulkarni, P. P. Boix, E. Shi, A. Cao, K. Fu, S. K. Batabyal, J. Zhang, Q. Xiong, L. H. Wong, N. Mathews and S. G. Mhaisalkar, *ACS Nano*, 2014, **8**, 6797–6804.
62 K. M. Kim, S. Ahn, W. Jang, S. Park, O. O. Park and D. H. Wang, *Solar Energy Materials and Solar Cells*, 2018, **176**, 435–440.
63 J. H. Lee, J. H. Heo, S. H. Im and O. O. Park, *ACS Appl. Mater. Interfaces*, 2020, **12**, 10527–10534.
64 S. Wan, H. Hu, J. Peng, Y. Li, Y. Fan, L. Jiang and Q. Cheng, *Nanoscale*, 2016, **8**, 5649–5656.
65 X.-L. Ou, J. Feng, M. Xu and H.-B. Sun, *Opt. Lett., OL*, 2017, **42**, 1958–1961.
66 X.-L. Ou, M. Xu, J. Feng and H.-B. Sun, *Solar Energy Materials and Solar Cells*, 2016, **157**, 660–665.
67 I. Jeon, R. Xiang, A. Shawky, Y. Matsuo and S. Maruyama, *Adv. Energy Mater.*, 2019, **9**, 1801312.
68 G. Ai, Y. Dai, W. Mao, H. Zhao, Y. Fu, X. Song, Y. En, V. S. Battaglia, V. Srinivasan and G. Liu, *Nano Lett.*, 2016, **16**, 5365–5372.
69 T. Latty, K. Ramsch, K. Ito, T. Nakagaki, D. J. T. Sumpter, M. Middendorf and M. Beekman, *J R Soc Interface*, 2011, **8**, 1298–1306.
70 J. Buhl, K. Hicks, E. R. Miller, S. Persey, O. Alinvi and D. J. T. Sumpter, *Behav Ecol Sociobiol*, 2009, **63**, 451–460.
71 D. P. Bebber, J. Hynes, P. R. Darrah, L. Boddy and M. D. Fricker, *Proceedings of the Royal Society B: Biological Sciences*, 2007, **274**, 2307–2315.
72 T. Nakagaki, R. Kobayashi, Y. Nishiura and T. Ueda, *Proceedings of the Royal Society of London. Series B: Biological Sciences*, 2004, **271**, 2305–2310.
73 D. Miner, M. Pickett and M. desJardins, Atlantis Press, 2009, pp. 18–19.
74 H.-T. Zhang, P. Panda, J. Lin, Y. Kalcheim, K. Wang, J. W. Freeland, D. D. Fong, S. Priya, I. K. Schuller and S. K. Sankaranarayanan, *Applied Physics Reviews*, 2020, **7**, 011309.
75 M. Tegmark, *Life 3.0: Being human in the age of artificial intelligence*, Knopf, 2017.
76 H. Ito, W. Oka, H. Goto and H. Umeda, *Jpn. J. Appl. Phys.*, 2006, **45**, 4325.
77 H. J. Snaith, *The journal of physical chemistry letters*, 2013, **4**, 3623–3630.
78 D. Liu and T. L. Kelly, *Nature photonics*, 2014, **8**, 133–138.
79 P. Docampo, J. M. Ball, M. Darwich, G. E. Eperon and H. J. Snaith, *Nature communications*, 2013, **4**, 1–6.

80 B. J. Kim, D. H. Kim, Y.-Y. Lee, H.-W. Shin, G. S. Han, J. S. Hong, K. Mahmood, T. K. Ahn, Y.-C. Joo and K. S. Hong, *Energy & Environmental Science*, 2015, **8**, 916–921.
81 D. Yang, R. Yang, S. Priya and S. Liu, *Angewandte Chemie International Edition*, 2019, **58**, 4466–4483.
82 H. S. Jung, G. S. Han, N.-G. Park and M. J. Ko, *Joule*, 2019, **3**, 1850–1880.
83 J. Yoon, H. Sung, G. Lee, W. Cho, N. Ahn, H. S. Jung and M. Choi, *Energy & Environmental Science*, 2017, **10**, 337–345.
84 X. Fan, W. Nie, H. Tsai, N. Wang, H. Huang, Y. Cheng, R. Wen, L. Ma, F. Yan and Y. Xia, *Advanced Science*, 2019, **6**, 1900813.
85 F. Louwet, L. Groenendaal, J. Dhaen, J. Manca, J. Van Luppen, E. Verdonck and L. Leenders, *Synthetic Metals*, 2003, **135–136**, 115–117.
86 J. Huang, P. F. Miller, J. C. de Mello, A. J. de Mello and D. D. C. Bradley, *Synthetic Metals*, 2003, **139**, 569–572.
87 N. Kim, H. Kang, J.-H. Lee, S. Kee, S. H. Lee and K. Lee, *Advanced Materials*, 2015, **27**, 2317–2323.
88 J. Yun, *Advanced Functional Materials*, 2017, **27**, 1606641.
89 G. S. Han, S. Lee, M. L. Duff, F. Qin and J.-K. Lee, *ACS Appl. Mater. Interfaces*, 2018, **10**, 4697–4704.
90 M. Lee, Y. Jo, D. S. Kim, H. Y. Jeong and Y. Jun, *Journal of Materials Chemistry A*, 2015, **3**, 14592–14597.
91 M. Lee, Y. Jo, D. S. Kim and Y. Jun, *Journal of Materials Chemistry A*, 2015, **3**, 4129–4133.
92 J. Troughton, D. Bryant, K. Wojciechowski, M. J. Carnie, H. Snaith, D. A. Worsley and T. M. Watson, *Journal of Materials Chemistry A*, 2015, **3**, 9141–9145.
93 C. Roldán-Carmona, O. Malinkiewicz, A. Soriano, G. M. Espallargas, A. Garcia, P. Reinecke, T. Kroyer, M. I. Dar, M. K. Nazeeruddin and H. J. Bolink, *Energy Environ. Sci.*, 2014, **7**, 994–997.
94 X. Liu, X. Guo, Y. Lv, Y. Hu, J. Lin, Y. Fan, N. Zhang and X. Liu, *ACS Appl. Mater. Interfaces*, 2018, **10**, 18141–18148.
95 X. Hu, Z. Huang, X. Zhou, P. Li, Y. Wang, Z. Huang, M. Su, W. Ren, F. Li and M. Li, *Advanced Materials*, 2017, **29**, 1703236.
96 X. Hu, Z. Huang, F. Li, M. Su, Z. Huang, Z. Zhao, Z. Cai, X. Yang, X. Meng, P. Li, Y. Wang, M. Li, Y. Chen and Y. Song, *Energy Environ. Sci.*, 2019, **12**, 979–987.
97 J. Han, S. Yuan, L. Liu, X. Qiu, H. Gong, X. Yang, C. Li, Y. Hao and B. Cao, *J. Mater. Chem. A*, 2015, **3**, 5375–5384.
98 Y. Jin, Y. Sun, K. Wang, Y. Chen, Z. Liang, Y. Xu and F. Xiao, *Nano Res.*, 2018, **11**, 1998–2011.
99 I. Jeon, J. Yoon, U. Kim, C. Lee, R. Xiang, A. Shawky, J. Xi, J. Byeon, H. M. Lee and M. Choi, *Advanced Energy Materials*, 2019, **9**, 1901204.
100 I. Jeon, J. Yoon, N. Ahn, M. Atwa, C. Delacou, A. Anisimov, E. I. Kauppinen, M. Choi, S. Maruyama and Y. Matsuo, *The journal of physical chemistry letters*, 2017, **8**, 5395–5401.
101 I. Jeon, T. Chiba, C. Delacou, Y. Guo, A. Kaskela, O. Reynaud, E. I. Kauppinen, S. Maruyama and Y. Matsuo, *Nano letters*, 2015, **15**, 6665–6671.
102 K. Liu and L. Jiang, *Nano Today*, 2011, **6**, 155–175.
103 R. Lakes, *Nature*, 1993, **361**, 511–515.
104 P. Fratzl and R. Weinkamer, *Progress in Materials Science*, 2007, **52**, 1263–1334.
105 A. Roth-Nebelsick, D. Uhl, V. Mosbrugger and H. Kerp, *Ann Bot*, 2001, **87**, 553–566.
106 L. Sack and C. Scoffoni, *New Phytologist*, 2013, **198**, 983–1000.
107 L. V. Thekkekara and M. Gu, *Scientific Reports*, 2017, **7**, 45585.
108 T. Li, S. Li, X. Li, Z. Xu, J. Zhao, Y. Shi, Y. Wang, R. Yu, X. Liu, Q. Xu and W. Guo, *Science Bulletin*, 2020, **65**, 225–232.
109 G. Jia, J. Plentz, A. Dellith, C. Schmidt, J. Dellith, G. Schmidl and G. Andrä, *Nano-Micro Lett.*, 2020, **12**, 19.
110 J. F. Silvain, J. Chazelas and S. Trombert, *Applied surface science*, 2000, **153**, 211–217.
111 J.-Y. Lee, S. T. Connor, Y. Cui and P. Peumans, *Nano Lett.*, 2008, **8**, 689–692.
112 T. Tokuno, M. Nogi, M. Karakawa, J. Jiu, T. T. Nge, Y. Aso and K. Suganuma, *Nano Res.*, 2011, **4**, 1215–1222.
113 J. Lee, P. Lee, H. Lee, D. Lee, S. S. Lee and S. H. Ko, *Nanoscale*, 2012, **4**, 6408–6414.
114 E. C. Garnett, W. Cai, J. J. Cha, F. Mahmood, S. T. Connor, M. Greyson Christoforo, Y. Cui, M. D. McGehee and M. L. Brongersma, *Nature Materials*, 2012, **11**, 241–249.
115 B. Han, Q. Peng, R. Li, Q. Rong, Y. Ding, E. M. Akinoglu, X. Wu, X. Wang, X. Lu, Q. Wang, G. Zhou, J.-M. Liu, Z. Ren, M. Giersig, A. Herczynski, K. Kempa and J. Gao, *Nature Communications*, 2016, **7**, 12825.
116 Y. Jia, C. Chen, D. Jia, S. Li, S. Ji and C. Ye, *ACS Appl. Mater. Interfaces*, 2016, **8**, 9865–9871.
117 M. Lagrange, D. P. Langley, G. Giusti, C. Jiménez, Y. Bréchet and D. Bellet, *Nanoscale*, 2015, **7**, 17410–17423.
118 T. Tokuno, M. Nogi, J. Jiu, T. Sugahara and K. Suganuma, *Langmuir*, 2012, **28**, 9298–9302.
119 H. Du, T. Wan, B. Qu, F. Cao, Q. Lin, N. Chen, X. Lin and D. Chu, *ACS Appl. Mater. Interfaces*, 2017, **9**, 20762–20770.
120 M. Layani, M. Gruchko, O. Milo, I. Balberg, D. Azulay and S. Magdassi, *ACS Nano*, 2009, **3**, 3537–3542.
121 S. Zhu, Y. Gao, B. Hu, J. Li, J. Su, Z. Fan and J. Zhou, *Nanotechnology*, 2013, **24**, 335202.
122 T. Sannicolo, M. Lagrange, A. Cabos, C. Celle, J.-P. Simonato and D. Bellet, *Small*, 2016, **12**, 6052–6075.
123 D. S. Ghosh, T. L. Chen and V. Pruneri, *Appl. Phys. Lett.*, 2010, **96**, 041109.
124 K. D. M. Rao, C. Hunger, R. Gupta, G. U. Kulkarni and M. Thelakkat, *Phys. Chem. Chem. Phys.*, 2014, **16**, 15107–15110.
125 B. Han, K. Pei, Y. Huang, X. Zhang, Q. Rong, Q. Lin, Y. Guo, T. Sun, C. Guo, D. Carnahan, M. Giersig, Y. Wang, J. Gao, Z. Ren and K. Kempa, *Advanced Materials*, 2014, **26**, 873–877.
126 S. Kiruthika, R. Gupta, A. Anand, A. Kumar and G. U. Kulkarni, *ACS Appl. Mater. Interfaces*, 2015, **7**, 27215–27222.
127 C. F. Guo, T. Sun, Q. Liu, Z. Suo and Z. Ren, *Nature Communications*, 2014, **5**, 3121.
128 H. Wu, D. Kong, Z. Ruan, P.-C. Hsu, S. Wang, Z. Yu, T. J. Carney, L. Hu, S. Fan and Y. Cui, *Nature Nanotechnology*, 2013, **8**, 421–425.
129 Y. Yu, Y. Zhang, K. Li, C. Yan and Z. Zheng, *Small*, 2015, **11**, 3444–3449.
130 X. Wang, R. Wang, H. Zhai, L. Shi and J. Sun, *J. Mater. Chem. C*, 2018, **6**, 5738–5745.
131 B. Han, Y. Huang, R. Li, Q. Peng, J. Luo, K. Pei, A. Herczynski, K. Kempa, Z. Ren and J. Gao, *Nature communications*, 2014, **5**, 1–7.
132 P. Moon and D. E. Spencer, *American Journal of Physics*, 1961, **29**, 717–717.
133 B. B. Mandelbrot and J. A. Wheeler, *American Journal of Physics*, 1983, **51**, 286–287.
134 R. E. Horton, *GSA Bulletin*, 1945, **56**, 275–370.
135 A. N. Strahler, *GSA Bulletin*, 1952, **63**, 1117–1142.
136 J. E. de A. Mariath, R. P. dos Santos and R. P. dos Santos, *Revista Brasileira de Biociências*.
137 M. M. Tavakoli, K.-H. Tsui, Q. Zhang, J. He, Y. Yao, D. Li and Z. Fan, *ACS Nano*, 2015, **9**, 10287–10295.
138 B. Dou, E. M. Miller, J. A. Christians, E. M. Sanehira, T. R. Klein, F. S. Barnes, S. E. Shaheen, S. M. Garner, S. Ghosh, A. Mallick, D. Basak and M. F. A. M. van Hest, *J. Phys. Chem. Lett.*, 2017, **8**, 4960–4966.

139 S. Ke, C. Chen, N. Fu, H. Zhou, M. Ye, P. Lin, W. Yuan, X. Zeng, L. Chen and H. Huang, *ACS Appl. Mater. Interfaces*, 2016, **8**, 28406–28411.
140 S. Castro-Hermosa, J. Dagar, A. Marsella and T. M. Brown, *IEEE Electron Device Letters*, 2017, **38**, 1278–1281.
141 M. Lee, Y. Ko, B. K. Min and Y. Jun, *ChemSusChem*, 2016, **9**, 31–35.
142 X. Wang, Z. Li, W. Xu, S. A. Kulkarni, S. K. Batabyal, S. Zhang, A. Cao and L. H. Wong, *Nano Energy*, 2015, **11**, 728–735.
143 Y. Xiao, G. Han, H. Zhou and J. Wu, *RSC Adv.*, 2016, **6**, 2778–2784.
144 B. A. Nejand, P. Nazari, S. Gharibzadeh, V. Ahmadi and A. Moshaii, *Chem. Commun.*, 2017, **53**, 747–750.
145 X. Pu, W. Song, M. Liu, C. Sun, C. Du, C. Jiang, X. Huang, D. Zou, W. Hu and Z. L. Wang, *Advanced Energy Materials*, 2016, **6**, 1601048.
146 I. Marriam, X. Wang, M. Tebyetekerwa, G. Chen, F. Zabihi, J. Pionteck, S. Peng, S. Ramakrishna, S. Yang and M. Zhu, *J. Mater. Chem. A*, 2018, **6**, 13633–13643.
147 W. Shao, M. Tebyetekerwa, I. Marriam, W. Li, Y. Wu, S. Peng, S. Ramakrishna, S. Yang and M. Zhu, *Journal of Power Sources*, 2018, **396**, 683–690.
148 M. Tebyetekerwa, Z. Xu, W. Li, X. Wang, I. Marriam, S. Peng, S. Ramkrishna, S. Yang and M. Zhu, *ACS Appl. Energy Mater.*, 2018, **1**, 377–386.
149 G. Chen, T. Chen, K. Hou, W. Ma, M. Tebyetekerwa, Y. Cheng, W. Weng and M. Zhu, *Carbon*, 2018, **127**, 218–227.
150 X. Wang, S. Meng, M. Tebyetekerwa, Y. Li, J. Pionteck, B. Sun, Z. Qin and M. Zhu, *Composites Part A: Applied Science and Manufacturing*, 2018, **105**, 291–299.
151 X. Wang, S. Meng, M. Tebyetekerwa, W. Weng, J. Pionteck, B. Sun, Z. Qin and M. Zhu, *Synthetic Metals*, 2017, **233**, 86–93.
152 S. Yu, X. Wang, H. Xiang, M. Tebyetekerwa and M. Zhu, *Sci. China Mater.*, 2019, **62**, 995–1004.
153 Y. Zhang, Y. Zhao, J. Ren, W. Weng and H. Peng, *Advanced Materials*, 2016, **28**, 4524–4531.
154 J. Zhou, X. Li, C. Yang, Y. Li, K. Guo, J. Cheng, D. Yuan, C. Song, J. Lu and B. Wang, *Advanced Materials*, 2019, **31**, 1804439.
155 M. Liao, L. Ye, Y. Zhang, T. Chen and H. Peng, *Advanced Electronic Materials*, 2019, **5**, 1800456.
156 Z. Wen, M.-H. Yeh, H. Guo, J. Wang, Y. Zi, W. Xu, J. Deng, L. Zhu, X. Wang, C. Hu, L. Zhu, X. Sun and Z. L. Wang, *Science Advances*, 2016, **2**, e1600097.
157 L. Xie, X. Chen, Z. Wen, Y. Yang, J. Shi, C. Chen, M. Peng, Y. Liu and X. Sun, *Nano-Micro Lett.*, 2019, **11**, 39.
158 X. Pu, W. Hu and Z. L. Wang, *Small*, 2018, **14**, 1702817.
159 J. Ren, Q. Xu and Y.-G. Li, *Flex. Print. Electron.*, 2018, **3**, 013001.
160 X. Hu, F. Li and Y. Song, *ACS Energy Lett.*, 2019, **4**, 1065–1072.
161 A. Hanuska, B. Chandramohan, L. Bellamy, P. Burke, R. Ramanathan and V. Balakrishnan, 47.
162 H. Yang, J. Yu, H. Zo and M. Choi, *Telematics and Informatics*, 2016, **33**, 256–269.
163 L. Qiu, J. Deng, X. Lu, Z. Yang and H. Peng, *Angewandte Chemie International Edition*, 2014, **53**, 10425–10428.
164 R. Li, X. Xiang, X. Tong, J. Zou and Q. Li, *Adv. Mater.*, 2015, **27**, 3831–3835.
165 H. Hu, K. Yan, M. Peng, X. Yu, S. Chen, B. Chen, B. Dong, X. Gao and D. Zou, *J. Mater. Chem. A*, 2016, **4**, 3901–3906.
166 L. Qiu, S. He, J. Yang, J. Deng and H. Peng, *Small*, 2016, **12**, 2419–2424.
167 M. Teodorescu, *Journal of Textiles*, 2014, **2014**, 1–9.
168 K. G. Satyanarayana, C. K. S. Pillai, K. Sukumaran, S. G. K. Pillai, P. K. Rohatgi and K. Vijayan, *J Mater Sci*, 1982, **17**, 2453–2462.
169 L. Fathi, *Strukturelle und mechanische Eigenschaften des Holzes von Kokospalmen, Ölpalmen und Dattelpalmen*.
170 I. Burgert, K. Frühmann, J. Keckes, P. Fratzl and S. Stanzl-Tschegg, *Trees*, 2004, **18**, 480–485.
171 A. S. Deshpande, I. Burgert and O. Paris, *Small*, 2006, **2**, 994–998.
172 J. E. Gordon, G. Jeronimidis, W. Watt, B. Harris and A. C. Ham, *Philosophical Transactions of the Royal Society of London. Series A, Mathematical and Physical Sciences*, 1980, **294**, 545–550.
173 J. Keckes, I. Burgert, K. Frühmann, M. Müller, K. Kölln, M. Hamilton, M. Burghammer, S. V. Roth, S. Stanzl-Tschegg and P. Fratzl, *Nature Materials*, 2003, **2**, 810–813.
174 Y. Sun, R. B. Sills, X. Hu, Z. W. Seh, X. Xiao, H. Xu, W. Luo, H. Jin, Y. Xin, T. Li, Z. Zhang, J. Zhou, W. Cai, Y. Huang and Y. Cui, *Nano Lett.*, 2015, **15**, 3899–3906.
175 K. Zhu, Z. Lu, S. Cong, G. Cheng, P. Ma, Y. Lou, J. Ding, N. Yuan, M. H. Rümmeli and G. Zou, *Small*, 2019, **15**, 1902878.
176 M. Cai, V. T. Tiong, T. Hreid, J. Bell and H. Wang, *J. Mater. Chem. A*, 2015, **3**, 2784–2793.
177 J. Deng, L. Qiu, X. Lu, Z. Yang, G. Guan, Z. Zhang and H. Peng, *J. Mater. Chem. A*, 2015, **3**, 21070–21076.
178 B. Dong, J. Hu, X. Xiao, S. Tang, X. Gao, Z. Peng and D. Zou, *Adv. Mater. Technol.*, 2019, **4**, 1900131.
179 S. He, L. Qiu, X. Fang, G. Guan, P. Chen, Z. Zhang and H. Peng, *J. Mater. Chem. A*, 2015, **3**, 9406–9410.
180 D.-Y. Khang, H. Jiang, Y. Huang and J. A. Rogers, *Science*, 2006, **311**, 208–212.
181 J. Song, *Current Opinion in Solid State and Materials Science*, 2015, **19**, 160–170.
182 J. J. Park, P. Won and S. H. Ko, *Int. J. of Precis. Eng. and Manuf.-Green Tech.*, 2019, **6**, 147–161.
183 M. Jo, S. Bae, I. Oh, J. Jeong, B. Kang, S. J. Hwang, S. S. Lee, H. J. Son, B.-M. Moon, M. J. Ko and P. Lee, *ACS Nano*, 2019, **13**, 12500–12510.
184 H. Li, W. Wang, Y. Yang, Y. Wang, P. Li, J. Huang, J. Li, Y. Lu, Z. Li, Z. Wang, B. Fan, J. Fang and W. Song, *ACS Nano*, 2020, **14**, 1560–1568.
185 J. Qi, H. Xiong, C. Hou, Q. Zhang, Y. Li and H. Wang, *Nanoscale*, 2020, **12**, 3646–3656.
186 T. H. Yang, H. Hida, D. Ichige, J. Mizuno, C. Robert Kao and J. Shintake, *Phys. Status Solidi A*, 2020, pssa.201900891.
187 L.-H. Xie, J. Liang, J. Song, C.-R. Yin and W. Huang, *Current Organic Chemistry*, 2010, **14**, 2169–2195.
188 T. P. Saragi, T. Spehr, A. Siebert, T. Fuhrmann-Lieker and J. Salbeck, *Chemical reviews*, 2007, **107**, 1011–1065.
189 J. Yi, Y. Wang, Q. Luo, Y. Lin, H. Tan, H. Wang and C.-Q. Ma, *Chemical Communications*, 2016, **52**, 1649–1652.
190 X.-F. Wu, W.-F. Fu, Z. Xu, M. Shi, F. Liu, H.-Z. Chen, J.-H. Wan and T. P. Russell, *Advanced Functional Materials*, 2015, **25**, 5954–5966.
191 R. G. Clarkson and M. Gomberg, *Journal of the American Chemical Society*, 1930, **52**, 2881–2891.
192 F. Bischoff and H. Adkins, *Journal of the American Chemical Society*, 1923, **45**, 1030–1033.
193 L.-H. Xie, F. Liu, C. Tang, X.-Y. Hou, Y.-R. Hua, Q.-L. Fan and W. Huang, *Organic letters*, 2006, **8**, 2787–2790.
194 B. Xu, D. Bi, Y. Hua, P. Liu, M. Cheng, M. Grätzel, L. Kloo, A. Hagfeldt and L. Sun, *Energy & Environmental Science*, 2016, **9**, 873–877.
195 D. Bi, B. Xu, P. Gao, L. Sun, M. Grätzel and A. Hagfeldt, *Nano Energy*, 2016, **23**, 138–144.

196 K. Liu, Y. Yao, J. Wang, L. Zhu, M. Sun, B. Ren, L. Xie, Y. Luo, Q. Meng and X. Zhan, *Materials Chemistry Frontiers*, 2017, **1**, 100–110.
197 M. Saliba, S. Orlandi, T. Matsui, S. Aghazada, M. Cavazzini, J.-P. Correa-Baena, P. Gao, R. Scopelliti, E. Mosconi and K.-H. Dahmen, *Nature Energy*, 2016, **1**, 1–7.
198 G. Pozzi, S. Orlandi, M. Cavazzini, D. Minudri, L. Macor, L. Otero and F. Fungo, *Organic letters*, 2013, **15**, 4642–4645.
199 A. Torres and L. G. Rego, *The Journal of Physical Chemistry C*, 2014, **118**, 26947–26954.
200 B. Xu, J. Zhang, Y. Hua, P. Liu, L. Wang, C. Ruan, Y. Li, G. Boschloo, E. M. Johansson and L. Kloo, *Chem*, 2017, **2**, 676–687.
201 Y. Wang, T.-S. Su, H.-Y. Tsai, T.-C. Wei and Y. Chi, *Scientific reports*, 2017, **7**, 1–9.
202 Y. Wang, Z. Zhu, C.-C. Chueh, A. K.-Y. Jen and Y. Chi, *Advanced Energy Materials*, 2017, **7**, 1700823.
203 S. Kazim, F. J. Ramos, P. Gao, M. K. Nazeeruddin, M. Grätzel and S. Ahmad, *Energy & Environmental Science*, 2015, **8**, 1816–1823.
204 J. E. Anthony, J. S. Brooks, D. L. Eaton and S. R. Parkin, *Journal of the American Chemical Society*, 2001, **123**, 9482–9483.
205 G. Giri, E. Verploegen, S. C. Mannsfeld, S. Atahan-Evrenk, D. H. Kim, S. Y. Lee, H. A. Becerril, A. Aspuru-Guzik, M. F. Toney and Z. Bao, *Nature*, 2011, **480**, 504–508.
206 C. D. Sheraw, T. N. Jackson, D. L. Eaton and J. E. Anthony, *Advanced Materials*, 2003, **15**, 2009–2011.
207 S. Paek, P. Qin, Y. Lee, K. T. Cho, P. Gao, G. Grancini, E. Oveisi, P. Gratia, K. Rakstys and S. A. Al-Muhtaseb, *Advanced Materials*, 2017, **29**, 1606555.
208 A. Mishra and P. Bäuerle, *Angewandte Chemie International Edition*, 2012, **51**, 2020–2067.
209 H. Bronstein, Z. Chen, R. S. Ashraf, W. Zhang, J. Du, J. R. Durrant, P. Shakya Tuladhar, K. Song, S. E. Watkins and Y. Geerts, *Journal of the American Chemical Society*, 2011, **133**, 3272–3275.
210 P. Liu, Y. Wu, H. Pan, Y. Li, S. Gardner, B. S. Ong and S. Zhu, *Chemistry of Materials*, 2009, **21**, 2727–2732.
211 J. H. Seo, E. B. Namdas, A. Gutacker, A. J. Heeger and G. C. Bazan, *Advanced Functional Materials*, 2011, **21**, 3667–3672.
212 H. Li, K. Fu, A. Hagfeldt, M. Grätzel, S. G. Mhaisalkar and A. C. Grimsdale, *Angewandte Chemie*, 2014, **126**, 4169–4172.
213 J. Roncali, P. Blanchard and P. Frère, *Journal of Materials Chemistry*, 2005, **15**, 1589–1610.
214 L. Groenendaal, F. Jonas, D. Freitag, H. Pielartzik and J. R. Reynolds, *Advanced Materials*, 2000, **12**, 481–494.
215 M. L. Petrus, T. Bein, T. J. Dingemans and P. Docampo, *Journal of Materials Chemistry A*, 2015, **3**, 12159–12162.
216 A. Krishna, D. Sabba, J. Yin, A. Bruno, L. J. Antila, C. Soci, S. Mhaisalkar and A. C. Grimsdale, *Journal of Materials Chemistry A*, 2016, **4**, 8750–8754.
217 S. Mathew, A. Yella, P. Gao, R. Humphry-Baker, B. F. Curchod, N. Ashari-Astani, I. Tavernelli, U. Rothlisberger, M. K. Nazeeruddin and M. Grätzel, *Nature chemistry*, 2014, **6**, 242–247.
218 A. Yella, C.-L. Mai, S. M. Zakeeruddin, S.-N. Chang, C.-H. Hsieh, C.-Y. Yeh and M. Grätzel, *Angewandte Chemie*, 2014, **126**, 3017–3021.
219 M.-E. Ragoussi, M. Ince and T. Torres, *European Journal of Organic Chemistry*, 2013, **2013**, 6475–6489.
220 M.-H. Li, J.-H. Yum, S.-J. Moon and P. Chen, *Energies*, 2016, **9**, 331.
221 S. H. Hwang, J. Roh, J. Lee, J. Ryu, J. Yun and J. Jang, *Journal of Materials Chemistry A*, 2014, **2**, 16429–16433.
222 J.-W. Lee, S. H. Lee, H.-S. Ko, J. Kwon, J. H. Park, S. M. Kang, N. Ahn, M. Choi, J. K. Kim and N.-G. Park, *Journal of Materials Chemistry A*, 2015, **3**, 9179–9186.
223 J. Song, E. Zheng, J. Bian, X.-F. Wang, W. Tian, Y. Sanehira and T. Miyasaka, *Journal of Materials Chemistry A*, 2015, **3**, 10837–10844.
224 Q. Wang, Y. Shao, Q. Dong, Z. Xiao, Y. Yuan and J. Huang, *Energy & Environmental Science*, 2014, **7**, 2359–2365.
225 C.-H. Chiang, Z.-L. Tseng and C.-G. Wu, *Journal of Materials Chemistry A*, 2014, **2**, 15897–15903.
226 O. Malinkiewicz, A. Yella, Y. H. Lee, G. M. Espallargas, M. Graetzel, M. K. Nazeeruddin and H. J. Bolink, *Nature Photonics*, 2014, **8**, 128–132.
227 J. You, Z. Hong, Y. Yang, Q. Chen, M. Cai, T.-B. Song, C.-C. Chen, S. Lu, Y. Liu and H. Zhou, *ACS nano*, 2014, **8**, 1674–1680.
228 J. Seo, S. Park, Y. C. Kim, N. J. Jeon, J. H. Noh, S. C. Yoon and S. I. Seok, *Energy & Environmental Science*, 2014, **7**, 2642–2646.
229 L.-C. Chen, J.-C. Chen, C.-C. Chen and C.-G. Wu, *Nanoscale research letters*, 2015, **10**, 312.
230 J.-Y. Jeng, K.-C. Chen, T.-Y. Chiang, P.-Y. Lin, T.-D. Tsai, Y.-C. Chang, T.-F. Guo, P. Chen, T.-C. Wen and Y.-J. Hsu, *Advanced materials*, 2014, **26**, 4107–4113.
231 X. Liu, M. Lei, Y. Zhou, B. Song and Y. Li, *Applied Physics Letters*, 2015, **107**, 063901.
232 A. T. Barrows, A. J. Pearson, C. K. Kwak, A. D. Dunbar, A. R. Buckley and D. G. Lidzey, *Energy & Environmental Science*, 2014, **7**, 2944–2950.
233 K. Mahmood, B. S. Swain, A. R. Kirmani and A. Amassian, *J. Mater. Chem. A*, 2015, **3**, 9051–9057.
234 S. Carretero-Palacios, A. Jiménez-Solano and H. Míguez, *ACS Energy Lett.*, 2016, **1**, 323–331.
235 K. Yao, H. Zhong, Z. Liu, M. Xiong, S. Leng, J. Zhang, Y. Xu, W. Wang, L. Zhou, H. Huang and A. K.-Y. Jen, *ACS Nano*, 2019, **13**, 5397–5409.
236 Q. Luo, C. Zhang, X. Deng, H. Zhu, Z. Li, Z. Wang, X. Chen and S. Huang, *ACS Appl. Mater. Interfaces*, 2017, **9**, 34821–34832.
237 V. Zhirnov, *Semiconductor synthetic biology roadmap*, Semiconductor Research Corporation Durham, 2018.
238 S. Kawanishi, Y. Hiraku and S. Oikawa, *Mutation Research/Reviews in Mutation Research*, 2001, **488**, 65–76.
239 S. S. Wallace, *Free Radical Biology and Medicine*, 2002, **33**, 1–14.
240 N. C. Seeman, *Annual review of biochemistry*, 2010, **79**, 65–87.
241 C. J. Murphy, M. R. Arkin, Y. Jenkins, N. D. Ghatlia, S. H. Bossmann, N. J. Turro and J. K. Barton, *Science*, 1993, **262**, 1025–1029.
242 S. Larsson, *Journal of the American Chemical Society*, 1981, **103**, 4034–4040.
243 H. M. McConnell, *The Journal of Chemical Physics*, 1961, **35**, 508–515.
244 S. Priyadarshy, S. M. Risser and D. N. Beratan, *The Journal of Physical Chemistry*, 1996, **100**, 17678–17682.
245 D. N. Beratan, S. Priyadarshy and S. M. Risser, *Chemistry & biology*, 1997, **4**, 3–8.
246 G. S. Tong, I. V. Kurnikov and D. N. Beratan, *The Journal of Physical Chemistry B*, 2002, **106**, 2381–2392.
247 J. Jortner, M. Bixon, T. Langenbacher and M. E. Michel-Beyerle, *Proceedings of the National Academy of Sciences*, 1998, **95**, 12759–12765.
248 B. Giese, *Current opinion in chemical biology*, 2002, **6**, 612–618.
249 E. Meggers and B. Giese, *Nucleosides & nucleotides*, 1999, **18**, 1317–1318.

250 S. M. Iqbal, G. Balasundaram, S. Ghosh, D. E. Bergstrom and R. Bashir, *Applied Physics Letters*, 2005, **86**, 153901.
251 C. Nogues, S. R. Cohen, S. Daube, N. Apter and R. Naaman, *The Journal of Physical Chemistry B*, 2006, **110**, 8910–8913.
252 B. Xu, P. Zhang, X. Li and N. Tao, *Nano letters*, 2004, **4**, 1105–1108.
253 P. T. Henderson, D. Jones, G. Hampikian, Y. Kan and G. B. Schuster, *Proceedings of the National Academy of Sciences*, 1999, **96**, 8353–8358.
254 E. M. Conwell, *Proceedings of the National Academy of Sciences*, 2005, **102**, 8795–8799.
255 P. Zalar, D. Kamkar, R. Naik, F. Ouchen, J. G. Grote, G. C. Bazan and T.-Q. Nguyen, *Journal of the American Chemical Society*, 2011, **133**, 11010–11013.
256 Y. Zhang, M. Wang, S. D. Collins, H. Zhou, H. Phan, C. Proctor, A. Mikhailovsky, F. Wudl and T.-Q. Nguyen, *Angewandte Chemie*, 2014, **126**, 248–253.
257 J. Dagar, M. Scarselli, M. De Crescenzi and T. M. Brown, *ACS Energy Letters*, 2016, **1**, 510–515.
258 J. Dagar, G. Scavia, M. Scarselli, S. Destri, M. De Crescenzi and T. M. Brown, *Nanoscale*, 2017, **9**, 19031–19038.
259 F. Toschi, D. Catone, P. O'Keeffe, A. Paladini, S. Turchini, J. Dagar and T. M. Brown, *Advanced Functional Materials*, 2018, **28**, 1707126.
260 Abd. R. bin M. Yusoff, J. Kim, J. Jang and M. K. Nazeeruddin, *ChemSusChem*, 2016, **9**, 1736–1742.
261 Y. Hou, K. Wang, D. Yang, Y. Jiang, N. Yennawar, K. Wang, M. Sanghadasa, C. Wu and S. Priya, *ACS Energy Lett.*, 2019, **4**, 2646–2655.
262 B. B. Mandelbrot, .
263 W. J. Watterson, R. D. Montgomery and R. P. Taylor, *Scientific reports*, 2017, **7**, 1–9.
264 B. Mandelbrot, *science*, 1967, **156**, 636–638.
265 J. Bassingthwaighte, L. Liebovitch and B. West, *New York*.
266 R. G. Hohlfeld and N. Cohen, *Fractals*, 1999, **7**, 79–84.
267 K. Wang, C. Liu, T. Meng, C. Yi and X. Gong, *Chem. Soc. Rev.*, 2016, **45**, 2937–2975.
268 A. Kay, I. Cesar and M. Grätzel, *Journal of the American Chemical Society*, 2006, **128**, 15714–15721.
269 R. Meier, C. Birkenstock, C. M. Palumbiny and P. Müller-Buschbaum, *Physical Chemistry Chemical Physics*, 2012, **14**, 15088–15098.
270 R. L. Chamousis, L. Chang, W. J. Watterson, R. D. Montgomery, R. P. Taylor, A. J. Moule, S. E. Shaheen, B. Ilan, J. van de Lagemaat and F. E. Osterloh, *Journal of Materials Chemistry A*, 2014, **2**, 16608–16616.
271 X. Qin, Z. Miao, Y. Fang, D. Zhang, J. Ma, L. Zhang, Q. Chen and X. Shao, *Langmuir*, 2012, **28**, 5218–5226.
272 S. Kaniyankandy, J. Nuwad, C. Thinaharan, G. K. Dey and C. G. S. Pillai, *Nanotechnology*, 2007, **18**, 125610.
273 E. Ben-Jacob and P. Garik, *Nature*, 1990, **343**, 523–530.
274 Q. Zhou, S. Wang, N. Jia, L. Liu, J. Yang and Z. Jiang, *Materials Letters*, 2006, **60**, 3789–3792.
275 A. P. Alivisatos, *Science*, 2000, **289**, 736–737.
276 Y. Liu, K. He, G. Chen, W. R. Leow and X. Chen, *Chem. Rev.*, 2017, **117**, 12893–12941.
277 M. Liu, S. Wang and L. Jiang, *Nat Rev Mater*, 2017, **2**, 17036.
278 R. Senthil and S. Yuvaraj, *Int J Energy Res*, 2019, **43**, 1068–1081.
279 S. M. Kang, S. Jang, J.-K. Lee, J. Yoon, D.-E. Yoo, J.-W. Lee, M. Choi and N.-G. Park, *Small*, 2016, **12**, 2443–2449.
280 M. Kim, S. Jang, J. Choi, S. M. Kang and M. Choi, *Nano-Micro Lett.*, 2019, **11**, 53.
281 S.-Y. Chuang, H.-L. Chen, J. Shieh, C.-H. Lin, C.-C. Cheng, H.-W. Liu and C.-C. Yu, *Nanoscale*, 2010, **2**, 799–805.
282 Y. M. Song, H. J. Choi, J. S. Yu and Y. T. Lee, *Optics express*, 2010, **18**, 13063–13071.
283 K. Deng, Z. Liu, M. Wang and L. Li, *Adv. Funct. Mater.*, 2019, **29**, 1900830.
284 W. Zhang, M. Anaya, G. Lozano, M. E. Calvo, M. B. Johnston, H. Míguez and H. J. Snaith, *Nano Lett.*, 2015, **15**, 1698–1702.
285 K. Meng, S. Gao, L. Wu, G. Wang, X. Liu, G. Chen, Z. Liu and G. Chen, *Nano Lett.*, 2016, **16**, 4166–4173.
286 P. V. Braun and P. Wiltzius, *Nature*, 1999, **402**, 603–604.
287 R. C. Schroden, M. Al-Daous, C. F. Blanford and A. Stein, *Chemistry of materials*, 2002, **14**, 3305–3315.
288 Y.-T. Li, Y. Tian, H. Tian, T. Tu, G.-Y. Gou, Q. Wang, Y.-C. Qiao, Y. Yang and T.-L. Ren, *Sensors*, 2018, **18**, 1368.
289 N. K. Allam, C.-W. Yen, R. D. Near and M. A. El-Sayed, *Energy & Environmental Science*, 2011, **4**, 2909–2914.
290 L. S. Li, T. Xu, Y. J. Zhang, J. Jin, T. J. Li, B. Zou and J.-P. Wang, *Journal of Vacuum Science & Technology A: Vacuum, Surfaces, and Films*, 2001, **19**, 1037–1041.
291 K. M. Al-Aribe, G. K. Knopf and A. S. Bassi, in *Microfluidics, BioMEMS, and Medical Microsystems XI*, International Society for Optics and Photonics, 2013, vol. 8615, p. 86150Q.
292 A. Nitzan and M. A. Ratner, *Science*, 2003, **300**, 1384–1389.
293 L. Sepunaru, N. Friedman, I. Pecht, M. Sheves and D. Cahen, *Journal of the American Chemical Society*, 2012, **134**, 4169–4176.
294 S. Mukhopadhyay, S. R. Cohen, D. Marchak, N. Friedman, I. Pecht, M. Sheves and D. Cahen, *Acs Nano*, 2014, **8**, 7714–7722.
295 O. Berthoumieu, A. V. Patil, W. Xi, L. Aslimovska, J. J. Davis and A. Watts, *Nano letters*, 2012, **12**, 899–903.
296 Z. Guo, D. Liang, S. Rao and Y. Xiang, *Nano Energy*, 2015, **11**, 654–661.
297 L. Mustárdy, K. Buttle, G. Steinbach and G. Garab, *The Plant Cell*, 2008, **20**, 2552–2557.
298 N. Yang, Y. Zhang, J. E. Halpert, J. Zhai, D. Wang and L. Jiang, *Small*, 2012, **8**, 1762–1770.
299 Z. Dancsházy and Z. Tokaji, *FEBS letters*, 2000, **476**, 171–173.
300 R. Li, C. M. Li, H. Bao, Q. Bao and V. S. Lee, *Applied Physics Letters*, 2007, **91**, 223901.
301 V. Thavasi, T. Lazarova, S. Filipek, M. Kolinski, E. Querol, A. Kumar, S. Ramakrishna, E. Padrós and V. Renugopalakrishnan, *Journal of nanoscience and nanotechnology*, 2009, **9**, 1679–1687.
302 R. Mohammadpour and S. Janfaza, *ACS Sustainable Chemistry & Engineering*, 2015, **3**, 809–813.
303 J. Chellamuthu, P. Nagaraj, S. G. Chidambaram, A. Sambandam and A. Muthupandian, *Journal of Photochemistry and Photobiology B: Biology*, 2016, **162**, 208–212.
304 S. Das, C. Wu, Z. Song, Y. Hou, R. Koch, P. Somasundaran, S. Priya, B. Barbiellini and R. Venkatesan, *ACS Appl. Mater. Interfaces*, 2019, **11**, 30728–30734.
305 A. Rakovich, A. Sukhanova, N. Bouchonville, E. Lukashev, V. Oleinikov, M. Artemyev, V. Lesnyak, N. Gaponik, M. Molinari and M. Troyon, *Nano letters*, 2010, **10**, 2640–2648.
306 M. H. Griep, K. A. Walczak, E. M. Winder, D. R. Lueking and C. R. Friedrich, *Biosensors and Bioelectronics*, 2010, **25**, 1493–1497.
307 M. Zoonens, F. Giusti, F. Zito and J.-L. Popot, *Biochemistry*, 2007, **46**, 10392–10404.
308 V. Renugopalakrishnan, B. Barbiellini, C. King, M. Molinari, K. Mochalov, A. Sukhanova, I. Nabiev, P. Fojan, H. L. Tuller and M. Chin, *The Journal of Physical Chemistry C*, 2014, **118**, 16710–16717.
309 C. King, B. Barbiellini, D. Moser and V. Renugopalakrishnan, *Physical Review B*, 2012, **85**, 125106.

310 H.-M. Chen, K.-R. Jheng and A.-D. Yu, *Biosensors and Bioelectronics*, 2017, **91**, 24–31.
311 M. Frydrych, P. Silfsten, S. Parkkinen, J. Parkkinen and T. Jaaskelainen, *Biosystems*, 2000, **54**, 131–140.
312 K. Prashanthan, B. Naydenov, K. Lips, E. Unger and R. W. MacQueen, *J. Chem. Phys.*, 2020, **153**, 164711.
313 H. Lu, X. Chen, J. E. Anthony, J. C. Johnson and M. C. Beard, *J. Am. Chem. Soc.*, 2019, **141**, 4919–4927.
314 H. Brueckner, Porphyrins and Chlorins | The Brückner Research Group, https://bruckner.research.uconn.edu/porphyrinoid-synthesis/, (accessed July 30, 2020).
315 S. Samiullah and J. R. Roberts, *Poultry science*, 2013, **92**, 2783–2788.
316 K. Wang, C. Liu, P. Du, J. Zheng and X. Gong, *Energy & Environmental Science*, 2015, **8**, 1245–1255.
317 H.-H. Chou, Y.-H. Chiang, M.-H. Li, P.-S. Shen, H.-J. Wei, C.-L. Mai, P. Chen and C.-Y. Yeh, *ACS Energy Lett.*, 2016, **1**, 956–962.
318 S. Chen, P. Liu, Y. Hua, Y. Li, L. Kloo, X. Wang, B. Ong, W.-K. Wong and X. Zhu, *ACS Appl. Mater. Interfaces*, 2017, **9**, 13231–13239.
319 Y.-H. Chiang, H.-H. Chou, W.-T. Cheng, Y.-R. Li, C.-Y. Yeh and P. Chen, *ACS Energy Letters*, 2018, **3**, 1620–1626.
320 C.-L. Mai, Y.-L. Huang, G.-H. Lee, S.-M. Peng and C.-Y. Yeh, *Chemistry–A European Journal*, 2008, **14**, 5120–5124.
321 M.-C. Kuo, L.-A. Li, W.-N. Yen, S.-S. Lo, C.-W. Lee and C.-Y. Yeh, *Dalton Transactions*, 2007, 1433–1439.
322 T.-H. Huang, Y.-J. Chen, S.-S. Lo, W.-N. Yen, C.-L. Mai, M.-C. Kuo and C.-Y. Yeh, *Dalton Transactions*, 2006, 2207–2213.
323 S. H. Kang, C. Lu, H. Zhou, S. Choi, J. Kim and H. K. Kim, *Dyes and Pigments*, 2019, **163**, 734–739.
324 U.-H. Lee, R. Azmi, S. Sinaga, S. Hwang, S. H. Eom, T.-W. Kim, S. C. Yoon, S.-Y. Jang and I. H. Jung, *ChemSusChem*, 2017, **10**, 3780–3787.
325 R. Azmi, U.-H. Lee, F. T. A. Wibowo, S. H. Eom, S. C. Yoon, S.-Y. Jang and I. H. Jung, *ACS Appl. Mater. Interfaces*, 2018, **10**, 35404–35410.
326 J. Cao, X. Lv, P. Zhang, T. T. Chuong, B. Wu, X. Feng, C. Shan, J. Liu and Y. Tang, *Advanced Materials*, 2018, **30**, 1800568.
327 A. Yella, H.-W. Lee, H. N. Tsao, C. Yi, A. K. Chandiran, M. K. Nazeeruddin, E. W.-G. Diau, C.-Y. Yeh, S. M. Zakeeruddin and M. Grätzel, *science*, 2011, **334**, 629–634.
328 J.-H. Yum, E. Baranoff, F. Kessler, T. Moehl, S. Ahmad, T. Bessho, A. Marchioro, E. Ghadiri, J.-E. Moser and C. Yi, *Nature communications*, 2012, **3**, 1–8.
329 J. Luo, M. Xu, R. Li, K.-W. Huang, C. Jiang, Q. Qi, W. Zeng, J. Zhang, C. Chi and P. Wang, *Journal of the American Chemical Society*, 2014, **136**, 265–272.
330 K. Gao, Z. Zhu, B. Xu, S. B. Jo, Y. Kan, X. Peng and A. K.-Y. Jen, *Adv. Mater.*, 2017, **29**, 1703980.
331 M. Li, Y. Li, S. Sasaki, J. Song, C. Wang, H. Tamiaki, W. Tian, G. Chen, T. Miyasaka and X.-F. Wang, *ChemSusChem*, 2016, **9**, 2862–2869.
332 M. Li, S. Sasaki, Y. Sanehira, T. Miyasaka, H. Tamiaki, T. Ikeuchi, G. Chen and X.-F. Wang, *Journal of Photochemistry and Photobiology A: Chemistry*, 2018, **353**, 639–644.
333 M. Li, N. Li, W. Hu, G. Chen, S. Sasaki, K. Sakai, T. Ikeuchi, T. Miyasaka, H. Tamiaki and X.-F. Wang, *ACS Appl. Energy Mater.*, 2018, **1**, 9–16.
334 S. B. Mane, A. A. Sutanto, C.-F. Cheng, M.-Y. Xie, C.-I. Chen, M. Leonardus, S.-C. Yeh, B. B. Beyene, E. W.-G. Diau and C.-T. Chen, *ACS applied materials & interfaces*, 2017, **9**, 31950–31958.
335 E. T. Johnson, M. A. Berhow and P. F. Dowd, *Journal of Chemical Ecology*, 2008, **34**, 757.
336 N. Saito and J. B. Harborne, *Phytochemistry*, 1992, **31**, 3009–3015.
337 K. S. Gould, J. McKelvie and K. R. Markham, *Plant, Cell & Environment*, 2002, **25**, 1261–1269.
338 S. U. Mertens-Talcott, J. Rios, P. Jilma-Stohlawetz, L. A. Pacheco-Palencia, B. Meibohm, S. T. Talcott and H. Derendorf, *Journal of agricultural and food chemistry*, 2008, **56**, 7796–7802.
339 S. R. Pereira, R. Pereira, I. Figueiredo, V. Freitas, T. C. Dinis and L. M. Almeida, *PLoS One*, 2017, **12**, e0174116.
340 S. A. Shah, F. U. Amin, M. Khan, M. N. Abid, S. U. Rehman, T. H. Kim, M. W. Kim and M. O. Kim, *Journal of neuroinflammation*, 2016, **13**, 1–16.
341 M. Takikawa, S. Inoue, F. Horio and T. Tsuda, *The Journal of nutrition*, 2010, **140**, 527–533.
342 O. Dangles and J.-A. Fenger, *Molecules*, 2018, **23**, 1970.
343 Carotenoids, https://lpi.oregonstate.edu/mic/dietary-factors/phytochemicals/carotenoids, (accessed July 17, 2020).
344 H. Tapiero, D. M. Townsend and K. D. Tew, *Biomed Pharmacother*, 2004, **58**, 100–110.
345 N. Mezzomo and S. R. S. Ferreira, Carotenoids Functionality, Sources, and Processing by Supercritical Technology, https://www.hindawi.com/journals/jchem/2016/3164312/, (accessed July 17, 2020).
346 T. Maoka, *J Nat Med*, 2020, **74**, 1–16.
347 C. F. Morelli, M. Biagiotti, V. M. Pappalardo, M. Rabuffetti and G. Speranza, *Natural product research*, 2015, **29**, 750–755.
348 N. R. Farnsworth and N. Bunapraphatsara, *Thai medicinal plants recommended for primary health care system*, Medicinal Plant Information Center, 1992.
349 P. Moongkarndi, N. Kosem, S. Kaslungka, O. Luanratana, N. Pongpan and N. Neungton, *Journal of ethnopharmacology*, 2004, **90**, 161–166.
350 W. Maiaugree, S. Lowpa, M. Towannang, P. Rutphonsan, A. Tangtrakarn, S. Pimanpang, P. Maiaugree, N. Ratchapolthavisin, W. Sang-Aroon and W. Jarernboon, *Scientific reports*, 2015, **5**, 15230.
351 A.-R. Im, L. Han, E. R. Kim, J. Kim, Y. S. Kim and Y. Park, *Phytotherapy Research*, 2012, **26**, 1249–1255.
352 S. Jain and M. S. Mehata, *Scientific reports*, 2017, **7**, 1–13.
353 M. S. Coutinho, E. Latocheski, J. M. Neri, A. C. Neves, J. B. Domingos, L. N. Cavalcanti, L. H. Gasparotto, E. P. Moraes and F. G. Menezes, *RSC advances*, 2019, **9**, 30007–30011.
354 A. M. Elseman, W. Sharmoukh, S. Sajid, P. Cui, J. Ji, S. Dou, D. Wei, H. Huang, W. Xi, L. Chu, Y. Li, B. Jiang and M. Li, *Advanced Science*, 2018, **5**, 1800568.
355 K. Wongcharee, V. Meeyoo and S. Chavadej, *Solar Energy Materials and Solar Cells*, 2007, **91**, 566–571.
356 N. Gokilamani, N. Muthukumarasamy, M. Thambidurai, A. Ranjitha and D. Velauthapillai, *Journal of Sol-Gel Science and Technology*, , DOI:10.1007/s10971-013-2994-9.
357 M. M. Giusti and R. E. Wrolstad, *Current protocols in food analytical chemistry*, 2001, F1-2.
358 A. Castañeda-Ovando, M. de Lourdes Pacheco-Hernández, M. E. Páez-Hernández, J. A. Rodríguez and C. A. Galán-Vidal, *Food chemistry*, 2009, **113**, 859–871.
359 A. Gengatharan, G. A. Dykes and W. S. Choo, *LWT-Food Science and Technology*, 2015, **64**, 645–649.
360 H. Hug, M. Bader, P. Mair and T. Glatzel, *Applied Energy*, 2014, **115**, 216–225.
361 A. Mei, X. Li, L. Liu, Z. Ku, T. Liu, Y. Rong, M. Xu, M. Hu, J. Chen and Y. Yang, *science*, 2014, **345**, 295–298.
362 H. Chen and S. Yang, *Journal of Materials Research*, 2017, **32**, 3011–3020.

363 Y. Liu, S. Ji, S. Li, W. He, K. Wang, H. Hu and C. Ye, *Journal of Materials Chemistry A*, 2015, **3**, 14902–14909.
364 C.-Y. Chan, Y. Wang, G.-W. Wu and E. W.-G. Diau, *Journal of Materials Chemistry A*, 2016, **4**, 3872–3878.
365 H. Chen and S. Yang, *Advanced materials*, 2017, **29**, 1603994.
366 K. Cao, Z. Zuo, J. Cui, Y. Shen, T. Moehl, S. M. Zakeeruddin, M. Grätzel and M. Wang, *Nano Energy*, 2015, **17**, 171–179.
367 Y. Jiang, C. Wu, L. Li, K. Wang, Z. Tao, F. Gao, W. Cheng, J. Cheng, X.-Y. Zhao and S. Priya, *Nano energy*, 2018, **53**, 440–448.
368 C. Wu, K. Wang, Y. Jiang, D. Yang, Y. Hou, T. Ye, C. S. Han, B. Chi, L. Zhao, S. Wang, W. Deng and S. Priya, *Advanced Functional Materials*, **n/a**, 2006803.
369 B. Li, F. Dai, Q. Xiao, L. Yang, J. Shen, C. Zhang and M. Cai, *Energy & Environmental Science*, 2016, **9**, 102–106.
370 W. Zhang, H. Lin, Z. Lin, J. Yin, H. Lu, D. Liu and M. Zhao, *ChemSusChem*, 2015, **8**, 2114–2122.
371 L. Chen, Y. Zhang, C. Lin, W. Yang, Y. Meng, Y. Guo, M. Li and D. Xiao, *Journal of Materials Chemistry A*, 2014, **2**, 9684–9690.
372 S. S. Mali, H. Kim, J. V. Patil and C. K. Hong, *ACS Appl. Mater. Interfaces*, 2018, **10**, 31280–31290.
373 L. Gao, Y. Zhou, F. Meng, Y. Li, A. Liu, Y. Li, C. Zhang, M. Fan, G. Wei and T. Ma, *Carbon*, 2020, **162**, 267–272.
374 C. Zhang, D. A. Mcadams and J. C. Grunlan, *Advanced Materials*, 2016, **28**, 6292–6321.
375 U. G. Wegst, H. Bai, E. Saiz, A. P. Tomsia and R. O. Ritchie, *Nature materials*, 2015, **14**, 23–36.
376 J. Vincent, *Living machines: A handbook of research in biomimetics and biohybrid systems*.
377 U. G. K. Wegst and M. F. Ashby, *Philosophical Magazine*, 2004, **84**, 2167–2186.
378 J. Aizenberg and P. Fratzl, *Advanced Materials*, 2009, **21**, 387–388.
379 J. W. Dunlop and P. Fratzl, *Annual Review of Materials Research*, 2010, **40**, 1–24.
380 L. Li and C. Ortiz, *Nature materials*, 2014, **13**, 501–507.
381 F. Song, A. K. Soh and Y. L. Bai, *Biomaterials*, 2003, **24**, 3623–3631.
382 M. A. Meyers, P.-Y. Chen, A. Y.-M. Lin and Y. Seki, *Progress in Materials Science*, 2008, **53**, 1–206.
383 A. G. Evans, Z. Suo, R. Z. Wang, I. A. Aksay, M. Y. He and J. W. Hutchinson, *Journal of Materials Research*, 2001, **16**, 2475–2484.
384 R. Z. Wang, Z. Suo, A. G. Evans, N. Yao and I. A. Aksay, *Journal of Materials Research*, 2001, **16**, 2485–2493.
385 X. Li, Z.-H. Xu and R. Wang, *Nano letters*, 2006, **6**, 2301–2304.
386 B. L. Watson, N. Rolston, A. D. Printz and R. H. Dauskardt, *Energy & Environmental Science*, 2017, **10**, 2500–2508.
387 F. Di Giacomo, A. Fakharuddin, R. Jose and T. M. Brown, *Energy & Environmental Science*, 2016, **9**, 3007–3035.
388 T. Ma, H.-L. Gao, H.-P. Cong, H.-B. Yao, L. Wu, Z.-Y. Yu, S.-M. Chen and S.-H. Yu, *Advanced materials*, 2018, **30**, 1706435.
389 Y. Wu, Q. Liu, J. Fu, Q. Li and D. Hui, *Composites Part B: Engineering*, 2017, **121**, 122–133.
390 J. Yang, D. Gu, K. Lin, Y. Yang and C. Ma, *Journal of the Mechanical Behavior of Biomedical Materials*, 2019, **91**, 59–67.
391 X. Yang, J. Ma, Y. Shi, Y. Sun and J. Yang, *Materials & Design*, 2017, **135**, 275–290.
392 S. A. Sabah, A. B. H. Kueh and M. Y. Al-Fasih, *Composites Science and Technology*, 2017, **149**, 64–74.
393 S. A. Sabah, A. B. H. Kueh and M. Y. Al-Fasih, *Construction and Building Materials*, 2018, **169**, 193–204.
394 N. San Ha, G. Lu and X. Xiang, *Journal of materials science*, 2019, **54**, 6286–6300.
395 S. Haldar and H. A. Bruck, *Composites science and technology*, 2014, **95**, 67–74.
396 S. Shi, Z. Sun, X. Hu and H. Chen, *Thin-Walled Structures*, 2014, **84**, 416–422.
397 Z. Sun, S. Shi, X. Guo, X. Hu and H. Chen, *Composites Part B: Engineering*, 2016, **94**, 245–252.
398 L. Cheng, A. Thomas, J. L. Glancey and A. M. Karlsson, *Composites Part A: Applied Science and Manufacturing*, 2011, **42**, 211–220.
399 S. C. Cao, J. Liu, L. Zhu, L. Li, M. Dao, J. Lu and R. O. Ritchie, *Sci Rep*, 2018, **8**, 5088.
400 J. P. Bilezikian, L. G. Raisz and T. J. Martin, *Principles of bone biology*, Academic press, 2008.
401 V. Zorba, E. Stratakis, M. Barberoglou, E. Spanakis, P. Tzanetakis, S. H. Anastasiadis and C. Fotakis, *Advanced materials*, 2008, **20**, 4049–4054.
402 Q. Xu, W. Zhang, C. Dong, T. S. Sreeprasad and Z. Xia, *Journal of the Royal Society Interface*, 2016, **13**, 20160300.
403 S. M. Kang, N. Ahn, J.-W. Lee, M. Choi and N.-G. Park, *J. Mater. Chem. A*, 2014, **2**, 20017–20021.
404 J. Jeevahan, M. Chandrasekaran, G. Britto Joseph, R. B. Durairaj and G. Mageshwaran, *J Coat Technol Res*, 2018, **15**, 231–250.
405 A. Syafiq, A. K. Pandey, N. N. Adzman and N. Abd Rahim, *Solar Energy*, 2018, **162**, 597–619.
406 mars.nasa.gov, Mars 2020 Perseverance Rover | Missions, https://mars.nasa.gov/mars-exploration/missions/mars2020, (accessed July 17, 2020).
407 B. Dudem, J. H. Heo, J. W. Leem, J. S. Yu and S. H. Im, *Journal of Materials Chemistry A*, 2016, **4**, 7573–7579.
408 J. Woo Leem and J. Su Yu, *RSC Advances*, 2015, **5**, 60804–60813.
409 Definition of HEALING, https://www.merriam-webster.com/dictionary/healing, (accessed July 17, 2020).
410 J. C. Cremaldi and B. Bhushan, *Beilstein Journal of Nanotechnology*, 2018, **9**, 907–935.
411 C. R. Metcalfe, *Econ Bot*, 1967, **21**, 115–127.
412 J. Parkin, *Ann Bot*, 1900, **os-14**, 193–214.
413 G. Bauer, A. Nellesen and T. Speck, *WIT Trans. Ecol. Environ*, 2010, **138**, 453–459.
414 G. Bauer, S. N. Gorb, M.-C. Klein, A. Nellesen, M. von Tapavicza and T. Speck, *PLoS One*, 2014, **9**, e113336.
415 G. Bauer and T. Speck, *Annals of botany*, 2012, **109**, 807–811.
416 A. Nellesen, M. Von Tapavicza, J. Bertling, A. M. Schmidt, G. Bauer and T. Speck, *Polymers from Renewable Resources*, 2011, **2**, 149–156.
417 A. C. Schüssele, F. Nübling, Y. Thomann, O. Carstensen, G. Bauer, T. Speck and R. Mülhaupt, *Macromolecular Materials and Engineering*, 2012, **297**, 411–419.
418 Bone remodelling at a glance | Journal of Cell Science, https://jcs.biologists.org/content/124/7/991.short, (accessed August 31, 2020).
419 T.-S. Wong, S. H. Kang, S. K. Tang, E. J. Smythe, B. D. Hatton, A. Grinthal and J. Aizenberg, *Nature*, 2011, **477**, 443–447.
420 K. Wang, D. Yang, C. Wu, J. Shapter and S. Priya, *Joule*, 2019, **3**, 311–316.
421 K. Wang, D. Yang, C. Wu, M. Sanghadasa and S. Priya, *Progress in Materials Science*, 2019, 100580.
422 K. Wang, C. Wu, Y. Hou, D. Yang and S. Priya, *J. Mater. Chem. A*, 2019, **7**, 24661–24690.
423 H. Li, J. Wu, Z. Yin and H. Zhang, *Accounts of chemical research*, 2014, **47**, 1067–1075.

424 K. Wang, C. Wu, Y. Jiang, D. Yang, K. Wang and S. Priya, *Science advances*, 2019, **5**, eaau3241.
425 Y. Hou, C. Wu, D. Yang, K. Wang, T. Ye, L. Brownlie, K. Wang and S. Priya, *Nano Energy*, 2020, 105133.
426 F. Gao, Y. Zhao, X. Zhang and J. You, *Advanced Energy Materials*, 2020, **10**, 1902650.
427 B. C. Tee, C. Wang, R. Allen and Z. Bao, *Nature nanotechnology*, 2012, **7**, 825–832.
428 K. A. Williams, A. J. Boydston and C. W. Bielawski, *Journal of the royal society interface*, 2007, **4**, 359–362.
429 S. Zhang and F. Cicoira, *Advanced Materials*, 2017, **29**, 1703098.
430 J. Y. Oh, S. Rondeau-Gagné, Y.-C. Chiu, A. Chortos, F. Lissel, G.-J. N. Wang, B. C. Schroeder, T. Kurosawa, J. Lopez and T. Katsumata, *Nature*, 2016, **539**, 411–415.
431 Y. Cao, T. G. Morrissey, E. Acome, S. I. Allec, B. M. Wong, C. Keplinger and C. Wang, *Advanced Materials*, 2017, **29**, 1605099.
432 E. Palleau, S. Reece, S. C. Desai, M. E. Smith and M. D. Dickey, *Advanced Materials*, 2013, **25**, 1589–1592.
433 G. Li, X. Wu and D.-W. Lee, *Lab on a Chip*, 2016, **16**, 1366–1373.
434 B. J. Blaiszik, S. L. Kramer, M. E. Grady, D. A. McIlroy, J. S. Moore, N. R. Sottos and S. R. White, *Advanced Materials*, 2012, **24**, 398–401.
435 A. Babayigit, A. Ethirajan, M. Muller and B. Conings, *Nature materials*, 2016, **15**, 247.
436 D. Fabini, *Quantifying the potential for lead pollution from halide perovskite photovoltaics*, ACS Publications, 2015.
437 A. Babayigit, D. D. Thanh, A. Ethirajan, J. Manca, M. Muller, H.-G. Boyen and B. Conings, *Scientific reports*, 2016, **6**, 1–11.
438 G. Abdelmageed, L. Jewell, K. Hellier, L. Seymour, B. Luo, F. Bridges, J. Z. Zhang and S. Carter, *Applied Physics Letters*, 2016, **109**, 233905.
439 G. Niu, X. Guo and L. Wang, *Journal of Materials Chemistry A*, 2015, **3**, 8970–8980.
440 A. H. Slavney, R. W. Smaha, I. C. Smith, A. Jaffe, D. Umeyama and H. I. Karunadasa, *Inorganic chemistry*, 2017, **56**, 46–55.
441 A. Poglitsch and D. Weber, *The Journal of chemical physics*, 1987, **87**, 6373–6378.
442 D. Cahen and I. Lubomirsky, *Accounts of Chemical Research*, 2017, **50**, 573–576.
443 D. R. Ceratti, Y. Rakita, L. Cremonesi, R. Tenne, V. Kalchenko, M. Elbaum, D. Oron, M. A. C. Potenza, G. Hodes and D. Cahen, *Advanced Materials*, 2018, **30**, 1706273.
444 Y. Zhao, J. Wei, H. Li, Y. Yan, W. Zhou, D. Yu and Q. Zhao, *Nature communications*, 2016, **7**, 1–9.
445 C. Ran, W. Gao, J. Li, J. Xi, L. Li, J. Dai, Y. Yang, X. Gao, H. Dong and B. Jiao, *Joule*, 2019, **3**, 3072–3087.
446 F. Lang, N. H. Nickel, J. Bundesmann, S. Seidel, A. Denker, S. Albrecht, V. V. Brus, J. Rappich, B. Rech and G. Landi, *Advanced Materials*, 2016, **28**, 8726–8731.
447 T. Markvart, *Journal of Materials Science: Materials in Electronics*, 1990, **1**, 1–12.
448 D. Mottl and R. Nymmik, *Advances in Space Research*, 2003, **32**, 2349–2353.
449 R. Schwenn, *Encyclopedia of Astronomy and Astrophysics*, 2001, **785998**, 1–9.
450 H.-C. Neitzert, P. Spinillo, S. Bellone, G.-D. Licciardi, M. Tucci, F. Roca, L. Gialanella and M. Romano, *Solar energy materials and solar cells*, 2004, **83**, 435–446.
451 W. Nie, J.-C. Blancon, A. J. Neukirch, K. Appavoo, H. Tsai, M. Chhowalla, M. A. Alam, M. Y. Sfeir, C. Katan and J. Even, *Nature communications*, 2016, **7**, 1–9.
452 M. Bag, L. A. Renna, R. Y. Adhikari, S. Karak, F. Liu, P. M. Lahti, T. P. Russell, M. T. Tuominen and D. Venkataraman, *Journal of the American Chemical Society*, 2015, **137**, 13130–13137.
453 P. Yadav, D. Prochowicz, E. A. Alharbi, S. M. Zakeeruddin and M. Grätzel, *Journal of Materials Chemistry C*, 2017, **5**, 7799–7805.
454 K. Domanski, B. Roose, T. Matsui, M. Saliba, S.-H. Turren-Cruz, J.-P. Correa-Baena, C. R. Carmona, G. Richardson, J. M. Foster and F. De Angelis, *Energy & Environmental Science*, 2017, **10**, 604–613.
455 S.-W. Lee, S. Kim, S. Bae, K. Cho, T. Chung, L. E. Mundt, S. Lee, S. Park, H. Park and M. C. Schubert, *Scientific reports*, 2016, **6**, 1–10.
456 R. Gottesman, L. Gouda, B. S. Kalanoor, E. Haltzi, S. Tirosh, E. Rosh-Hodesh, Y. Tischler, A. Zaban, C. Quarti and E. Mosconi, *The journal of physical chemistry letters*, 2015, **6**, 2332–2338.
457 G. Nan, X. Zhang and G. Lu, *The Journal of Physical Chemistry Letters*, 2019, **10**, 7774–7780.
458 A. Miyata, A. Mitioglu, P. Plochocka, O. Portugall, J. T.-W. Wang, S. D. Stranks, H. J. Snaith and R. J. Nicholas, *Nature Physics*, 2015, **11**, 582–587.
459 A. Jha, H.-G. Duan, V. Tiwari, P. K. Nayak, H. J. Snaith, M. Thorwart and R. D. Miller, *Acs Photonics*, 2017, **5**, 852–860.
460 Y. Tian, M. Peter, E. Unger, M. Abdellah, K. Zheng, T. Pullerits, A. Yartsev, V. Sundström and I. G. Scheblykin, *Physical Chemistry Chemical Physics*, 2015, **17**, 24978–24987.
461 Y. Jiang, L. Qiu, E. J. Juarez-Perez, L. K. Ono, Z. Hu, Z. Liu, Z. Wu, L. Meng, Q. Wang and Y. Qi, *Nature Energy*, 2019, **4**, 585–593.
462 Y. Yang and M. W. Urban, *Angewandte Chemie*, 2014, **126**, 12338–12343.
463 H. Ying, Y. Zhang and J. Cheng, *Nature communications*, 2014, **5**, 1–9.
464 X. Chen, M. A. Dam, K. Ono, A. Mal, H. Shen, S. R. Nutt, K. Sheran and F. Wudl, *Science*, 2002, **295**, 1698–1702.
465 B. Ghosh and M. W. Urban, *Science*, 2009, **323**, 1458–1460.
466 K. Imato, M. Nishihara, T. Kanehara, Y. Amamoto, A. Takahara and H. Otsuka, *Angewandte Chemie*, 2012, **124**, 1164–1168.
467 P. Cordier, F. Tournilhac, C. Soulié-Ziakovic and L. Leibler, *Nature*, 2008, **451**, 977–980.
468 M. Burnworth, L. Tang, J. R. Kumpfer, A. J. Duncan, F. L. Beyer, G. L. Fiore, S. J. Rowan and C. Weder, *Nature*, 2011, **472**, 334–337.
469 M. Nakahata, Y. Takashima, H. Yamaguchi and A. Harada, *Nature communications*, 2011, **2**, 1–6.
470 M. W. Urban, D. Davydovich, Y. Yang, T. Demir, Y. Zhang and L. Casabianca, *Science*, 2018, **362**, 220–225.
471 S. R. White, N. R. Sottos, P. H. Geubelle, J. S. Moore, M. R. Kessler, S. R. Sriram, E. N. Brown and S. Viswanathan, *Nature*, 2001, **409**, 794–797.
472 M. R. Kessler, N. R. Sottos and S. R. White, *Composites Part A: applied science and manufacturing*, 2003, **34**, 743–753.
473 N. K. Noel, A. Abate, S. D. Stranks, E. S. Parrott, V. M. Burlakov, A. Goriely and H. J. Snaith, *ACS nano*, 2014, **8**, 9815–9821.
474 D. Bi, C. Yi, J. Luo, J.-D. Décoppet, F. Zhang, S. M. Zakeeruddin, X. Li, A. Hagfeldt and M. Grätzel, *Nature Energy*, 2016, **1**, 1–5.
475 J. Han, S. Luo, X. Yin, Y. Zhou, H. Nan, J. Li, X. Li, D. Oron, H. Shen and H. Lin, *Small*, 2018, **14**, 1801016.
476 S. Liu, Y. Guan, Y. Sheng, Y. Hu, Y. Rong, A. Mei and H. Han, *Advanced Energy Materials*, 2020, **10**, 1902492.

477 A. Mahapatra, D. Prochowicz, M. M. Tavakoli, S. Trivedi, P. Kumar and P. Yadav, *Journal of Materials Chemistry A*, 2020, **8**, 27–54.
478 R. Wang, J. Xue, L. Meng, J.-W. Lee, Z. Zhao, P. Sun, L. Cai, T. Huang, Z. Wang, Z.-K. Wang, Y. Duan, J. L. Yang, S. Tan, Y. Yuan, Y. Huang and Y. Yang, *Joule*, 2019, **3**, 1464–1477.
479 M. Zhang, M. Tai, X. Li, X. Zhao, H. Chen, X. Yin, Y. Zhou, Q. Zhang, J. Han and N. Wang, *Solar RRL*, 2019, **3**, 1900345.
480 Z. Guo, *Acta Pharmaceutica Sinica B*, 2016, **6**, 115–124.
481 P. Cravo, H. Napolitano and R. Culleton, *Acta Tropica*, 2015, **148**, 1–7.
482 E. A. Winzeler and M. J. Manary, *Genome Biology*, 2014, **15**, 544.
483 A. Antonacci and V. Scognamiglio, *TrAC Trends in Analytical Chemistry*, 2019, **115**, 100–109.
484 F. Wang, X. Liu and I. Willner, *Advanced Materials*, 2013, **25**, 349–377.
485 S. Kishore Ravi, N. Paul, L. Suresh, A. Tjitra Salim, T. Wu, Z. Wu, M. R. Jones and S. Ching Tan, *Materials Horizons*, 2020, **7**, 866–876.
486 S. K. Ravi, P. Rawding, A. M. Elshahawy, K. Huang, W. Sun, F. Zhao, J. Wang, M. R. Jones and S. C. Tan, *Nat Commun*, 2019, **10**, 902.
487 N. Paul, L. Suresh, J. V. Vaghasiya, L. Yang, Y. Zhang, D. K. Nandakumar, M. R. Jones and S. C. Tan, *Biosensors and Bioelectronics*, 2020, **165**, 112423.
488 H. Wang, S. Lin, E. Katilius, C. Laser, J. P. Allen, J. C. Williams and N. W. Woodbury, *J. Phys. Chem. B*, 2009, **113**, 818–824.
489 P. Singh, S. Singh, N. Jaggi, K.-H. Kim and P. Devi, *Nano Energy*, 2021, **79**, 105482.
490 X. He, M. Aizenberg, O. Kuksenok, L. D. Zarzar, A. Shastri, A. C. Balazs and J. Aizenberg, *Nature*, 2012, **487**, 214–218.
491 E. Wang, M. S. Desai and S.-W. Lee, *Nano Lett.*, 2013, **13**, 2826–2830.
492 A. Shastri, L. M. McGregor, Y. Liu, V. Harris, H. Nan, M. Mujica, Y. Vasquez, A. Bhattacharya, Y. Ma, M. Aizenberg, O. Kuksenok, A. C. Balazs, J. Aizenberg and X. He, *Nature Chemistry*, 2015, **7**, 447–454.
493 M. Qin, M. Sun, M. Hua and X. He, *Current Opinion in Solid State and Materials Science*, 2019, **23**, 13–27.
494 M. Qin, M. Sun, R. Bai, Y. Mao, X. Qian, D. Sikka, Y. Zhao, H. J. Qi, Z. Suo and X. He, *Advanced Materials*, 2018, **30**, 1800468.
495 M. Sun, R. Bai, X. Yang, J. Song, M. Qin, Z. Suo and X. He, *Advanced Materials*, 2018, **30**, 1804916.
496 T. J. White and D. J. Broer, *Nature Materials*, 2015, **14**, 1087–1098.
497 A. H. Gelebart, D. Jan Mulder, M. Varga, A. Konya, G. Vantomme, E. W. Meijer, R. L. B. Selinger and D. J. Broer, *Nature*, 2017, **546**, 632–636.
498 O. M. Wani, H. Zeng and A. Priimagi, *Nature Communications*, 2017, **8**, 15546.
499 Y.-L. Zhao and J. F. Stoddart, *Langmuir*, 2009, **25**, 8442–8446.
500 R. Klajn, *Chemical Society Reviews*, 2014, **43**, 148–184.
501 X. Qian, Y. Zhao, Y. Alsaid, X. Wang, M. Hua, T. Galy, H. Gopalakrishna, Y. Yang, J. Cui, N. Liu, M. Marszewski, L. Pilon, H. Jiang and X. He, *Nature Nanotechnology*, 2019, **14**, 1048–1055.
502 G. Prinsloo and R. Dobson, *Sun Tracker, Automatic Solar-Tracking, Sun-Tracking Systems, Solar Trackers and Automatic Sun Tracker Systems 太陽能跟踪 Солнечная слежения: High precision solar position algorithms, programs, software and source-code for computing the solar vector, solar coordinates & sun angles in Microprocessor, PLC, Arduino, PIC and PC-based sun tracking devices or dynamic sun following hardware*, Gerro Prinsloo, 2014.
503 S. Seme, G. Štumberger and J. Voršič, *IEEE Transactions on Power Electronics*, 2011, **26**, 1280–1290.
504 Track Racks – Solar Trackers – Photovoltaic Racks | Zomeworks Corporation, http://www.zomeworks.com/photovoltaic-tracking-racks/, (accessed July 17, 2020).
505 M. J. Clifford and D. Eastwood, *Solar Energy*, 2004, **77**, 269–280.
506 C. E. F. Castañeda, *Prodetec-Programa de Pós-Graduação de Desenvolvimento Tecnologico*.
507 R. H. McFee, *Appl. Opt., AO*, 1975, **14**, 1493–1502.
508 F. R. Rubio, M. G. Ortega, F. Gordillo and M. López-Martínez, *Energy Conversion and Management*, 2007, **48**, 2174–2184.
509 C.-Y. J. Lee, P.-C. Chou, Y.-C. Chen, C.-M. Chiang and C.-F. Lin, *The Open Construction and Building Technology Journal*.
510 B. J. Huang, W. L. Ding and Y. C. Huang, *Solar Energy*, 2011, **85**, 1935–1944.
511 Byeong-Ho Jeong, Ju-Hoon Park, Seung-Dai Kim and Jong-Ho Kang, in *2013 International Conference on Electrical Machines and Systems (ICEMS)*, 2013, pp. 414–417.
512 V. P. More and V. K. Kulkarni, *International Journal of Current Engineering and Technology*, 2014, **2**, 230–234.
513 S. M. Çinar, F. O. Hocaoğlu and M. Orhun, *Journal of Renewable and Sustainable Energy*, 2014, **6**, 033143.
514 F. J. Dyson, *Science*, 1960, **131**, 1667–1668.
515 G. J. Lee, C. Choi, D.-H. Kim and Y. M. Song, *Advanced Functional Materials*, 2018, **28**, 1705202.
516 L. Gu, S. Poddar, Y. Lin, Z. Long, D. Zhang, Q. Zhang, L. Shu, X. Qiu, M. Kam, A. Javey and Z. Fan, *Nature*, 2020, **581**, 278–282.
517 F. Xia and L. Jiang, *Advanced Materials*, 2008, **20**, 2842–2858.
518 L. Ge, S. Sethi, L. Ci, P. M. Ajayan and A. Dhinojwala, *Proceedings of the National Academy of Sciences*, 2007, **104**, 10792–10795.
519 K. Liu, Y. Tian and L. Jiang, *Progress in Materials Science*, 2013, **58**, 503–564.
520 M. Nicolas, F. Guittard and S. Géribaldi, *Angewandte Chemie*, 2006, **118**, 2309–2312.
521 X. Yao, Y. Song and L. Jiang, *Advanced Materials*, 2011, **23**, 719–734.
522 S. Yin, X. Men, H. Sun, P. She, W. Zhang, C. Wu, W. Qin and X. Chen, *Journal of Materials Chemistry A*, 2015, **3**, 12016–12022.
523 J. Wang, J. Qiao, J. Wang, Y. Zhu and L. Jiang, *ACS applied materials & interfaces*, 2015, **7**, 9281–9286.
524 J. M. Galloway, J. P. Bramble and S. S. Staniland, *Chemistry–A European Journal*, 2013, **19**, 8710–8725.
525 H.-B. Yao, H.-Y. Fang, Z.-H. Tan, L.-H. Wu and S.-H. Yu, *Angewandte Chemie*, 2010, **122**, 2186–2191.
526 A. Walther, I. Bjurhager, J.-M. Malho, J. Pere, J. Ruokolainen, L. A. Berglund and O. Ikkala, *Nano letters*, 2010, **10**, 2742–2748.
527 Y.-Q. Li, T. Yu, T.-Y. Yang, L.-X. Zheng and K. Liao, *Advanced Materials*, 2012, **24**, 3426–3431.
528 I. B. Burgess, J. Aizenberg and M. Lončar, *Bioinspir. Biomim.*, 2013, **8**, 045004.
529 S. Yang, J. Ford, C. Ruengruglikit, Q. Huang and J. Aizenberg, *Journal of Materials Chemistry*, 2005, **15**, 4200–4202.
530 B. Pokroy, A. K. Epstein, M. C. Persson-Gulda and J. Aizenberg, *Advanced Materials*, 2009, **21**, 463–469.
531 Y. Li, J. Zhang, S. Zhu, H. Dong, F. Jia, Z. Wang, Y. Tang, L. Zhang, S. Zhang and B. Yang, *Langmuir*, 2010, **26**, 9842–9847.

532 C. Y. Tay, Y.-L. Wu, P. Cai, N. S. Tan, S. S. Venkatraman, X. Chen and L. P. Tan, *NPG Asia Materials*, 2015, **7**, e199–e199.
533 Y. Zhao, Z. Xie, H. Gu, C. Zhu and Z. Gu, *Chemical Society Reviews*, 2012, **41**, 3297–3317.
534 A. del Campo and E. Arzt, *Macromolecular Bioscience*, 2007, **7**, 118–127.
535 G. Villar, A. D. Graham and H. Bayley, *Science*, 2013, **340**, 48–52.
536 Y. Yang, X. Song, X. Li, Z. Chen, C. Zhou, Q. Zhou and Y. Chen, *Advanced Materials*, 2018, **30**, 1706539.
537 S. Mann, *Biomineralization: principles and concepts in bioinorganic materials chemistry*, Oxford University Press on Demand, 2001, vol. 5.
538 X. Zhang, Z. Zhang, Y. Zhang, D. Wei and Y. Deng, *Safety Science*, 2013, **54**, 87–91.
539 J. A. Jiménez-Avalos, G. Arrevillaga-Boni, L. González-López, Z. Y. García-Carvajal and M. González-Avila, *Critical Reviews in Food Science and Nutrition*, 2021, **61**, 234–258.
540 G. Flora, D. Gupta and A. Tiwari, *Interdisciplinary Toxicology*, 2012, **5**, 47–58.
541 N. C. for E. Health, CDC - Lead - CDC's Childhood Lead Poisoning Prevention Program, https://www.cdc.gov/nceh/lead/about/program.htm, (accessed July 17, 2020).
542 *The Code of Federal Regulations of the United States of America*, U.S. Government Printing Office, 2005.
543 R. F. Service, *Science*, 2016, **354**, 1214–1215.
544 N. Flomenbaum, L. Goldfrank, R. Hoffman, M. A. Howland, N. Lewin and L. Nelson, .
545 V. Cangelosi, L. Ruckthong and V. L. Pecoraro, *Metal ions in life sciences*.
546 End-of-life management, /publications/2016/Jun/End-of-life-management-Solar-Photovoltaic-Panels, (accessed March 19, 2021).
547 L. A. Estroff, *Chem. Rev.*, 2008, **108**, 4329–4331.
548 A. du Plessis, C. Broeckhoven, I. Yadroitsava, I. Yadroitsev, C. H. Hands, R. Kunju and D. Bhate, *Additive Manufacturing*, 2019, **27**, 408–427.
549 D. Bhate, C. A. Penick, L. A. Ferry and C. Lee, *Designs*, 2019, **3**, 19.
550 S. Li, H. Bai, R. F. Shepherd and H. Zhao, *Angewandte Chemie International Edition*, 2019, **58**, 11182–11204.
551 G. D. Scholes, G. R. Fleming, L. X. Chen, A. Aspuru-Guzik, A. Buchleitner, D. F. Coker, G. S. Engel, R. van Grondelle, A. Ishizaki, D. M. Jonas, J. S. Lundeen, J. K. McCusker, S. Mukamel, J. P. Ogilvie, A. Olaya-Castro, M. A. Ratner, F. C. Spano, K. B. Whaley and X. Zhu, *Nature*, 2017, **543**, 647–656.
552 F. Dubin, R. Melet, T. Barisien, R. Grousson, L. Legrand, M. Schott and V. Voliotis, *Nature Physics*, 2006, **2**, 32–35.
553 M. Einzinger, T. Wu, J. F. Kompalla, H. L. Smith, C. F. Perkinson, L. Nienhaus, S. Wieghold, D. N. Congreve, A. Kahn, M. G. Bawendi and M. A. Baldo, *Nature*, 2019, **571**, 90–94.
554 N. J. Thompson, D. N. Congreve, D. Goldberg, V. M. Menon and M. A. Baldo, *Applied Physics Letters*, 2013, **103**, 263302.
555 L. Yang, M. Tabachnyk, S. L. Bayliss, M. L. Böhm, K. Broch, N. C. Greenham, R. H. Friend and B. Ehrler, *Nano Lett.*, 2015, **15**, 354–358.